Appendix 12-5: Environmental and Hydrologic History of Estero Bay: Implications for Watershed Management and Restoration

Michael Savarese[1], Ai Ning Loh[1] and John H. Trefry[2],
November 2004

[1] Florida Gulf Coast University, College of Arts and Sciences
[2] Florida Institute of Technology, Department of Marine and Environmental Systems

Environmental and Hydrologic History of Estero Bay: Implications for Watershed Management and Restoration

Contract #C-15871

Final Report

Drs. Michael Savarese[1], Ai Ning Loh[2], & John H. Trefry[3]

[1,2] Florida Gulf Coast University
College of Arts & Sciences
10501 FGCU Blvd. South
Ft. Myers, Florida 33965-6565
[1](239) 590-7165 msavares@fgcu.edu
[2](239) 590-7261 anloh@fgcu.edu

[3] Florida Institute of Technology
Department of Marine and Environmental Systems
Oceanography Program
150 West University Blvd.
Melbourne, Florida 32901-6975
(321) 674-8096 jtrefry@fit.edu

Submitted to the South Florida Water Management District

November 22, 2004

Executive Summary

Introduction

The purpose of this study was two-fold. First, Estero Bay's watershed management and restoration are being planned without regard to the effects of sea level rise. Sea level rise not only controls the distribution of environments through time, but also the evolution of estuarine geomorphology. Accelerated sea level rise rate, since the beginning of industrialization, may grossly change the estuarine-scape over decadal and centennial time scales. In addition, oyster reef development appears to be integral to estuarine geomorphology. For other regions of the Southwest Florida coast, particularly the Ten Thousand Islands, it has been demonstrated that the coast has prograded seaward despite rising sea level because the rate of reef sedimentation and accretion has exceeded the modest rate of sea level rise. Restoration planning is best conducted with these insights.

Second, development of Estero Bay's watersheds should alter the rate at which bed- and suspended-load sediment is delivered to the bay. This has consequences for bay ecology (i.e., sedimentation can affect light attenuation, primary productivity, and aspects of physical water quality) and for geomorphologic evolution (i.e., the estuarine-scape evolves in response to the net sum of sea level rise rate and the rate of sedimentation).

In order to investigate these two phenomena, a geological investigation of Estero Bay's late Holocene (last 5000 years) history and the recent changes of sedimentation rate was undertaken. Because the Southwest Florida coast has experienced variable sea level rise rates throughout the late Holocene, the ways in which the coast has responded in the past should allow future responses to be predicted.

The study addressed four central questions. They were:

(1) How has the coast and estuarine-scape evolved through the late Holocene as sea level rise rates have varied? (2) What role has reef development played in this evolution? (3) How has fluvial sedimentation and freshwater delivery varied during this time interval? And (4) how have sedimentation rates changed over recent history, since human development?

To address these questions research focused on 3 study regions within Estero Bay, each reflecting one of the major watersheds entering the bay: (1) Hendry and Mullock Creeks, entering the northern region of the bay; (2) Estero River, entering the north-central portion of the bay; and (3) Imperial River, entering in the south.

Five principal objectives were defined:

Determine the paleoenvironmental context of the late Holocene (< 5000 years) strata preserved in the sedimentary cores taken from Estero Bay through sedimentologic and faunal analyses. 2. Refine the paleoenvironmental interpretations through organic geochemical analysis. 3. Establish both a low (< 5000 years) and high (last 200 years) resolution geochronologic framework for environmental history. 4. Interpret the spatial and temporal distribution of environments over the late Holocene through lithocorrelation and chronocorrelation. 5. Determine the rates of deposition and the changes in those rates over recent time scales.

Methods

Core transects were established in each of the 3 watersheds: 1 in Hendry / Mullock Creek, 1 in Estero River, and 2 in the Imperial (1 oriented along the eastern, inshore margin of Estero Bay and the other along the western, offshore margin). Sediment traversing the late Holocene cover down to Pliocene bedrock was cored from numerous locations along each transect. Standard practices of sedimentology, stratigraphy, paleontology, and carbon and nitrogen isotopic geochemistry were undertaken to identify facies, interpret their environmental context, and to correlate common environments across space and time.

Recent geochronologies (past 100 years) were obtained for one sediment core from southern Estero Bay and one from northern Estero Bay. Vertical profiles for excess ^{210}Pb and ^{137}Cs were used to determine sedimentation rates. Concentrations of Al, TOC, and $CaCO_3$ also were determined in selected layers throughout each core.

Most Significant Results & Their Implications

(1) Eleven facies were recognized within the late Holocene strata from all cores. Those facies represent the following suite of depositional paleoenvironments: 1. regolith – weathered bedrock found at the base of many cores; 2. supratidal / subaerial sands – portions of soil profiles probably from upland settings; 3. freshwater peats – organic material deposited in freshwater wetlands; 4. riverine sediments – sands deposited in river-related environments such as channels, point bars, and deltas; 5. intertidal mangrove peats – representing mangrove forests that are tidally inundated during extreme high tides; 6. intertidal sand and mud flats; 7. organic-rich, shell-poor subtidal sands and muds – low brackish water subtidal settings; 8. shell-rich subtidal sands and muds – higher brackish water subtidal settings rich in estuarine mollusks; 9. marine subtidal vermetiform gastropod-dominated reefs – high energy, open coast, near marine reef environments constructed by vermetiform gastropods; 10. high brackish, oyster – vermetiform gastropod reefs – slightly lower salinity and less exposed than the vermetiform-dominated reefs; and 11. brackish intertidal oyster reefs – medial brackish water, well-protected reef environments.

(2) Progradation has generated the estuarine ecology and coastal geomorphology we see today in Estero Bay and elsewhere in Southwest Florida. That progradation has occurred in a mosaic pattern, rather than a linear seaward direction, and despite the modest rate of sea level rise (< 10 cm / 100 yrs) over the last 3000 years. Oyster reef development plays a critical role in the progradation; internal sedimentation on a reef, coupled with oyster accretion, generates rates of upward growth that exceed the modest rate of sea level rise. Reefs grow up into high intertidal heights and then become the substrate for mangrove propagule settlement and eventual mangrove forest proliferation.

(3) Current rates of sea level rise (since the beginning of industrialization) are an order of magnitude higher than they were in the 3000 previous years. Reef sedimentation and accretion cannot keep pace with the accelerated rate of sea level rise (oyster reefs accrete at rates not exceeding 18 cm / 100 years). If the current sea level rise rate persists over decadal and centennial scales, oyster reef development will become less prolific both spatially and temporally and the coastal geomorphology of Southwest Florida, including that seen in Estero Bay, will change considerably. In addition, the oyster-reef-based estuarine ecology will cease to exist. These predictions are supported by the

history that has been interpreted for early in the late Holocene. Between 4500 – 5500 ybp, incipient oyster reef development occurred within proto-Estero Bay (and elsewhere along the Southwest Florida coast), but failed. This failure corresponded in time to an interval of higher sea level rise.

(4) The carbon and nitrogen stable isotopic composition of organic materials deposited within the late Holocene sequences can be very useful in deciphering the vegetative origins of the organic matter. This was particularly helpful in the paleoenvironmental interpretation of facies lacking in shelly faunas. For example, it is often difficult to differentiate a freshwater-influenced environment from a marine or estuarine environment that lacks a shelly fauna. Freshwater and marine environmental end-members have distinct carbon isotopic signatures, and these were used to corroborate the paleoenvironmental interpretations of suspect freshwater facies.

(5) Other geologists have speculated that the shift to a transgressive phase along the southern Florida coast during times of accelerated sea level rise could be triggered abruptly in response to storm events. The hypothesis proposed states that the inner bay margins are currently in a metastable state, and they are likely to transgress after storm-induced erosion of the mangrove forest fringe. Our results support this hypothesis. The inner bay margin has remained relatively stable for the last 2500 years; there is no evidence to suggest that estuarine subtidal environments existed landward of the current mangrove fringe. Cores taken just a few meters seaward of the inner bay margin exhibit abrupt truncations, due to erosion, of mangrove peat down a distance between a few centimeters and decimeters of the current sediment-water interface. These cores represent recent step-backs of the inner bay margin after the passage of tropical storms.

(6) There is some evidence supporting the interpretation of the proto-Estero estuary as having a more open, unprotected western margin as recently as 2300 ybp. Cores taken from modern oyster reefs in north-central Estero Bay show reef autogenic successional histories whereby very high energy, marine water reefs constructed by vermetiform gastropods (belonging the families Turritellidae and Vermetidae) gradually alter to low energy, brackish water reefs constructed by the American oyster. Marine, high-energy reefs initiated between 2300 – 2700 ybp; the transition to oyster-only reef development occurred at 470 ybp. We further speculate that the vermetiform gastropod reefs served as the first barriers to freshwater retention, thereby predisposing Estero Bay to an estuarine existence.

(7) The core taken from the back-barrier setting behind Ft. Myers Beach supports this interpretation. The core shows a stratigraphic sequence of a high-energy inner shelf (believed to be time equivalent to the vermetiform reefs), overlain by a supratidal facies believed to be the barrier island, and finally capped by a mangrove peat formed in a back-barrier mangrove forest. No dates from this core are currently available.

(8) Our work also indicates that the Imperial River has been a formidable supplier of detrital sediment to southern Estero Bay for at least the last 460 years, the date of oldest riverine sediment found in the two Imperial core transects. The southern end of the bay has a somewhat unique geomorphology and is composed of an aggraded infilling of the back-barrier environment. Coring results suggest that this system experienced a more linear, rather than mosaic, progradation from south to north. One core taken from the southern edge of Big Hickory Bay, however, demonstrates that progradation through the development of oyster reefs to mangrove forests has also occurred in the southern

portion of Estero. We conclude that progradation has been caused by two phenomena in this region of the bay: 1) a linear progradation caused by fluvial sedimentation associated with the Imperial River mouth; and 2) a mosaic progradation caused by oyster reef sedimentation and accretion. The former is unique for Estero; the latter is found through the 3 watersheds.

(9) The measurement of recent rates of sedimentation (< 100 years) conducted using radiogenic isotopes and concentrations of aluminum, TOC, and $CaCO_3$ (at two locations, one in northern and one in southern Estero Bay) demonstrates that sedimentation rates have been high since 1950 and have accelerated over the last 50 years. The rate increase is particularly high for the southern Estero Bay site in the Imperial River watershed. Interestingly, the site chosen in the south was located in Fishtrap Bay, presently within the current river's flow path (the Imperial River's mouth was shifted from a more easterly to westerly position since development began in the Bonita area). The increase in sedimentation may reflect this engineered shift in the Imperial River's navigable channel. Regardless, the results from the high-resolution sedimentation rate aspect of the study indicate that the timing of watershed development has coincided with the time of accelerated sedimentation. This implies that river-based sediment could be treated as estuarine pollutants subjected to TMDL controls.

Acknowledgments

This research project was made possible through funding provided by the South Florida Water Management District (contract #C-15871). An internal grant was also provided by Florida Gulf Coast University (FGCU). Special thanks go to Peter Doering, Melody Hunt, Bob Chamberlain, and Tomma Barnes, all from the South Florida Water Management District, for their support and encouragement. The science benefited greatly from contributions from the following professionals: Rick Oches (University of South Florida, Tampa), Lenore Tedesco and Kathy Licht (Indiana University – Purdue University at Indianapolis), Hal Wanless (University of Miami), Richard Davis (University of South Florida, Tampa), Lynn Wingard (U.S. Geological Survey), and Jose Leal (Bailey-Matthews Shell Museum). Robert D. Rember, Robert P. Trocine, and Debra W. Woodall (from Florida Institute of Technology) assisted John Trefry in the high resolution geochronologic work. The FGCU Coastal Watershed Institute's lab managerial staff, Erin Rasnake, Leslie Haynes, and Sharon Thurston, helped facilitate the field work. Two student theses made contributions to the project: a masters thesis by Heather Rein and a senior thesis by Stephanie Obley. A second masters thesis, by Jorge Agobian, was inspired by the research and is currently underway. In addition, two senior theses, by Kamila Diddle and Jerry Berry, were initiated by this work and completed last spring. Finally, numerous students and interns helped with various aspects of the project, the most notable being Kamila Diddle, Brian Marlowe, Susan Cone, Amanda Bridges, Jorge Agobian, Todd Bost, Amanda Woodruff, Laura Markley, and Jerry Berry.

Table of Contents

List of Tables

List of Figures

List of Appendices

A. Stratigraphic columns for all cores taken for late Holocene history.
B. Sediment grain size histograms and cumulative weight percent graphs for all sediment samples taken from late Holocene cores.
C. Results from faunal analysis counts.
D. Digital images of cores (attached as a CD).
E. Report written by J.H. Trefry, R.D. Rember, R.P. Trocine, and D.W. Woodall entitled "Sedimentation Rates and Sediment Composition in Estero Bay, Florida" (attached as separate pdf).

Introduction

Southwest Florida's rapid population growth and development has generated a number of hydrologic and water quality problems for our coastal ecosystems. Typically development grossly changes the volume of freshwater runoff and the sediment load carried into our coastal waterways and estuaries. As natural habitat becomes impervious to water because of housing and roadway construction, freshwater runoff tends to increase, often leading to higher sedimentation rates in coastal bays. Sedimentation in turn affects the estuarine biota by increasing turbidity and decreasing light penetration of the water column and by the fouling of benthic organisms. Consequently, the effects of managed river flow on sedimentation must be considered when establishing minimum flows and levels.

Commensurate with the anthropogenic effects on hydrology and sedimentation is the natural shift in the position of sea level through time. Sea level rise exacerbates problems of water quality and hydrology. Although sea level has been progressively rising over the last 18,000 years, since the end of the last glaciation, the rate of rise has fluctuated considerably (Figures 1 & 2). Sea level is arguably uncontrollable through standard practices of environmental management, though it is undoubtedly driven ultimately by human-forced climatic change (IPCC, 1996). However, it is of vital concern to regional planning. First, Southwest Florida must anticipate the longer-term environmental effects of sea level rise. It would be futile to develop management strategies or restoration plans that were discordant with these effects. Second, many of our region's planning and management practices are inconsistent with the anticipated environmental effects of sea level rise.

Additionally, the rate of sea level rise controls the morphology of southern Florida's coast (Wanless & Parkinson, 1989; Wanless et al., 1994). This physiography, often referred to by geologists as the "Ten Thousand Islands geomorphology" (Figure 3), is typified by protected inner bays and numerous, intervening mangrove-forested islands, and is a consequence of 3200 years of a slow sea level rise (< 6 cm / 100 years; Parkinson, 1989). Under this regime, the rate of sedimentation has actually exceeded the rate of sea level rise, and this has permitted the building seaward of the Ten Thousand Islands morphology (Parkinson, 1989; Figures 4 & 5). Our coasts have prograded

seaward despite rising sea level. A sea level rise rate that grossly exceeds rate of sedimentation should destabilize this morphology. Recent measurements of sea level rise rates, by recording tide heights over time (Maul & Martin, 1993), suggest that this critical threshold has been exceeded since the beginning of industrialization in the late 19th Century. Rates from Key West since the early part of the 20th Century have approximated 30 cm / 100 years (Figure 6, taken from Maul & Martin, 1993). Tide gauge data from a station in Fort Myers since deployment in 1966 show a similarly high rate of approximately 12 cm / 100 years (Figure 7). When compiled for sites throughout Florida, rates over the last century have been measured between 20-40 cm / 100 years, an order of magnitude higher than the rate that has persisted for the previous 3000 years (Wanless et al., 1994). Admittedly, 100 years of observation are not sufficient to distinguish a natural anomaly from a radical change. If the latter is true, however, the geomorphology that has dominated for the last 3000 years may quickly degrade and leave a more linear and less environmentally diverse coastline in its place. Finally, the change in the rate of sedimentation through the history of development in Southwest Florida relative to the change in sea level rise rate must also be considered (see, for example, Cahoon & Lynch, 1997). Intuition suggests that any sedimentation rate increase due to watershed management probably will not accommodate the increase in the rate of sea level rise.

The coastal progradation the Southwest Florida coast has experienced over the last 3000 years is principally caused by the high rates of sedimentation and accretion of oysters and the reefs they form. Oysters are most productive under polyhaline conditions (18-30 ppt). These salinities have been traditionally located along the inner to middle reaches of the inner bays, just seaward of the river mouths. Oyster suspension feeding leads to the production of fecal and pseudofecal pelloids which effectively increase the sedimentation rate of mud-sized particles on a reef. In addition, high productivity causes increased rates of shell biomineralization and larval recruitment. This increases the rate of clump formation and shell accretion on a reef. The two phenomena work in concert to move an oyster reef quickly into the high intertidal. This, in turn, promotes the settlement of mangrove propagules (Figure 8). Once mangrove trees take root, the high productivity associated with root formation (i.e., peat generation) effectively increases

sedimentation rate further. Under modest rates of sea level rise, reef and mangrove sedimentation and accretion easily overtake sea level rise, and the coast exhibits a mosaic progradation where an ecological succession of oyster reef to mangrove forest occurs (Figure 4). Consequently, not only is Southwest Florida's estuarine ecology dependent upon oyster reef formation (Savarese et al., 2003; Tolley et al., 2003), so is our coastal geomorphology. Commensurate with the study of late Holocene history must be an investigation of the history of reef formation.

The implications of such changes in sea level rise and sedimentation are great. Much of southern Florida's biodiversity, many of its endangered species, and much of our estuarine productivity depend upon subtidal and intertidal communities and mangrove-forest coastal wetlands. It will be these habitats that will most drastically change in geographic position and aerial extent due to sea level rise and have their ecology most seriously compromised by higher rates of sedimentation (e.g., Ellison & Stoddart, 1991; Snedaker, 1993; SFWMD, 2001 [historic and recent vegetative habitat maps show spatial change of mangrove and salt marsh]). Although every estuarine system in Southwest Florida must contend with these issues, Estero Bay and its freshwater watersheds are particularly at risk (Figure 9). Estero Bay's watersheds are still relatively undisturbed, though the potential for extensive development is great. Unlike other estuarine systems where urban development parallels the coast just inland of the mangrove ecotone, Estero Bay is surrounded by expanses of wetland and upland habitat that could serve as accommodation areas as native communities migrate in response to sea level and sedimentation changes. Consequently, there is still time to anticipate the future effects of development on sedimentation and the geomorphic response to sea level rise and adjust management and land-use practices accordingly. It is for these reasons that this investigation was undertaken. This project investigates the environmental and hydrologic history of Estero Bay over the last 5000 years (late Holocene) with the specific intent of helping guide future management and restoration efforts.

The research addresses four central questions:

(1) How has the coast and estuarine-scape evolved through the late Holocene as sea level rise rates have varied? And what are the implications for future environmental

change and restoration? Both the geomorphologic and environmental management implications of sea level rise in Southwest Florida necessitate a firm understanding of this region's late Holocene history. This most recent geologic history provides precedents for the coastal system's response and insights into how Southwest Florida might respond in the future. Arguably an appreciation of this history is even more important in the hands of regional planners, managers, and decision-makers, many of whom have limited experience in environmental science and geology. Lastly, providing a deeper-time database of coastal evolution helps modelers improve the accuracy of predicting future environmental change. This would aid long-range environmental planning and forecasting. A series of hand and vibracores, positioned along on-/offshore transects through the bay and penetrating the Pleistocene and Holocene sedimentary cover to underlying bedrock, was used to interpret the history of estuarine development.

(2) What role has reef development played in this evolution? Because oyster reef development is vital to both Southwest Florida's estuarine ecology and coastal geomorphology, the response of reef development during the Holocene to changes in sea level rise rate is instructive to how the ecology and geomorphology will respond in the future. A set of cores within the Horseshoe Keys region of north-central Estero Bay, the area of greatest present-day reef development, was studied to illuminate the role of reef growth and succession to coastal evolution.

(3) How has fluvial sedimentation and freshwater delivery varied during this time interval? The brackish estuarine environment of Estero Bay presumably reflects historic changes in the delivery of freshwater and fluvial sediments through the late Holocene. The geomorphology of the Imperial River system in southern Estero Bay suggests a prominence of fluvial deposition. The role of fluvial activity in this, and the other two watersheds studied herein (Estero River and Hendry / Mullock Creek), was investigated by positioning cores across the present-day river mouths.

(4) How have sedimentation rates changed over recent history, since human development? Does this reflect changes in watershed management and increased levels of runoff? Sediments are in effect potential pollutants. Consequently, they could be treated as such and be subjected to "total daily maximum load" (TDMLs) constraints. In addition, such data could help establish minimum flows and levels for Estero Bay's rivers

to target specific sedimentation rates or salinities. Sedimentation rates and their change over recent history (< 200 years) were quantified using shallow sediment cores and high-resolution geochronologic techniques using radiogenic isotopes.

Project Scope

Research was focused on 3 study regions within Estero Bay, each reflecting one of the major watersheds entering the bay: (1) Hendry and Mullock Creeks, entering the northern region of the bay; (2) Estero River, entering the north-central portion of the bay; and (3) Imperial River, entering in the south (Figure 9).

The project had 5 principal objectives:

1. Determine the paleoenvironmental context of the late Holocene (< 5000 years) strata preserved in the sedimentary cores taken from Estero Bay through sedimentologic and faunal analyses. The environmental conditions under which sediments are deposited imprint sedimentologic, geochemical, and faunal characteristics that are indicative of those conditions. These characteristics were used to define facies (i.e., sediment packages representing specific sedimentary environments) within each of the cores. Fairly sophisticated interpretations concerning the environment of deposition for each facies were attained, including: aquatic versus terrestrial settings, water depth, energy level due to waves and currents, salinity, and openness or protected-ness of the setting.

2. Refine the paleoenvironmental interpretations through organic geochemical analysis. Stable carbon and nitrogen isotopes ($\delta^{13}C$ and $\delta^{15}N$, respectively), as well as the carbon to nitrogen ratios (C:N) of organic matter were used to further constrain the vegetative sources of organic material present at different depositional locations and times throughout the late Holocene. These data were used to distinguish marine versus non-marine sources of organic matter, vascular versus non-vascular plants and nitrogen-fixing plants (mangroves).

3. Establish both a low (< 5000 years) and high (last 200 years) resolution geochronologic framework for environmental history. A geochronology was established in concert with the paleoenvironmental interpretations of the facies in order to understand environmental change through time. Low resolution dating, providing absolute dates

with +/- 50-year accuracy, was used to establish: rates of sea level rise through the late Holocene (by tracking the height of marine flooding surfaces within cores through time), the timing of appearance of critical depositional environments (e.g., mangrove forests, oyster reefs, open marine settings, and protected embayments), and the first appearance of certain faunas and floras. Radiocarbon and amino acid racemization dating techniques were employed here.

In order to determine recent changes in sedimentation rates, higher resolution, radiometric dating techniques were employed. The radioisotopes lead-210 (^{210}Pb) and cesium-137 (^{137}Cs) provide greater precision (+/- 10-year errors), and therefore permit accurate measurement of sedimentation rates over decadal time scales.

4. Interpret the spatial and temporal distribution of environments over the late Holocene through lithocorrelation and chronocorrelation. After the paleoenvironmental reconstructions and a geochronology were established, the spatial and temporal distribution of environments was mapped through the techniques of litho- and chronocorrelation (i.e., correlating facies that represent comparable depositional environments and the identification of key beds or isochrons deposited synchronously). Fence diagrams were constructed for these purposes.

5. Determine the rates of deposition and the changes in those rates over recent time scales. After a high-resolution geochronology was established for the most recent sediments (< 200 years), sedimentation rates were calculated from the cores.

Methods

Late Holocene History: Field Design and Coring.

Estero Bay was subdivided into 3 watersheds, from north to south: Hendry and Mullock Creeks; Estero River; and Imperial River (Figure 9). These are the 3 most influential watersheds providing freshwater and sediment to the bay and the 3 watersheds most likely affected by past and future development. A coring transect, running along the estuarine axis from the lower reaches of the river into the middle portion of Estero Bay, was located along each of these watersheds (Figures 10 & 11). (GPS coordinates for all coring localities are listed in Table 1.)

Eight cores were taken in the Hendry / Mullock Creek watershed. The transect here was oriented north (onshore) to south (offshore) from the lower reaches of Hendry Creek to the Horseshoe Keys region of the interior of Estero Bay (Figure 10). Five of these cores were used to construct a fence diagram; they are, from north to south: 0205-6, 0207-17, 0206-12, 0206-11, and 0207-16. Positionally these cores represent, respectively: inner region of the inner bay, central region of the inner bay, outer edge of the inner bay, inner region of Estero Bay, and the central region of Estero Bay (Horseshoe Keys). Two cores were located further upstream of the mouth of Hendry Creek (cores 0205-7 & 0308-19), but the strata from these contained mostly river channel deposits and therefore did not provide much insight into sea level rise history. Consequently, these two cores were left off the fence diagram. Finally, core 0206-12 was a recoring of 0205-5. The former provided a more complete section, so it was chosen to represent the outer region of the inner bay within the fence diagram.

A coring transect, running east to west, along the Estero River to infer late Holocene history was established during a preliminary study by Stephanie Obley and Michael Savarese (Obley et al., 2001; Obley, 2002) and consisted originally of 9 cores (Figure 10). They are, from upstream (east) to downstream (west): 9911-4, 9911-3, 0106-10, 0102-1, 0307-13 (replaced original core 9911-1 during this study), 0006-1, 0006-2, 0307-14 (replaced core 0106-9 during this study), and 9911-2. Because newer material was needed to assess the organic geochemistry, two new cores, 0307-13 and 0307-14, were taken during this study and have since replaced their predecessors in the Estero River fence diagram. Two additional cores were taken in the middle reaches of the Estero River, one within a *Juncus* marsh (0212-21) and a second within the river's channel (0102-2). This latter core was disgarded, because it contained a thin veneer of channel sands overlying bedrock. The old cores from the Obley study were redescribed herein and integrated with the new cores taken in this and the other two watersheds.

The history of the Imperial River watershed presented unique challenges to the study. Because human development has shifted the position of the river mouth's entrance to southern Estero Bay (also known as Big Hickory Bay) from east to west, two south to north (on- to offshore) transects were constructed (Figure 11). The first is positioned more easterly and traverses the pre-development mouth of the Imperial River while

running along the proximal eastern edge of Estero Bay; the second is positioned further west and passes through the present mouth of the Imperial River where it enters Big Hickory Bay (of southern Estero Bay) while running along the more distal western edge of Estero Bay (Figure 11). The former is hereafter referred to as the "Imperial inshore transect" and the latter as the "Imperial offshore transect". The inshore fence transect is composed of 5 cores; from south to north they are: 0307-11, 0307-12, 0306-7, 0307-15, and 0306-6. The offshore transect is composed of an additional 5 cores, from south to north: 0406-9, 0307-9, 0306-8, 0306-4, and 0306-6 (this last core serves as the middle Estero Bay anchor for both the inshore and offshore transects).

During the spring and summer of 2004, three additional research needs, requiring coring, were identified. First, the inner bay margin throughout South and Southwest Florida is believed to have remained fixed since approximately 3200 ybp (Wanless & Parkinson, 1989). We suspect that the inner bay margin is presently metastable due to recent acceleration in sea level rise, and could transgress abruptly under the present sea level rise regime. A punctuated transgression of this margin was documented in response to passage of Hurricane Andrew in 1992 along the Highland Beach region of southwestern Everglades National Park (Risi et al., 1995; Tedesco et al., 1995). In order to test the hypothesis of inner bay margin stability and to better predict its future response due to accelerated sea level rise, cores were taken just inshore of the inner bay margins in Hendry Creek (core 0312-31), Estero River (core 0405-6), and Imperial River (core 0405-5) systems (Figures 10 & 11).

Second, the region extending south of Big Hickory Bay, east of Fishtrap Bay, and surrounding the distributary channels of the lower Imperial River is geomorphologically unique for Estero Bay. The question arises as to whether this mangrove-forested region is a product of the same oyster reef progradation as seen elsewhere in Southwest Florida. Or, alternatively, is it a product of deltaic deposition and therefore an effect of the Imperial River? To investigate these possible mechanisms, core 0402-4, located between the new and old mouths of the Imperial River and within the marginal mangrove forest (Figure 11), was taken.

Finally, the cores taken prior to the summer of 2004 were located too proximally to help in the interpretation of barrier island history. Cores taken offshore of the barrier

islands, on the inner or middle shelf, would undoubtedly contain highly reworked sediments with poor stratigraphic completeness and temporal fidelity, making it difficult, if not impossible, to address the timing of barrier island formation. The back-barrier island environment, however, is dominated by depositional rather than erosional processes, and therefore provides greater potential for improved stratigraphic resolution. Consequently, two cores were taken from the back-barrier settings, one in western Fishtrap Bay (core 0408-10) and the other behind Ft. Myers Beach in northern Estero Bay (core 0408-11; Figures 10 & 11).

Sediment long cores were either taken with a hand corer or with a vibracore device (Figures 12 & 13). Late Holocene sediments may reach thicknesses up to 5 meters. Hand cores provide reasonable results for stratigraphic sections less then 2 meters in thickness. Vibracores are needed for thicker sections. Because vibracoring typically instills a greater degree of compaction than hand coring, cores were usually taken by hand until penetration was no longer possible. Coring was then resumed using the vibracore device until bedrock was reached or until the core barrel would no longer twist under human power. (A core barrel that remains "unfrozen" can typically be extracted by hand.)

Three-inch diameter, aluminum irrigation pipe was vibrated into the sediment. Sediment compaction was measured by comparing the height of the sediment inside and outside the pipe. The pipe top was then capped, the pipe extracted, and the core cut to length and sealed for transport back to the laboratory. The distance between the sediment-water interface at the core site and the lowest height of mangrove leaves (representing the mean high tide line) from a neighboring mangrove fringe or island served as a vertical datum against which all cores were compared. This allows the height of sea level to be tracked through time and space. Back at the laboratory, the aluminum pipes were cut using a custom jig and a circular saw fitted with a carbide blade. The cores were then split by hand and readied for sampling and description.

Late Holocene History: Stratigraphic, Sedimentologic, Geochemical, and Faunal Analyses.

Each core was measured and described using standard stratigraphic practices. Facies within each section were recognized from general visual characteristics (color, texture, and grain size; Figure 14). Stratigraphic sections were first drafted by hand and then using the graphics software package Flash to generate stratigraphic columns. Each core was photographed digitally in 25 cm lengths (Appendix D). Half of each core was left untouched for archival purposes and the second half was dedicated to sampling for further analysis.

Each facies of a core was sub-sampled for grain size analysis. A rectangular prism of sediment with dimensions of approximately 5 x 5 x 3 cm (height x width x depth) was removed from one or more stratigraphic heights within a facies for grain size determination. Care was taken to not use sediment adjacent to the core barrel. Samples were dried at 40° C. Grain size distributions (measures of mean grain size, standard deviation [i.e., grain sorting], and skewness) were obtained through use of a laser coulter counter, located at Indiana – Purdue University, Indianapolis. The coulter counter generates percent weight fractions for each Wentworth size category. These data were then used to plot weight percent histograms and cumulative weight percent scatter plots (see examples in Figures 15 & 16; also Appendix B). The Folk graphical method was used from the cumulative weight percent plots to calculate mean size, sorting, and skewness (Boggs 2001).

Similar volumes of sediment were extracted from each shell-bearing facies for faunal analysis. The sediment removed was sieved through 2-mm, 1-mm, and 63-micron stainless-steel screens. Macrofauanal invertebrates (principally gastropod and bivalved mollusks) from the 2-mm fraction were identified to the lowest taxonomic level possible, and the absolute abundance of species was determined by counting occurrences (see Appendix C). Species-level identifications were made by comparison with figured specimens in published guides and monographs (Warmke & Abbott, 1962; Abbott, 1967; Andrews, 1977; Camp et al., 1998; Gundersen, 1998) and through comparison with curated collections from the Bailey-Matthews Shell Museum on Sanibel. Additionally,

identifications were confirmed by Dr. Lynn Wingard, a paleontologist and malacologist from the the U.S. Geological Survey, Reston.

Because the most critical historical environmental characteristic of interest is salinity, mollusks were used as paleosalinity indicators of past environments. A companion study authored by Savarese and Wingard (2004) was used to delineate the ranges of salinity tolerances of living individuals of those molluscan taxa found in the Estero Bay cores. The U.S. Geological Survey has been conducting a faunal and water quality monitoring study of Florida and Biscayne Bays since 1995 (Brewster-Wingard & Ishman, 1999; Wingard et al., 2001, 2003; Wingard, 2004). The species occurring in these bays are identical to those occurring along the Southwest Florida coast. We have assumed these common species have similar salinity tolerances. Data amassed for Florida and Biscayne Bays in an Access database were used to generate salinities and temperatures of occurrence (see sample histogram in Figure 17; Savarese & Wingard, 2004). These will be used in a future analysis to further interpret the paleosalinities of those facies recognized in the Estero cores.

Samples for $\delta^{13}C$ and $\delta^{15}N$ analyses were collected from 18 Estero Bay cores (2 from Estero River, 5 from Hendry Creek and 11 from Imperial River). Although samples for stable isotope geochemical analysis were collected from every facies in each core, it was determined after initial $\delta^{13}C$ and $\delta^{15}N$ results that only samples from organic-rich and peat facies were needed to be analyzed in order to resolve the historical vegetation down core.

Cores were sampled immediately after returning to the lab. Samples were collected using clean (rinsed with 10% HCl and Nanopure water, baked at 550ºC) scoopulas, by scooping the sample from each facie, taking care to avoid any sample in direct contact with the core tube. Samples were stored frozen immediately in clean (baked at 550ºC) glass jars at -20ºC. An aliquot of the sediment samples (~1g wet weight) was sub-sampled and dried in the oven at 60ºC. The dried sediment was ground to a fine powder using a clean (baked at 550°C) mortar and pestle. Visible pieces of shell hash and roots issuing from overlying facies were removed prior to grinding of the sample. The ground sediment was then acidified with 10% hydrochloric acid (Trace Metal grade) to remove any carbonates. These samples were then dried again and

homogenized using clean (baked at 550°C) stirring rods. Micrograms of the dried and acidified samples were weighed into clean (rinsed with acetone) triplicate tin cups and sent to the University of California at Davis Stable Isotope Facility for $\delta^{13}C$ and $\delta^{15}N$ analyses. A total of 189 samples (including triplicates) were analyzed.

The stratigraphic sections from each of the 3 transects and the associated radiocarbon dates (see next subsection) were used to assemble fence diagrams. The process of integrating spatial and temporal data to infer geologic history is conducted through the construction of a fence diagram, a visual tool that displays environmental and temporal data to assist interpretation (see, for example, Figure 28). Cores from each transect were correlated along the on- / offshore transects through each of the 3 watersheds. Comparable facies, representing similar environmental settings, were matched (i.e., lithocorrelation). Radiocarbon dates for critical environmental events were plotted alongside the stratigraphic columns in each fence (i.e., chronocorrelation).

Late Holocene History: Lower Resolution Geochronology.

Two absolute dating techniques were applied to organic components (mollusk shells, wood fragments, or peat fibers) sampled from critical facies. Radiocarbon dating using AMS (accelerator mass spectrometry) techniques was conducted by Beta Analytic, a certified laboratory in Miami that specializes in south Florida applications.

Sedimentologic events for radiocarbon dating must be fore-thoughtfully chosen because of the expense involved. The first appearance of marine influence (i.e., the sea level flooding surface) was dated at two locations per transect. This provided measures of the rate of sea level rise for discrete intervals of the late Holocene in Estero Bay. The timing of appearance of mangrove forests helps differentiate the land- and seascape for particular time intervals. Lastly, the timing of sedimentary progradation, where the coastline is building seaward despite rising sea level, represents the interval during which the Ten Thousand Island geomorphology was established.

The second dating method, amino acid racemization (Goodfriend, 1989), is a technique that has been employed successfully in the past by Savarese to date fossil *Crassostrea virginica*, the American oyster (Lindland et al., 2001; Lindland, 2002). Since oysters are prolific in late Holocene core facies and since these dating analyses are

considerably cheaper than radiocarbon techniques, amino acid racemization is more economical. Unfortunately, the amino acid racemization conducted in 2001 and 2002 was based on a calibration from Dr. Glenn Goodfriend's laboratory at George Washington University and for oysters collected in the Ten Thousand Islands. Dr. Goodfriend passed away tragically in 2003, after this research was proposed and funded. Consequently, the oyster racemization calibration needed to be repeated in a new laboratory and for shells collected from Estero Bay. Dr. Rick Oches, from University of South Florida at Tampa, agreed to collaborate, and a calibration study was undertaken in 2003-2004 in concert with this project (see complete report by Savarese & Oches, 2004).

Calibration data came from a core taken in the Horseshoe Keys within north-central Estero Bay (core number 0209-19; Figure 10). Horseshoe Keys is an area of current reef growth; it has a long history of reef development, dating back to 2690 ybp; and the associated subtidal estuarine history goes back to 5300 ybp (based on AMS radiocarbon dates). Consequently, oysters are common throughout the late Holocene.

Oysters were sampled from 4 stratigraphic horizons that spanned the oyster-bearing length of the core: (1) between 40-60 cm height; (2) between 70-85 cm height; (3) between 140-150 cm height; and (4) between 170-185 cm height (Figure 41). Five, six, two, and four oysters were collected from each horizon respectively. Each oyster was taphonomically graded on a scale from 1 to 4, with one representing a pristinely preserved shell and 4 being a very poorly preserved shell (for taphonomic grading concept see Brandt, 1989). Criteria for grading followed Lindland et al. (2001), Lindland (2002), and Flessa et al. (1993). Shells of poorer grade have a greater likelihood of having been reworked, meaning their stratigraphic position may be erroneous – they would date older than the environment in which they were ultimately entombed. Consequently, only shells with the most pristine grades were ultimately selected for calibration.

Eight oysters, two from each of the four horizons, were selected for racemization analysis and AMS dating. Assuming stratigraphic depth in the core directly correlates with age, the four horizons provide greatest temporal spread and the paired samples from each horizon provides some replication.

Each sample was split into two equal halves. One half was subjected to AMS dating at Beta Analytic, Inc. The other half was analyzed for amino acid content at Dr. Oches' laboratory at University of South Florida, Tampa.

Amino acids, which are optically active molecules, are produced by living organisms in the process of protein synthesis and tissue generation in the L-amino acid (levorotatory or left-handed) configuration. After death the process of racemization begins and L-amino acids stereochemically invert about their central carbon atom, forming their D-amino acid (dextrorotatory or right-handed) isomer. In mollusks, including oysters, amino acids are formed in the biomineralization process of shell formation and are well preserved within the primary calcite or aragonite structure of the shells.

Amino acid geochronology refers to the measurement of the ratio of D- to L-amino acids. Typically, living organisms are comprised of 100% L-amino acids. Once isolated from living tissue, racemization begins and progresses to an equilibrium D/L ratio of 1.0 for most amino acids. Therefore, the D/L ratio of individual amino acids can be used to approximate time since death of an organism. Because of the sensitivity of the racemization reaction to environmental temperature, which is unknown for most pre-modern samples, the method is most effectively applied as a relative dating tool. Calibrating the racemization progression with an independent dating method, such as radiocarbon dating, can provide a racemization-based numerical dating technique that is applicable to samples whose post-depositional thermal histories are similar to the calibration samples.

D/L ratios were measured for 5 amino acids: aspartic acid (Asp), glutamic acid (Glu), valine (Val), phenylalanine (Phe), and alloisoleucine / isoleucine (A/I). Generally Phe and A/I have the greatest variability; aspartic acid racemizes quickly and is, therefore, only good for short durations (< 1000 ybp); Glu and Val racemize at rates that are most compatible with our time range of up to 5000 years of history.

Oyster fragments selected for amino acid racemization, weighing approximately 100-200 mg, were cut from the thickest part of the hinge or umbo region of the shell. The outer layers were mechanically removed, and approximately 50% of the remaining fragment was dissolved in 2N HCl to remove any adhering contaminating material from

the exposed surfaces. The remaining fragment was rinsed in ultra-purified H_2O, dried, weighed to the nearest 0.1 mg, and placed in a sterile 2ml glass vial. Samples were then dissolved in 7N HCl in the proportion 0.2ml HCl/mg shell. The vial containing the acidified solution was flushed with N_2, capped, and placed in an oven at 110° C for 6 hours to liberate amino acids from peptide chains. Following this hydrolysis step, the solution was placed in an evaporator where the liquid was dried under flowing N_2 gas in an 80° C heating block. The residual powder was then rehydrated with purified H_2O adjusted to pH 2.00. Finally, 200 microliter samples were transferred to autosampler vials and loaded onto an Agilent 1100 liquid chromatograph, operated using HP Chemstation software.

Analysis of D- and L-isomers of the 5 different amino acids was completed using reverse-phase liquid chromatography, following the method of Kaufman and Manley (1998). Amino acids were derivitized using O-phthalaldehyde + IBLC, injected onto a 250 x 5mm column containing 5 micrometer C18 resin, followed by fluorescence detection. Three mobile phase solutions were pumped on a gradient through the system: mobile phase A = 23 mM Na-acetate buffer, mobile phase B = methanol, and mobile phase C = acetonitrile. An interlaboratory comparison standard was analyzed daily to check for analyzer consistency.

Calibrated-intercept radiocarbon ages from Beta Analytic were regressed against D/L Glu. Three replicate racemization analyses were run for each shell, and the means were used in the regression. A linear regression model was employed; the D/L progression is typically linear for glutamic acid. Because there is some laboratory-induced racemization in the preparation process, the calibration curve does not go through zero; an oyster with an age of "zero" would have a slightly positive D/L ratio. Consequently, the linear regression was not forced to have a y-intercept of zero.

After the calibration equation of glutamic acid was established, it was used to date oysters collected from other cores. In all, 25 oysters from as many different facies were removed from the cores, were taphonomically graded, and subjected to amino acid racemization analysis. D/L Glu ratios were converted to absolute ages using the calibration equation.

Oyster Reef History.

Many of the cores throughout Estero Bay, in all 3 watersheds, were taken from existing oyster reefs or passed through oyster reef facies in the subsurface. These provided insights into reef history, but that information was anecdotal and lacked forethought of experimental design. To better understand the history of reef development, the Horseshoe Keys region of north-central Estero Bay was targeted for coring (Figure 18). Three cores were positioned in the northern Horseshoe Keys (Figure 19). Two of these were located intertidally along the reef crest (cores 0207-16 & 0209-19), separated north to south by approximately 100 m. The third core (0209-18) was positioned on the leeward side of the north crest locality (0207-16) within a subtidal flanking facies.

The Horseshoe Keys reef cores were studied using identical stratigraphic, sedimentologic, and faunal techniques described above for the late Holocene history cores.

Recent Sedimentation Rates.

Field Design.-- Reconstruction of recent geochronology for shallow bay sediment, for the determination of recent sedimentation rates, is complicated by physical and biological mixing of the sediment, low natural activities of the useful radionuclides (common to sandy sediment), missing layers of sediment (e.g., hurricane disturbance in Florida), and other potential problems. Because each region of the bay has a different set of problems and a different likelihood for success, we undertook a pilot study of recent geochronology and worked on a limited number of cores to test the applicability of the methods. Dr. Trefry of Florida Institute of Technology has had success doing comparable work in the lower Everglades and Florida Bay (e.g., Kang et al., 2000), and he oversaw this portion of the research effort.

In order to prospect for the most promising cores, surface samples were taken from 21 localities throughout Estero Bay to test for levels of radiogenic activity (Figures 20 & 21). Those surface sediments exhibiting the highest radiogenic activities are most likely to provide high-resolution geochronologies. Those samples were analyzed in Dr. Trefry's laboratory at FIT, and the most promising sites were identified. Four of those

sites, 2 in each of the Hendry / Mullock and Imperial waterways, were cored. Of the 4, the 2 best-stratified, mud-dominated cores were chosen for final analysis. Site 16 in northern and site 22 in southern Estero Bay were ultimately selected for study (Figures 20 & 21).

Sampling and Initial Processing. -- Sediment cores were collected by a diver. In each case, the sediment was collected by pushing a 7-cm diameter, 50-cm long, cellulose acetate butyrate (CAB) tube into the sediment (Figure 22). After collection, a rubber stopper was placed in the bottom of the core tube and plastic caps were taped onto each end of the core. The cores were kept upright throughout the sampling and recovery operations. Each core was returned to the laboratory at Florida Gulf Coast University and sub-sampled within 24 hours.

Sediment cores were sub-sectioned in 0.5-cm intervals over the top 10 cm and in 1- to 2-cm intervals through the remainder of the core. The sediment was extruded by pushing up on the stopper inside the CAB tubing with soda cans while the core was supported in a wooden rack (Figure 23). The outer few millimeters of sediment that may have been smeared during extrusion were scraped away with a small Teflon spatula and the remaining sediment was placed in a pre-weighed polystyrene vial. The vial with wet sediment was reweighed.

The samples were then transported to Florida Institute of Technology (FIT) and stored frozen until further processing. Initially, the frozen sediment was freeze-dried for ~48 hours to a constant weight. Previous testing has shown that the freeze-drying process is 100% compatible with drying at 105° C with respect to water removal. The freeze-dried samples were re-weighed to determine the water content. Then, the dried sediment samples were homogenized using a Teflon® mixing rod.

Total Aluminum (Al). -- About 50 mg of freeze-dried, homogenized sediment and the certified reference material (CRM) MESS-2 (a marine sediment issued by the National Research Council of Canada) were totally digested in Teflon® beakers using concentrated, high-purity acids following the method of Trefry and Metz (1984). In the digestion process, 1 mL perchloric acid ($HClO_4$), 1 mL nitric acid (HNO_3), and 3 mL hydrofluoric acid (HF) were added to the sediment in the Teflon® beaker, covered with a Teflon® watch cover, and heated at 50° C until a moist paste formed. The mixture was

heated for another 3 hours at 80° C with an additional 2 mL HNO_3 and 3 mL HF before bringing the sample to dryness. Finally, 1 mL HNO_3 and about 30 mL distilled-deionized water (DDW) were added to the sample and heated strongly to dissolve perchlorate salts and reduce the volume. The completely dissolved and clear samples were diluted to 20 mL with DDW.

Labware used in the digestion process was acid-washed with hot, 8N HNO_3 and rinsed three times with DDW. Two procedural blanks, two duplicate samples, and two CRMs were prepared with each set of 20 samples.

Sediment samples, CRMs, and procedural and reagent blanks were analyzed by flame atomic absorption spectrometry (FAAS). The method used is based on the USEPA method described for Series 7000. Analysis was carried out using a Perkin-Elmer model 4000 FAAS with a nitrous oxide-acetylene flame.

Calcium Carbonate ($CaCO_3$). -- The calcium carbonate content of the sediment was determined using the carbonate bomb technique of Schink et al. (1978). The carbonate bomb is a gasometric device that measures the amount of CO_2 produced when a sample is treated with 6N HCl. Initially, variable amount of pure $CaCO_3$ (0.10 to 1.00 g) were reacted with 18 mL of 6N HCl to obtain a calibration curve. The calibration curve consisted of plotting the pressure change (amount of evolved CO_2 and measured manometrically) versus mass of $CaCO_3$. Next, the $CaCO_3$ content of the sediment samples was determined by adding acid to 1.00-g samples and measuring the resulting pressure change. The percent $CaCO_3$ was obtained using the calibration curve and multiplying the fraction by 100.

Total Organic Carbon (TOC). -- A 0.5 to 1 gram portion of the freeze-dried sediment was placed in a 20-mL Pyrex® beaker. Five mL of 10% phosphoric acid (H_3PO_4) were added to remove any inorganic carbon present. The sediment was dried at 60°C and re-weighed to determine the increase in mass due to the formation of calcium phosphate from adding H_3PO_4. Then, approximately 200 to 400 mg of pre-treated sediment were weighed into ceramic boats and combusted at 900°C in a Shimadzu® TOC-5050A carbon system with SSM-5000A solid sampling module following the manufacturer's instructions. The TOC content of the sediment samples was determined using a four-point calibration curve with pure sucrose as the standard. The TOC

concentrations were corrected to account for the increase in sediment mass following the addition of H_3PO_4. The calibration curve was checked every 10 samples by analyzing the CRM MESS-2.

Radionuclides. -- Approximately 8-10 grams of freeze dried sediment from each layer (0.5-cm or 1-cm thick) of the sediment cores were ground to a fine powder using a Spex 8000 mixer mill. The samples were then tightly packed into 2-cm diameter, 5-cm long polycarbonate vials to a depth of 30±1 mm. A rubber stopper was cemented into place in the vial with two-part epoxy to prevent leakage of ^{222}Rn and disruption of secular equilibrium between ^{226}Ra and ^{210}Pb. The samples were then set aside for at least 20 days to establish secular equilibrium.

The activities of ^{210}Pb, ^{214}Pb, ^{214}Bi and ^{137}Cs were determined using a well-type, intrinsic germanium detector (WiGe, Princeton Gamma Tech). Vials containing about 10 g of freeze-dried sediment were counted for about 2 days until all peak areas were sufficient to provide <10% counting error. Detector efficiency was determined using the following: NBS 4350B, river sediment and NBS 4354, freshwater lake sediment from National Institute of Standards and Technology (NIST) and standards RGU-1 and RGTh-1 from the International Atomic Energy Agency. The specific activity (dpm/g) of each sediment sample was calculated from the detector efficiency, gamma intensity, geometry factor, and sample weight. All values are reported as the activity on the date of coring. Errors are shown on the basis of ±1-sigma counting statistics.

Quality Assurance and Quality Control.-- All sediment samples were collected by, transported by, and stored by personnel from FIT. Upon return to or arrival at the laboratory, each sample was carefully inspected to insure that it was intact and that the identification number was clearly readable.

For this project, QC measures included balance calibration, instrument calibration (FAAS, TOC analyzer, gamma spectrometer), matrix spike analysis for Al, duplicate sample analysis, analysis of CRMs, procedural blank analysis, and standard checks. Data quality objectives (DQOs) for these quality control measurements are given in Table 2.

Electronic balances used for weighing samples and reagents were calibrated prior to each use with certified NIST-traceable standard weights. All pipettes (electronic or

manual) were calibrated prior to use. The FAA used for Al analysis was initially standardized with a three- to five-point calibration; a linear correlation coefficient of $r \geq 0.999$ was required before experimental samples were analyzed. Analysis of complete three- to five-point calibrations and/or single standard checks alternated every 5-10 samples until all the analyses were complete. The relative standard deviation (RSD) between complete calibration and standard check was required to be <15% or recalibration and reanalysis of the affected samples were performed.

Matrix spikes were prepared for a minimum of 5% of the total number of samples analyzed and included each metal to be determined. Results from matrix spike analysis using the method of standard additions provide information on the extent of any signal suppression or enhancement due to the sample matrix. If necessary (i.e., spike results outside 80-120% limit), spiking frequency was increased to 20% and a correction applied to the metal concentrations of the experimental samples.

Duplicate samples from homogenized field samples (as distinct from field replicates) were prepared in the laboratory for a minimum of 5% of the total samples. These laboratory duplicates were included as part of each set of sample digestions and analyses and provide a measure of analytical precision.

Two procedural blanks were prepared with each set of 20 samples to monitor potential contamination resulting from laboratory reagents, glassware, and processing procedures. These blanks were processed using the same analytical scheme, reagents, and handling techniques as used for the experimental samples.

A common method used to evaluate the accuracy of environmental data is to analyze reference materials, samples for which consensus or "accepted" analyte concentrations exist. The CRMs and SRMs were listed above with the pertinent methods. The complete data for reference materials are tabulated in the appendix (see separate report by Trefry et al.).

Data for all QA/QC measurements are given with the complete data sets in the attached appendix. All DQOs for this project were met (also shown in the attached appendix).

Calculating Sedimentation Rates.-- Sedimentation rates (S) in cm/yr were initially calculated using the following equations:

^{210}Pb:

$$S = \frac{\text{(-) decay constant for } ^{210}\text{Pb-210 (0.0311 yr}^{-1}\text{)}}{\text{Slope for plot of natural logarithm (ln) excess } ^{210}\text{Pb vs. sediment depth}} \quad \text{Eq. 1}$$

^{137}Cs:

$$S = \frac{\text{Depth in cm at which Activity } ^{137}\text{Cs = zero (i.e., below MDL)}}{\text{[Year – (1950)] in years}} \quad \text{Eq. 2}$$

The activity of excess ^{210}Pb is calculated by subtracting the mean of A(^{214}Pb, ^{214}Bi) from A(total ^{210}Pb). The activities of ^{214}Pb and ^{214}Bi are assumed to be in secular equilibrium with ^{226}Ra.

In addition, sediment accumulation rates and sediment ages were determined using two different models, the constant initial concentration (CIC) and the constant rate of supply (CRS) of excess ^{210}Pb (where excess ^{210}Pb = total ^{210}Pb – ^{226}Ra). The CIC model assumes a constant initial concentration of excess ^{210}Pb and constant sedimentation rates over time (Krishnaswami et al., 1971; Koide et al., 1973; Robbins and Edgington 1975). If this assumption is valid, excess ^{210}Pb activity (A in dpm/g) at a certain depth can be initially described by the basic radioactive decay law as follows:

$$A = A_o e^{-\lambda t} \quad \text{Eq. 3}$$

where A_o is the excess ^{210}Pb activity at the sediment-water interface, λ is the decay constant of ^{210}Pb and t is time.

The cumulative dry mass (M_c) in g/cm^2 is obtained by the following equation:

$$M_c = \sum_{i=1}^{n} \rho_i d_i \quad \text{Eq. 4}$$

$$\rho_i = \rho_s (1-\phi) \quad \text{Eq. 5}$$

where M_c is the cumulative dry mass (g/cm^2), ρ_i represents the dry density (g/cm^3) at i_{th} depth of core sediment as shown in Eq. 3, where ρ_s is the average density of sediment and ϕ is porosity at sediment depth, and d_i is the thickness of the i_{th} depth interval (cm). After substituting $t = M_c/S$, where S is the sediment accumulation rate (g/cm^2/yr), Eq. 3 can be rewritten as follows:

$$\ln A = \ln A_o - (\lambda/S)M_c \qquad \text{Eq. 6}$$

The sediment accumulation rate (S) for each core can be calculated from the slope of the best-fit linear equation between cumulative dry mass and excess ^{210}Pb activity from Eq. 6. The age at a certain depth is estimated by dividing cumulative dry mass by the mean sediment accumulation rate.

The CRS model assumes a constant supply of excess ^{210}Pb, but variable inputs of dry sediment (Appleby & Oldfield 1978; Hermanson 1990). If these assumptions are satisfied, then the integrated inventory (I) of excess ^{210}Pb beneath sediment of age t is

$$I = I_{Total}\, e^{-\lambda t} \qquad \text{Eq. 7}$$

where I_{Total} is the total inventory of excess ^{210}Pb in the sediment column (dpm/cm^2), λ is the decay constant of ^{210}Pb, and t is time. The total inventory of excess ^{210}Pb can be calculated from the following:

$$I_{Total} = \sum_{i=1}^{n} A_i M_i \qquad \text{Eq. 8}$$

where A_i is the activity of excess ^{210}Pb at depth i and M_i is the dry mass (g/cm^3) at the thickness of the i_{th} depth interval. The sediment age (t) at the i_{th} depth interval is calculated using Eq. 9.

$$t = \frac{1}{\lambda} \ln\left(\frac{I_{Total}}{I}\right) \qquad \text{Eq. 9}$$

Results & Discussion

Late Holocene History: Facies Present and Their Paleoenvironmental Interpretation.

Sedimentologic, faunal, and taphonomic characteristics of the sediments within the late Holocene cores resulted in the identification of 11 facies. Those representative characteristics and their paleoenvironmental interpretations are as follows:

1. Regolith. These sediments are consistently found at the base of a sediment core immediately above the bedrock basement. The material making up the facies is weathered limestone, probably belonging to the Pliocene Tamiami Formation. Limestone cobbles, pebbles, and gravel are floating within either a clay- or sand-rich matrix. Clays may or may not be composed of carbonate, suggesting if the latter they represent dissolution lags. The color of the matrix is light, either a light gray, blue-gray, or white. Fossils may be present, but these usually have a limestone matrix adhering to them, indicating they are also weathered from the underlying bedrock.

This facies is interpreted to be a basal soil horizon that developed on top of a limestone bedrock surface. Although no ages were obtained from the regolith, it presumably is Plio-Pleistocene in age. The interval is unconformable and represents a long-duration exposure surface prior to late Holocene marine flooding. Regolith is color-coded tan on the fence diagrams.

2. Freshwater peat. The plant organics composing this facies are very different from those in facies 5 (mangrove peats). Organics here are granular rather than fibrous, and plant tissues are not readily identifiable macroscopically. These beds are also thinly bedded, again in contrast to the mangrove peats. Sediment matrix may be quartz sand or marly carbonate mud. When found, they are interbedded among supratidal sands.

The granular texture, stratigraphic position, and marly matrix are all consistent with a freshwater wetland origin for these peats. Granular textures are common in grass prairie soils, and prairies often have periphyton algal-generated calcitic muds. This peat is also never found under- or overlying an estuarine or intertidally influenced facies, suggesting the environmental setting was well-removed from marine influence. The

facies is therefore interpreted to represent a "freshwater wetland". Freshwater peat is color-coded dark green on the fence diagrams.

3. Riverine sediments. Sediments within this facies are sand-rich where the sands are very fine- to medium-grained. Muds may be present, but if so, they compose a minor fraction. Fibrous and speckled organics are common and are found somewhat uniformly throughout the strata. Estuarine shells are uncommon (the localities are positioned near the bay, so the likelihood of finding freshwater mollusks is low). Often the base of the facies is erosional with a shell-rich lag deposit marking onset of this facies' deposition. Cross laminations are difficult to discern in any core simply because the core barrel is narrow and disruption of sediments along the barrel margin during the coring process is likely to obliterate those structures. This facies, however, does show subtle indications of cross laminations.

The erosional disconformable base of this facies, coupled with the sediment grain size and texture indicate this facies represents a fluvial setting. The facies may represent a channel, point bar, or deltaic setting. Fluvial sequences are often initiated on top of unconformable surfaces; river deposition usually follows a period of erosion. The sediments overlying the disconformity were deposited as bed load with traction transport generating the cross laminations. The lower reaches of the present-day rivers entering Estero Bay contain estuarine faunas and can have intertidal mud/sand flats or oyster reefs associated with them. Riverine sediment is color-coded yellow on the fence diagrams.

4. Supratidal / subaerial sands. Sands of this facies can have variable grain size, ranging from fine to coarse. Colors are typically light to medium gray, yellow, or brown. Plant-derived organics are common and may reach concentrations of peat (i.e., incipient peat). Organics can be homogenously distributed, mottled throughout, or concentrated in laminations. Muds may occur, often as clots or as soil peds. Upper contacts are often gradational into mangrove peats. Vertical roots or root casts commonly penetrate from above. Carbonate shells are usually absent.

The absence of a shelly fauna, the presence of organics, roots, and root casts, the oxidized iron staining (yielding yellow or brown colors), and the mud clots all indicate this facies represents a supratidal, subaerial environment. These features are consistent

with those found in the lower horizons of a soil profile. Given the lack of marly sediments and relative low concentration of organics, this environment probably reflects an upland forest setting. Supratidal, subaerial sands are color-coded orange-brown on the fence diagrams.

5. Intertidal, mangrove peats. These sediments are dominated by plant organics that are well preserved. Decay has not obliterated organic tissues, and plant parts are readily identifiable from gross morphology or through plant histology (though the latter was not undertaken in this study). Organics are typically composed of fibrous root hairs, root sheaths, and roots, some of which may have solid or spongy textures; rarely are leaves present. Roots and root sheaths may be horizontal or vertical. If vertical, they may penetrate underlying facies to considerable distances. Roots were found as deep as 1 meter below the overlying bearing peats. The sedimentary matrix surrounding the organics can be composed of carbonate mud or quartz sand. Color is typically a dark gray, brown, or black. Estuarine shells may be present, but if so in low abundance. Preservation of shells is commonly poor; shells are usually fragmented. The sediments may also be burrowed either contemporaneously or later after a marine facies overlies the peat. If the latter is present, discrete burrows can be seen originating in the overlying facies and penetrating the underlying peat.

The plant matter composing the peats is consistent with the material produced in the root zone of mangrove forests. The root hairs and root shapes and textures are consistent with those of the red mangrove, though it is not possible without histologic work to differentiate red mangroves from other species of mangrove (black and white). Given the high concentration of organics within the facies, these probably represent red mangrove forests which typically produce denser organic peats than other forest types. There is clear indication that these peats represent intertidal wetlands. Mangroves, particularly reds, require some marine influence. In addition, estuarine mollusk shells are present, as are burrows, both of which indicate at least intermittent wetting at high tide. The facies typically overlies, at least when found at the base of a stratigraphic section, a supratidal sand and underlies a subtidal estuarine facies. This relative position indicates these lower peats represent the basal transgressive marine deposits of a transgressive sequence – the peat represents the initiation of marine flooding of the landscape. This

facies is therefore interpreted as an "intertidal mangrove peat". When positioned with respect to supra- and subjacent facies as described above, the peat represents a basal transgressive environment. Intertidal, mangrove peat is color-coded medium green on the fence diagrams.

6. Intertidal mud or sand flats. This facies lacks diagnostic features and is therefore only interpretable when it occurs at the top of a core. (When the core is taken in a modern intertidal mud or sand flat, the core's uppermost facies must represent this environment.) It is included in the analysis because when this facies occurs, it sits as part of the progradational sediment package that contributes to the mosaic regression of the coast (see further discussion below). The intertidal mud or sand flat facies is color-coded red on the fence diagrams.

7. Organic-rich, shell-poor subtidal sands and muds. Sediments from this facies are either sands (fine- to medium-grained) or muddy sands. If the latter, sands always dominate. Color ranges from light to medium gray. Organics are common and may be found disseminated uniformly or concentrated as interlaminations with sand-dominated laminations. Mollusk shells do occur, but are rare. Discrete burrows or mottled bioturbation fabrics can occur, but are never as common as in the "shell-rich, subtidal sand and mud" facies (facies 8).

This facies is interpreted as representing a subtidal, low brackish water setting, probably located some distance up one of the rivers. The few or near lack of marine water indicators, such as mollusk shells and bioturbation fabrics or discrete burrows, is consistent with a lower salinity estuarine setting. This interpretation is also consistent relative to the position of sub- and suprajacent facies within transgressing or regressing sequences. The "organic-rich, shell-poor subtidal sand and mud" facies is color-coded dark blue in the fence diagrams.

8. Shell-rich, subtidal sands and muds. Sediments in this facies may be sandy muds to muddy sands. Color ranges from light to dark gray. Mollusk shells are very common to abundant and can vary significant in the quality of their preservation. Taxonomic diversity is high, with many species of bivalves and gastropods represented. Shell beds are common and may represent time-averaged or transported assemblages.

Mottled bedding, caused by bioturbation, and discrete burrows are common. The facies can be interlaminated with muddy and sandy laminations. Sorting is commonly poor, particularly in the mottled portions of the facies.

The mix of sands and muds indicates that both bed- and suspended-loads are deposited in this environment. The presence of shell beds and coarser laminations suggests a subtidal environment, but one that is commonly influenced by both normal and storm wave activity. The fine and coarse interlaminations indicate a waxing and wanning tidal influence. High degree of infaunal activity homogenizes the sediment, destroying the interlaminations, and thereby generating poorly sorted sediments. Mottled bedding and deep, discrete vertical burrows suggest the bottom waters were well oxygenated, probably due to tidal mixing. The higher diversity fauna, the deep infaunal activity, and the variable taphonomic characteristics indicate that this environment was of greater salinity than the "organic-rich, shell-poor subtidal" facies (facies 7), perhaps representing a high brackish water salinity, and of greater variable energy than facies 7. This facies is color-coded purple in the fence diagrams.

9. Marine subtidal vermetiform gastropod reefs. This facies is composed of highly fossiliferous sands and gravels. Sands are composed of either quartz or skeletal fragments and are fine- to coarse-grained; gravels are composed of skeletal carbonate and dominated by vermetiform gastropod shell fragments. Shell hash beds and beds composed of valves and valve fragments are common. The molluscan fauna is diverse, with numerous species of bivalves and gastropods present. In addition, crab limb and chela fragments and barnacle plates are common. The most common taxa are two genera of vermetiform gastropods: *Vermicularia*, belonging to the family Turritellidae (Figure 24); and *Vermetus*, belonging to the family Vermitidae. Both have evolute coiling shells as adults and consequently a sedentary life mode. Shells can grow as dense mats to form reefal boundstones. These surfaces serve as hard substrate for the attachment of other organisms (e.g., oysters, barnacles, byssally attached mussels, serpulid worm tubes). Vermetiform gastropod and other mollusk shells exhibit high degrees of encrustation and biocorrosion; the endobiont sponge, *Cliona*, is particularly common.

This environment is interpreted to be near marine in its salinity and of relatively high energy, suggesting a well marine-influenced and open, unprotected coast. Modern vermetiform gastropods, including those belonging to these same species, are intolerant of brackish waters and thrive best in marine or near-marine conditions. In addition, vermetiform reefs are often found on more wave-influenced, exposed coasts. The taphonomic characteristics of the assemblage are consistent with this interpretation. The vermetiform boundstone clumps are formidable structures and could easily have resisted wave influences. Relict vermetiform reefs are found today along the exposed coast of the Ten Thousand Islands (Shier, 1969). The presence of a rich epifaunal and endobiont community is also indicative of normal marine salinity. These encrustors and borers are more common in marine settings; *Cliona*, in particular, is intolerant of brackish water conditions and of subaerial exposure at low tide (Hopkins, 1956; 1962).

Of the 3 subtidal facies (facies 7, 8, and 9), this facies represents the most marine and most exposed, open coastal environment. The "vermetiform gastropod reef" facies is color-coded pink in the fence diagrams.

10. High brackish, oyster – vermetiform gastropod reefs. This facies is very similar in its sedimentologic, paleontologic, and taphonomic characteristics as the vermetiform-dominated subtidal reef facies (facies 9). The principal difference is the increase in abundance of the oyster, *Crassostrea virginica*, relative to the vermetiform gastropods. Oysters become more common and vermetiform gastropods less so. Shell beds and shell hash beds still occur, but are less numerous and less thick. Carbonate mud may appear, generating muddy sand textures.

Because *Crassostrea virginica* maximizes its growth and reproductive output in polyhaline settings, this facies is believed to represent a slightly lower salinity environment than the vermetiform-dominated reef environment. This environment, however, was probably closer to the 30 ppt end-member of the polyhaline distribution than the 18 ppt end-member. The appearance of mud may indicate a quieter setting or perhaps merely reflects greater suspension feeding activity by the oysters. The taphonomic characteristics and the less-prolific nature of the shell beds also indicate a

slightly more protected-water surrounding than seen in the vermetiform-dominated reef. This facies is color-coded magenta in the fence diagrams.

11. Brackish intertidal oyster reefs. The sediments making up this facies are carbonate mud-dominated, though quartz sands do occur subordinately. Mud is often found as pelloids. Color ranges from medium to dark gray. The American oyster, *Crassostrea virginica*, dominates the fossil assemblage. Many oysters are found still articulated; others occur as clumps; and many have pristine taphonomic grades. Oysters, however, are also commonly found as single valves, as fragments, and with poor taphonomic grades. A diverse assemblage of bivalves and gastropods can co-occur with the oysters.

By analogy with modern oyster reef environments in Southwest Florida, this facies is interpreted to represent a brackish water intertidal oyster reef. Modern oyster reefs with most prolific growth develop in medial brackish environments and are exposed to air at low tide. The sedimentologic, taphonomic, and paleontologic characteristics of this facies are identical to those found in modern oyster reef settings. This facies is color-coded light blue in the fence diagrams.

Late Holocene History: Stratigraphy and Trangressive / Regressive Sequences.

Two distinct patterns exist between those cores located within the inner, eastern half of Estero Bay (herein referred to as proximal cores) and the outer, western half of the bay (herein referred to as distal cores).

The inner cores have a simpler stratigraphy, consisting of one transgressive / regressive sequence. The sequence begins with a regolith horizon sitting on top of bedrock. Above this invariably sits a thick package of supratidal / subaerial sediments. Materials for radiocarbon dating are generally absent from the supratidal facies, and, if the package predates 50,000 ybp, the half-life of ^{14}C is insufficient to provide reliable dates. A thin horizon of well-preserved bivalve shells was found in this facies within core 0307-10 at a depth of 340 cm within the core (Appendix A). The shells were preserved well enough to assume they had not been extensively reworked. A

conventional radiocarbon age of 43,540 ybp was obtained, indicating that at least some occurrences of the supratidal facies date from the late Pleistocene.

A mangrove, intertidal peat commonly sits above the supratidal facies within the proximal cores. This facies represents the basal marine-influenced deposit of the transgressive half of the sequence (i.e., the basal transgressive peat). Calibrated radiocarbon dates of these peats can date anywhere within the late Holocene. Dates are as old as 5385 ybp in more offshore, proximal settings (for example in Big Hickory Bay; see core 0306-8 in Appendix A) or as young as 1260 ybp from inshore, proximal settings (for example at the mouth of the Estero River; see core 0307-13, Appendix A). The thickness of the peat is often truncated by erosion, with a thin shell bed sitting directly at the contact with the overlying unit. The mangrove peat can be absent altogether at the base of the transgressive package. If so, however, the upper contact of the supratidal facies is sharp, suggesting the presence of a major erosional unconformity. In such situations, a storm-derived shell bed often punctuates the beginning of the transgressive package (see, for example, horizon G in core 0307-10; Figure 27).

The transgressive package then proceeds through a series of progressively more marine or progressively more subtidal facies. The logical ordering of the pattern is maintained, although specific facies may be missing from the succession. For example, the peat is often overlain by the shell-rich subtidal facies (exemplified by core 0206-12; Figure 25). Alternatively, the more freshwater influenced organic-rich, shell-poor subtidal sands and muds may be found above the peat and underlying a younger shell-rich subtidal facies. This pattern is particularly evident among cores from the Estero River transect (see cores 9911-2, 0307-14, 0006-2, and 0006-1; Appendix A), and occasionally occurs among cores from the Imperial River transects (cores 0306-4 and 0306-6; Appendix A). In yet other cores, the brackish, intertidal oyster reef facies may directly overlie the peat or the unconformity where the peat use to be. This is evident in core 0307-9 (Figure 27) and core 0207-17 (Appendix A).

The marine transgression culminates in some sections with the most marine influenced vermetiform gastropod reef facies. This is seen in cores from the Horseshoe

Keys (cores 0209-18, 0207-16, and 0209-19; Appendix A) and from core 0307-9 from the Imperial River transect (Figure 27).

The regressive package of the sequence in the proximal cores exhibits a predictable pattern as well in the stacking of facies. The regression, because of its more recent history, is observable in cores taken in modern intertidal or supratidal settings (e.g., on or adjacent to inner bay islands or on modern oyster reefs). Modern subtidal settings are in regions that have yet to be affected by the mosaic regression. Facies become progressively more intertidal or supratidal or exhibit greater degrees of influence by freshwater. In some situations, the shell-rich subtidal facies is overlain by the brackish, intertidal oyster reef facies (cores 0206-12 and 0207-17; Figures 25 & 26, respectively). In others, specifically those from the Horseshoe Keys, the reef facies exhibit an environmental succession where the waters become progressively more freshwater influenced (discussed in later subsection). Finally in yet others, the organic-rich, shell-poor facies sits atop the package, suggesting the return of river influence (for example, see core 0307-13; Appendix A).

Cores taken on mangrove-forested inner bay islands show the classic progradational sequence first recognized by Parkinson (1989). Core 0402-4, taken from the forested region between the new and old mouths of the Imperial River, exhibits this progradational stratigraphy (Appendix A). The transgressive package culminates with shell-rich subtidal sands. These are then overlain by the brackish, intertidal oyster reef facies and then regressive mangrove peats.

The oldest date obtained to constrain the timing of the regressive phase is the calibrated radiocarbon age of 2880 ybp. This date comes from core 9911-2 and is located at the transition from the high brackish, oyster – vermetiform gastropod reef facies and the brackish, intertidal oyster reef facies (Appendix A). The transition to regressive progradation dates between 2350-2690 ybp for the Horseshoe Keys reef sites (core 0209-18 and 0209-19). The remaining radiocarbon ages obtained for the regressive phase are all younger than these. These dates for the progradation are all consistent with the timing of phase 2 of the late Holocene sea level curve compiled by Wanless et al. (1994; Figure 1). If these dates are compared against the more refined sea level curve compiled by

Gelsanliter and Wanless (1995; Figure 2), the progradation phase overlaps with the right-most, shallowly sloping line segment of the curve.

Figures 25 and 26 illustrate the typical sequence of transgressing and regressing strata from proximally positioned cores.

Distally positioned cores, in addition to exhibited this younger late Holocene transgressive – regressive cycle, can show evidence of older transgressive – regressive cycle. Core 0307-9, from middle region of Fishtrap Bay along the Imperial offshore transect (Figure 27), has a brackish, intertidal oyster reef facies and suprajacent shell-rich subtidal facies both underlying the supratidal / subaerial sands. This indicates some portions of the present-day distal coast were inundated with estuarine waters at some earlier date. Unfortunately, no radiocarbon dates are available for this material. A similar older transgressive – regressive cycle, however, has been discovered in the distal coastal setting of the Ten Thousand Islands, and calibrated radiocarbon dates from here go back to 5500 ybp (Savarese, unpublished data).

Late Holocene History: Isotope Geochemistry.

Stable isotope and C:N ratio results from this study were used as an additional tool to further constrain the sources of organic matter during different depositional times throughout the late Holocene. Analyses results are available from 14 core localities from Estero River (cores 0212-21, 0307-13, and 0307-14), Hendry Creek (cores 0206-11, 0206-12, 0207-16, 0207-17, and 0312-31) and Imperial River (cores 0306-4, 0306-8, 0307-9, 0307-10, 0307-11, and 0307-12). Isotopic values are plotted alongside the stratigraphic columns for these localities in Appendix A. Only data from organic-rich and peat facies will be discussed here.

Organic matter C:N ratios from this study ranged from 19 to 81, with majority of the samples having ratios greater than 20, indicating that vascular plant material is the predominant source of organic matter within these cores (Cloern et al., 2002). Organic matter $\delta^{13}C$ signatures ranged from -31‰ to -21‰, while $\delta^{15}N$ signatures ranged from -0.25‰ to 3.66‰ suggesting that organic matter found in this study is derived from environments with a variety of salinity regimes (Boutton, 1991). Organic matter enriched

in ^{13}C ($\delta^{13}C \approx$ -22‰ to -20‰) indicates that it was most likely produced in a marine or high salinity environment while organic matter that is depleted in ^{13}C ($\delta^{13}C \approx$ -31‰ to -25‰) suggests that the organic matter was produced in a freshwater or low salinity environment (Boutton, 1991). Organic matter with $\delta^{15}N$ signatures close to 0‰ indicates a nitrogen-fixing source, such as mangroves (Nadelhoffer & Fry, 1994).

Samples analyzed from the riverine facies and from the organic-rich, shell-poor subtidal sand and mud facies yielded $\delta^{13}C$ signatures consistent with a more freshwater-influenced environment. These results are consistent with the environmental interpretation based on faunal and sedimentologic evidence.

Carbon isotope signatures for the vermetiform gastropod-dominated reef facies and the shell-rich subtidal sand and mud facies are consistent with marine signatures. However, carbonates from the shell-rich fractions of these sediments may be artificially enriching the carbon isotope signature.

Late Holocene History: Correlation.

The lithostratigraphic relationships of the cores in each transect are represented in a series of fence diagrams: the Hendry / Mullock Creek fence (Figure 28), the Estero River fence (Figure 29), the inshore Imperial River fence (Figure 30), and the offshore Imperial River fence (Figure 31). All available radiocarbon dates obtained for cores included within the transects are reported as calibrated ages, unless otherwise specified, alongside the stratigraphic columns.

The transects from Hendry / Mullock Creek and Estero River are clearly oriented along an estuarine axis. Consequently, these fence diagrams are best suited to document the spatial and temporal progression of the marine transgression. The height, relative to mean sea level, of the basal transgressive peat increases in the shoreward direction (note the stepping up in height of the green-colored peat facies in Figure 28). Three radiocarbon dates exist for the mangrove peats for the Hendry fence, and they get progressively younger in the upstream direction (5300 ybp, 3120 ybp, and 2280 ybp; Figure 28). The same 'stepping up' pattern is apparent in the upstream direction on the Estero River fence (Figure 29). The basal transgressive peat occurs in cores 0307-14,

0307-13, and 0102-1. (The mangrove peats at the tops of cores 9911-3 and 9911-4 are regressive peats and are part of the mosaic progradation.)

The relative heights and ages of the basal transgressive peats can be used to estimate sea level rise rates. This is best exemplified on the Hendry fence (Figure 28). The difference in height of the peat tops divided by the difference in absolute age of the two peats provides an estimate of sea level rise rate for this interval of time. When calculated for the 5300 and 3120 ybp peats, a sea level rise rate of 8 cm / 100 years is obtained for this time interval. Repeating the same process for the 3120 and 2280 ybp peats yields approximately the same sea level rise rate. This value is consistent with phase 2 of the Wanless et al. (1994) sea level curve (Figure 1). However, our measured rate is somewhat low for the older, phase 1 segment. The more refined South Florida sea level curve produced by Gelsanliter and Wanless (1995; Figure 2) has a number of accelerated and decelerated phases. If the curve is smoothed for the interval between 4500 ybp and the present, the slope would approximate a value of 8 cm / 100 yrs. Consequently, the rate obtained for the Hendry Creek fence is viewed as consistent with previous findings. It should be noted, however, that the stratigraphic columns within all the fences have not been decompacted. Consequently, the height of the basal marine peats would differ somewhat if the columns could be differentially decompacted. This shortfall adds another element of error to the sea level rise rate estimation.

The relative distribution of marine, high brackish, and low brackish water facies are consistent with the transgressive – regressive cycle interpretation. Marine facies become more common within stratigraphic columns in the downstream direction, and low brackish water facies are more common in the upstream direction. Again, this is very evident on the Hendry Creek and Estero River fences. Marine facies are not likely to transgress too far upstream in a watershed; similarly low brackish water facies are not likely to regress too far downstream.

The Imperial River offshore fence in general exhibits the stepping up of the basal transgressive peat (Figure 31). The peats are absent from the 2 downstream-most cores (cores 0306-6 and 0306-4); these cores were not deep enough to penetrate the basal transgression. Upstream from here the mangrove peat is higher in core 0306-8; the peat

is missing core 0307-9, but the shell bed demarking the unconformity above the supratidal sands, the position formally occupied by the mangrove peat, is higher as well. The upstream-most core (0406-9) shows the peat in a slightly depressed position. Compaction, however, may explain the misplaced height.

The maximal transgressive marine facies are found in all sections of the Imperial offshore fence, and their positions increase in height in the upstream direction (Figure 31). Because this transect is positioned west of Estero Bay's medial longitudinal axis, marine influence is expected throughout the fence. The fact that marine facies become progressively younger in the north to south direction, based on relative stratigraphic heights, suggests that the marine transgression did not proceed in a linear, west to east direction in the earliest late Holocene. It is likely, therefore, that the coast contained an eastward indentation in what is now the southern position of Estero Bay. (The same conclusion can be drawn for the northern end of Estero Bay. The basal marine peat is time transgressive toward the north in the Hendry fence, suggesting that the coast had an eastward indentation in what is now the northern end of Estero Bay.)

Patterns of transgression are not readily obvious in the Imperial inshore fence (Figure 30). It may be that these localities are too proximal to exhibit consistent evidence of transgression. This fence, however, does exhibit interesting regression patterns. Progradational facies are common throughout this fence, and the regressive package becomes thicker in the upstream direction. The progradation is represented simply by the brackish, intertidal oyster reef facies (sitting above the more marine, shell-rich subtidal facies) in the two downstream-most cores (0306-6 and 0307-15). Riverine, oyster reef, mangrove peat, and organic-rich subtidal facies make up the regressive package in the 3 most upstream cores. This pattern of upstream thickening and increasing facies complexity is consistent with a more linear, rather than mosaic, style progradation of this southern end of Estero Bay (see further discussion of river influence in the Imperial River transect below).

Influence of Fluvial Sedimentation in the Imperial River.

The cores from the Imperial River transects, particularly those from the inshore transect, exhibit appreciable influence by fluvial sedimentation. The riverine facies caps the 3 upstream-most cores from the inshore fence (0306-7 [Figure 32], 0307-12 [Figure 33], and 0307-11) and 2 of the cores from the offshore fence (0306-8 and 0406-9). Interestingly, fluvial sediment is not common near the mouths of the other two watersheds, Hendry Creek and Estero River. A calibrated radiocarbon date of 460 ybp was obtained immediately below the base of the riverine facies in core 0306-7, in what is clearly a more marine subtidal facies (Figure 32), suggesting that the Imperial River system dates to at least this time frame. Core 0307-12 illustrates other facies that are commonly associated with river channels, point bars, and deltaic environments (Figure 33). Facies C in this core is the progradational mangrove peat. Presumably the ancestral Imperial River migrated through the mangrove forest to create younger facies B and A. Oyster reefs are commonly associated with riverine tidal flats and bars. The brackish, intertidal oyster reef facies found in position B is dominated by sands, rather than muds, indicating that this may have been a reef developed on river-derived bed load sediments. Facies A represents the present-day tidally influenced river channel that presumably interrupted reef development.

The Imperial River's drainage was modified in recent history by repositioning the mouth at the junction between Fishtrap and Big Hickory Bay for navigational purposes (the "recent mouth" noted on Figure 34). The ancestral mouth was located further east in the southeastern corner of Big Hickory Bay. Presumably this repositioning has shifted the river's depocenter toward the west and away from Big Hickory Bay's southeastern corner. The fence diagrams demonstrate this. The inshore transect, positioned to traverse drainage to the ancestral mouth, exhibits thicker packages of fluvial sediment. Alternatively, fluvial sediments are poorly developed in the offshore transect, positioned through the recent mouth, suggesting a more recent and shorter history of fluvial deposition here.

Role of Reef Development.

Coastal progradation of Southwest Florida is clearly controlled principally by the development of oyster reefs. In order to better understand this role, the history of reef development in the Horseshoe Keys region of north-central Estero Bay was studied.

Figure 35 shows a fence diagram relating the 3 cores taken from the reef crest and reef flank in the Horseshoe Keys (see location in Figures 18 & 19). All 3 cores exhibit a reef faunal succession where the reef-building assemblage changes upsection to reflect greater influence of freshwater. A vermetiform gastropod-dominated assemblage gradually transitions to a mix of vermetiform gastropods and oysters, ultimately changing to an oyster-only reef-building assemblage. The species of vermetid and turritellid gastropods that compose the reef are less tolerant of brackish water than *Crassostrea virginica*. In addition, a commensurate sedimentologic change through these reef facies occurs that suggests the environment becomes less energetic and more protected upsection.

The timing of onset of vermetiform gastropod reef development is 2350 ybp, for core 0209-18, and 2690 ybp, for core 0209-19. Reef initiation was, therefore, time transgressive throughout the Horseshoe Keys; reef development initiated in one or more localized areas and then spread laterally through time. Two calibrated radiocarbon dates were obtained for the transition to oyster-only reef development in the same 2 cores. Both date at 470 ybp. The isochronous timing is curious and suggests that some synchronous environmental event caused the faunal transition. Alternatively, the common dates may be coincidental.

The sequence of reef facies appears to represent an autogenic succession, whereby the presence of the vermetiform gastropod-dominated assemblage physically changes its environment and ultimately predisposes the habitat for oysters. Vermetiform gastropods may have generated a reef structure along a more exposed coastline that eventually created a more protected backreef environment. That barrier could have also effectively increased the retention time of freshwater, thereby initiating an estuarine environment that was later more conducive to oyster reef formation. This hypothesis is intriguing but requires further testing. At present, it is also unclear how old the barrier

island system is. If the barrier islands predated the vermetiform gastropod reefs, the freshwater entrapment and the resulting estuarine conditions of Estero Bay would have already existed. The high-energy sedimentologic features associated with the vermetiform gastropod-dominated facies and the fact that modern relict vermetiform reefs exist along the exposed coast of the Ten Thousand Islands are compelling arguments favoring the lack of a protective barrier at 2690 ybp.

The thicknesses of the reef facies and their associated radiocarbon dates can be used to estimate reef accretion rates (ignoring the complicating factor of compaction). Given these data, vermetiform gastropods accreted at rates around 12 cm / 100 yrs while oysters accreted more rapidly at about 18 cm / 100 yrs. These rates are greater than the rate of sea level rise that existed between 3200 – 200 ybp, but less than the sea level rise rates that existed prior to 3200 ybp (Figure 1). The difference in accretion rates between vermetiform gastropods and oysters also implies that vermetiform gastropods should be more sensitive to sea level rise and therefore be less able to sustain reef development during times of rise acceleration.

An older, failed attempt at oyster reef formation dating between 4500 – 5500 ybp existed elsewhere in Southwest Florida (i.e., Ten Thousand Islands; Savarese, unpublished data), and there is some indication that this earlier phase of reef formation existed in the Estero Bay region (see core 0307-9), though we lack dates to constrain the timing. If the sea level rise rates compiled by Wanless et al. (1994) or by Gelsanliter and Wanless (1995) are correct, the high sea level rise rate occurring at this time would have been incompatible with the rate of reef sedimentation. This may explain why this early phase of reef formation was not long in duration. Figure 36 plots these two intervals of reef development on top of the Wanless sea level curve.

These late Holocene patterns in reef development indicate that if the recent acceleration of sea level rise, documented since the beginning of industrialization, persists over decadal and centennial time scales, reef development will again become incompatible with sea level.

Stability of the Inner Bay Margin.

It has been hypothesized that sea level rise inundated the inner bay margin around 3200 ybp and that the margin has remained static since that time despite the continuous rise in sea level. This hypothesis was tested for Estero Bay by interpreting the late Holocene history of cores taken just inboard of the inner bay margin in all 3 watersheds (cores 0312-31, 0405-5, and 0405-6).

The stratigraphic section for all 3 cores have relatively thick packages of mangrove peat sitting directly on top of supratidal / subaerial sands. There is no intervening record of marine or estuarine deposits between these two facies. A calibrated radiocarbon age is available at the base of the peat in core 0312-31 (from the inner bay margin near Hendry Creek; Figure 37) and dates at 2320 ybp. This indicates that the mangrove forest fringe at the inner bay margin was in place at least this long.

Cores taken just seaward of the inner bay margin (cores 0205-6 in Hendry [Appendix A] and 0307-15 in Imperial [Figure 38]) provide evidence for recent set-back of the margin. Risi and others have argued that recent sea level rise acceleration should eventually cause a transgression of the inner bay margin, triggered by storm-caused erosion (Risi et al., 1995). Core 0205-6 was taken within 5 meters of the mangrove fringe; a thin veneer of estuarine subtidal sediments sits directly on top of a mangrove peat. Core 0307-15 was also taken within 5 meters of the mangrove fringe. In this core, a 75 cm package of subtidal and intertidal sediments rests on top of a mangrove peat. The top of the peat dates at 2595 ybp and is overlain by a storm-generated shell bed, suggesting that storm erosion cut down through over 2500 years of mangrove deposition. Both these cores support the hypothesis of recent, storm-triggered transgression of the inner bay margin.

Back-barrier Island History.

Of the 2 cores taken behind the barrier islands (core 0408-11, behind Ft. Myers Beach, and 0408-10, in western Fishtrap Bay), only the core behind Ft. Myers provided clues about the origin of the barrier islands (Figure 39). Unfortunately, no radiocarbon

dates have been acquired for either of these cores, so no geochronologic information is available at present.

The basal transgressive peat in core 0408-11 (facies E) is not much deeper than where it is positioned within cores taken from the center of Estero Bay. The facies immediately above the peat (D) contains a shell gravel with marine fossils. This environment may represent a high-energy inner shelf environment or perhaps a beach. Regardless, the sediments were clearly deposited in a high energy, fully marine environment associated with an open coast. Facies C may represent the barrier island setting. The facies is dominated by very fine sand with sparse marine shells and organics. This is then overlain by facies B, a mangrove peat that is interpreted as a back-barrier mangrove forest. The shell-rich subtidal facies (A) rests at the top of the package.

If this interpretation is correct, this core documents the first appearance of the barrier island and records the precursor open coastal setting prior to island formation. Facies D would be a time equivalent unit to the vermetiform gastropod-dominated reef facies from the interior of Estero Bay. Interestingly, facies D does contain fragments of vermetiform turritellids and oysters. This back-barrier environment holds great promise for deciphering the history of barrier island formation.

Amino Acid Racemization.

At the onset of the study, it was hoped that amino acid racemization within oyster shells could be used as a geochronometer in place of radiocarbon dating. Unfortunately, the limited work we undertook to refine the dating system was not enough to generate a useable technique at this time.

The calibration equation obtained relating the D/L glutamic acid ratio to radiocarbon age is displayed in Figure 40. The best-fit linear regression equation has a relatively poor R^2 value of 0.78. Subsequent to the calibration, 25 oysters were subjected to racemization analysis to acquire dates of key environmental events through the late Holocene. To illustrate the problem with the application of the calibration equation to obtain absolute ages, the amino acid racemization dates for 7 oysters from one core

(0307-9) were plotted against stratigraphic height (Figure 41). If all dates were true (i.e., they truly reflected the time at which the oyster was buried), then there should be no stratigraphic disordering among the dates – the dates would get progressively older as you went deeper into the section. Stratigraphic disordering is evident in Figure 41. The most parsimonious interpretation is that at least 2 oysters are out of sequence, the one dating at 2983 and the other at 4411 ybp. These could be oysters that were reworked; physical processes exhumed the oysters and redeposited them at a more recent date (i.e., these oysters are older than the time at which they were finally buried). The problem with this explanation, however, is that these oysters have relatively pristine taphonomic grades (grades of 1 or 2); the quality of their preservation indicates they have not experienced significant reworking. The anomalously young date of 2879 ybp at the base of the section is also problematic and indicates the situation cannot be explained by reworking. We have radiocarbon dates ranging from 4000 – 5500 ybp at these depths in other cores. Stratigraphic disordering due to reworking cannot transport a young oyster back in time.

Ultimately this analysis indicates the calibration is erroneous and further study is needed. Because our oysters are intertidal, they experience radically different temperatures when exposed to air and water. Racemization rates are temperature sensitive. This may be differentially affecting reaction rates. Different microlayers of the oyster shell may be more susceptible to temperature effects than others. We hope to further investigate racemization processes in discrete layers of the oyster shell.

Recent Sedimentation Rates.

Data are presented and discussed on a core-by-core basis for cores 22 and 1 from southern Estero Bay and then core 16 from the northern bay: The data include the following:

1. Excess ^{210}Pb, ^{137}Cs and resulting sediment ages and sediment accumulation rates.
2. Total aluminum (Al).
3. Total organic carbon TOC).

4. Calcium carbonate ($CaCO_3$).

The primary focus of this part of the study is on recent (past 100 years) sediment accumulation. The supplemental data for total Al, TOC and $CaCO_3$, coupled with sediment ages, provide information about any recent changes in sediment composition.

Sediment Core 22 was collected from a small pocket in the southern-most portion of Estero Bay (Figure 42). The water depth was about 1.5 m and the core collected for recent geochronology was 18 cm long. The water content of the sediment decreased from 77% water (by weight) in the surface layer to 28% at the base of the core (Figure 43).

The activity profile for ^{137}Cs shows a decrease from the surface to 10 cm. Below 13 cm, the activity is near the detection limit. The small amounts of ^{137}Cs in the lower portion of the core may have been mixed down or filtered down with small amounts of fine-grained clay. Using depths of 10.5 to 13.5 cm for the 1950 marker of no detectable ^{137}Cs, the sedimentation rate based on ^{137}Cs is 0.20 to 0.25 cm/yr. This range is in reasonably good agreement with the rate of 0.20 cm/yr from the excess ^{210}Pb data.

The vertical profile for excess ^{210}Pb also was plotted versus the cumulative dry mass of sediment (Figure 45 based on Eqs. 4 to 6). A good fit was observed ($r = 0.97$) and the calculated sediment accumulation rate is 0.16 $g/cm^2/yr$. The ages derived from this calculation of sediment accumulation rate based on the CIC model are used as the y-axis for the vertical profile for ^{137}Cs (Figure 45). With this independent approach, the depth for 1950 is about 12 cm and thus a sedimentation rate in cm/yr of 0.23 cm/yr is derived. This value is in good agreement with the results discussed above. The actual ages that correspond with each layer are given in the appendix within the separate report authored by Trefry et al.

The data for excess ^{210}Pb and cumulative dry mass of sediment also were used to obtained sediment ages using the CRS model (Eqs. 7 to 9). A comparison between the CIC and CRS models based on excess ^{210}Pb (Figure 46) shows good agreement back to about 1960. At earlier dates, the CRS model predicts an older age than the CIC model. The CIC model shows better agreement with results for ^{137}Cs. The CRS model is subject to error under conditions of non-steady state sedimentary processes such as slumping and

deposition or erosion of sediment layers during storm events. This trend is similar to that observed by Kang et al. (2000) in Florida Bay.

Thus, for the purposes of this study, sedimentation rates of 0.20 to 0.25 cm/yr seem most reasonable for core 22. This range will be used in the subsequent discussion of sediment composition. The exact ages for a given sediment layer will be those derived from the CIC model.

The mean values and ranges for water content, excess ^{210}Pb, ^{137}Cs, ^{226}Ra, total Al, TOC, and $CaCO_3$ are given in Table 4. Vertical profiles for Al, TOC, and $CaCO_3$ are plotted in Figure 47. The activity of excess ^{210}Pb in the surface layer of core 22 of 8.2 dpm/g is consistent with the value of 6.1 dpm/g obtained for a thicker layer of surface sediment collected as a screening tool (Figure 42). This level of excess ^{210}Pb is consistent with a lower rate of sediment accumulation because excess ^{210}Pb has had more time to accumulate in the particles deposited at this site.

Concentrations of total Al and the activities for ^{226}Ra are highest in the top layers of the core and lowest at the base of the core. A direct relationship between Al and ^{226}Ra was observed for all sediment samples collected from Estero Bay (Figure 48). Despite variations in the activities of ^{226}Ra, they correlate with Al concentrations in sediments from all three cores (Figure 48). The activity of ^{226}Ra at the y-intercept (~0.65 dpm g^{-1}) is similar to values for limestone (0.6-0.9 dpm g^{-1}; Eisenbud, 1973). Limestone has levels of Al that are <0.1%. The good relationship ($r = 0.84$, $n = 42$) between ^{226}Ra and Al suggests that ^{226}Ra is mostly incorporated with aluminosilicate minerals and that the ^{226}Ra in sediment from this study is mostly detrital in origin. Downcore variations in activities of ^{226}Ra in core 22 are consistent with the trend for Al (Figure 47).

Concentrations of Al, $CaCO_3$, and TOC are about 3, 3, and 7 times higher, respectively, in the surface layer of core 22 than at the base of the core (Table 4 and Figure 47). The onset of increasing concentrations of these three parameters is in the period after 1950 (Figure 47) when the development in the area began a period of increased growth. Such large increases in levels of TOC have been observed in recent sediments from other areas in Florida (Trefry et al., 1992). These organic-rich sediments have a high oxygen demand, are generally anoxic and lead to low-oxygen conditions in the water column, especially in late summer.

Sediment Core 1 was collected from a more open area in southern Estero Bay (Figure 42). The water depth was about 1.5 m and the core collected for recent geochronology was ~30 cm long.

In contrast with core 22, results for core 1 show little or no useful radionuclide data (Figure 49). Activities of excess ^{210}Pb were highly variable throughout the core (Figure 49). Likewise, activities for ^{137}Cs were variable throughout the core with highest levels at about 22 cm. Thus, no reliable sedimentation rate could be determined. The distribution of radionuclides suggests that the sediments at this site have been subjected to significant mixing and loss or gain of sediment.

Concentrations of Al, $CaCO_3$, and TOC are relatively uniform throughout the core with a coefficient of variance ([mean/standard deviation] x 100%) of about 25% for each of the three parameters (Table 5 and Figure 50). Furthermore, concentrations of all three parameters are low and similar to levels found at the base of core 22. The core is predominantly composed of quartz sand (≥70%).

Sediment core 16 was collected from the northern portion of Estero Bay (Figure 51). The water depth was about 1.5 m and the core collected for recent geochronology was 38 cm long. The water content of the sediment decreased from 76% water (by weight) in the surface layer to 34% near the base of the core (Table 6 and Figure 52).

The vertical profile for the activities of excess ^{210}Pb for core 16 has characteristics of profiles from both cores 22 and 1. There is some scatter in the activities of excess ^{210}Pb; however, within that scatter, a logarithmic decrease has been resolved by omitting data points for which both the excess ^{210}Pb and ^{137}Cs activities were anomalously low (Figure 53). Kang et al. (2000) and Kang and Trefry (2003) used this approach for sediment cores from Florida Bay when sediment was believed to have been winnowed away or when older sediment (with low activities) was deposited, generally during storm events. After removing the anomalous values, a line with a correlation coefficient of 0.98 was obtained (Figure 53) and the calculated sediment accumulation rate is 0.34 cm/yr [S = (-0.0311/yr)/(-0.091 cm) = 0.34 cm/yr].

The activity profile for ^{137}Cs shows considerable variation in the top 10 cm with a decrease to detection limits from 10-17.5 cm. Using a depth of 17.5 cm for the 1950 marker of no detectable ^{137}Cs, the sedimentation rate based on ^{137}Cs is 0.33 cm/yr. This range is in remarkably good agreement with the rate calculated with the excess ^{210}Pb data.

The vertical profile for excess ^{210}Pb also was plotted versus the cumulative dry mass of sediment (Figure 54 based on Eqs. 4 to 6). A good fit was observed ($r = 0.99$) and the calculated sediment accumulation rate is 0.25 $g/cm^2/yr$. The ages derived from this calculation of sediment accumulation rate based on the CIC model are used as the y-axis for the vertical profile for ^{137}Cs (Figure 54). With this independent approach, the depth for 1950 is about 19.5 cm and thus a sedimentation rate of 0.37 cm/yr is derived. This value is in good agreement with the results discussed above. The actual ages that correspond with each layer are given in the appendix within the separate report authored by Trefry et al. The CRS model did not provide ages that matched the ^{137}Cs data as well the CIC model.

Thus, for the purposes of this study, sedimentation rates of 0.33 to 0.37 cm/yr seem most representative for core 16. This range will be used in the subsequent discussion of sediment composition. The exact ages for a given sediment layer will be those derived from the CIC model.

The mean values and ranges for water content, excess ^{210}Pb, ^{137}Cs, ^{226}Ra, total Al, TOC, and $CaCO_3$ are given in Table 6. Vertical profiles for Al, TOC, and $CaCO_3$ are plotted in Figure 55. Core 16 was collected adjacent to a large oyster reef and the carbonate content was high and relatively uniform (CV = 11%) throughout the core (Figure 55). Concentrations of TOC and Al in the top 8 cm of the core (since 1980) are about 30% and 40%, respectively, greater than in the lower portion of the core (pre-1980). Levels of TOC are 1.8± 0.3% in all sediment deposited prior to 1980 and dating back to the early 1900s (Figure 55). However, the relative degree of increase in levels of TOC in core 16 is much lower than in core 22.

Summary. -- In the southern bay (core 22), the calculated sedimentation rate was 0.20-0.25 cm/yr and the sediment mass accumulation rate was 0.16 $g/cm^2/yr$ over the past 70-

90 years. Three- and seven-fold increases in concentrations of Al and TOC, respectively, were observed since 1950 in core 22 from southern Estero Bay. In the northern bay (core 16), the calculated sedimentation rate was about 0.35 cm/yr and the sediment mass accumulation rate was 0.25 $g/cm^2/yr$. Concentrations of TOC and Al have increased by 30% and 40%, respectively, since about 1980 in the core from northern Estero Bay.

References Cited

Abbott, R. T. 1967. American Seashells. D. Van Nostrand Company, Inc., Princeton, New Jersey. 541 p.

Andrews, J. 1977. Shells and Shores of Texas. University of Texas Press, Austin, Texas. 365 p.

Appleby, P.G. and Oldfield, F. 1978. The calculation of lead-210 date assuming a constant rate of supply of unsupported ^{210}Pb to the sediment. Catena 5: 1-8.

Boggs, S. Jr. 2001. Principles of Sedimentology and Stratigraphy. Prentice Hall, New Jersey, 726 p.

Boutton, T.W. 1991. Stable carbon isotope ratios of natural materials: II. Atmospheric, terrestrial, marine, and freshwater environments, p. 173-185. *In* D.C. Coleman and B. Fry [eds], Carbon isotope techniques. Academic Press, San Diego.

Brandt, D. S. 1989. Taphonomic grades as a classification for fossiliferous assemblages and implications for paleoecology. Palaios 4:303-309.

Brewster-Wingard, G. L. and Ishman, S. E. 1999. Historical trends in salinity and substrate in central Florida Bay: a paleoecological reconstruction using modern analogue data. Estuaries 22(2B):369-383.

Cahoon, D. R. and Lynch, J. C. 1997. Vertical accretion and shallow subsidence in a mangrove forest of southwestern Florida, USA. Mangrove and Salt Marshes 1:173-186.

Camp, D. K., Lyons, W. G., and Perkins, T. H. 1998. Checklists of Selected Shallow-water Marine Invertebrates of Florida. Florida Marine Research Institute Technical Report TR-3, 239 p.

Cloern, J.E., Canuel, E.A., and Harris, D. 2002. Stable carbon and nitrogen isotope composition of aquatic and terrestrial plants of the San Francisco Bay estuarine system. Limnology and Oceanography 47(3): 713-729.

Ellison, J. C. and Stoddart, D. R. 1991. Mangrove ecosystem collapse during predicted sea-level rise: Holocene analogues and implications. Journal of Coastal Research 7: 151-165.

Flessa, K. W., Cutler, A. H., and Meldahl, K. H. 1993. Time and taphonomy: quantitative estimates of time-averaging and stratigraphic disorder in a shallow marine habitat. Paleobiology 19(2):266-286.

Gelsanliter, S. and Wanless, H. R. 1995. High-frequency sea-level oscillations in the late Holocene of south Florida: a dominating control on facies initiation and dynamics. 1st SEPM Congress on Sedimentary Geology, Congress Program and Abstracts, vol. 1, St. Petersburg Beach, FL, p. 58.

Goodfriend, G. A. 1989. Complementary use of amino acid epimerization and radiocarbon analysis for dating of mixed age assemblages. American Journal of Science 3:1041-1047.

Gundersen, R. W. 1998. The Seashells of Sanibel and Captiva Islands. Bailey-Matthews Shell Museum, Sanibel, Florida. 30 p.

Hermanson, M.H. 1990. ^{210}Pb and ^{137}Cs chronology of sediments from small, shallow Arctic lakes. Geochimica et Cosmochimica Acta 54: 1443-1451.

Hopkins, S. H., 1956, Notes on boring sponges in Gulf Coast estuaries and their relation to salinity: The Bulletin of Maritime Science, v. 6, p. 44-58.

Hopkins, S. H., 1962, Distribution of species of Cliona (boring sponge) on the eastern shore of Virginia in relation to salinity: Chesapeake Science, v. 3, p. 121-124.

Intergovernmental Panel on Climate Change (IPCC). 1996. Climate Change 1995: The Science of Climate Change. Cambridge University Press, Cambridge. 572 p.

Kang, W.-J., Trefry, J. H., Nelsen, T. A., and Wanless, H. R. 2000. Direct atmospheric inputs versus runoff fluxes of mercury to the lower Everglades and Florida Bay. Enviromental Science and Technology 34:4058–4063.

Kang, W-J. and Trefry, J.H. 2003. Retrospective analysis of the impacts of major hurricanes on sediments in the lower Everglades and Florida Bay. Environmental Geology 44:771-780.

Kaufman, D. S. and Manley, W. F. 1998. A new procedure for determination DL amino acid ratios in fossils using reserve phase liquid chromatography. Quaternary Science Reviews 17:987-1000.

Koide M., Bruland, K.W. and Goldberg, E.D. 1973. $^{228}Th/^{232}Th$ and ^{210}Pb geochronologies in marine and lake sediments. Geochimica et Cosmochimica Acta 37: 1171-1187.

Krishnaswami, S., Lal, D., Martin, J.M. and Meybeck, M. 1971. Geochronology of lake sediments. Earth &Planetary Science Letters 11: 407-414.

Lindland, E. 2002. Time accumulation on an oyster reef: implications for the monitoring of environmental change. 15th Annual Keck Geology Consortium Research Symposium volume, p. 73-76.

Lindland, E., Savarese, M., and Goodfriend, G. A. 2001. Time of accumulation on an oyster reef: implications for the monitoring of environmental change. 16th Biennial Conference of the Estuarine Research Federation. Abstract volume, p. 80.

Maul, G. A., and Martin, D. M.. 1993. Sea level rise at Key West, Florida, 1846-1992: America's longest instrument record? Geophysical Research Letters 20:1955-1958.

Nadelhoffer, K.J. and Fry, B. 1994. Nitrogen isotope studies in forest ecosystems, p. 22-44. In K. Lajtha and R.H. Michener [eds]. Stable isotopes in ecology and environmental science. Blackwell Scientific Publications, Cambridge.

Obley, S. P. 2002. The influence of sea level rise on the history of estuarine environments in Southwest Florida. 15th Annual Keck Geology Consortium Research Symposium volume, p. 85-88.

Obley, S. P., Savarese, M., and Tedesco, L. P. 2001. The influence of sea level rise on the history of estuarine environments in Southwest Florida. . 16th Biennial Conference of the Estuarine Research Federation. Abstract volume, p. 102.

Parkinson, R. W. 1989. Decelerating Holocene sea-level rise and its influence on Southwest Florida coastal evolution: a transgressive/regressive stratigraphy. Journal of Sedimentary Petrology 59(6):960-972.

Risi, J. A., Wanless, H. R., Tedesco, L. P., and Gelsanliter, S., 1995, Catastrophic sedimentation from Hurricane Andrew along the southwest Florida coast: Journal of Coastal Research 21: 83-102.

Robbins, J.A. and Edgington, D.N. 1975. Determination of recent sedimentation rates in Lake Michigan using ^{210}Pb and ^{137}Cs. Geochimica et Cosmochimica Acta 39: 285-304.

Savarese, M. and Oches, R. 2004. Dating fossil oysters using amino acids. South Florida Water Management District Technical Report, 16 p.

Savarese, M., Volety, A., and Tolley, G. 2003. Influence of watershed alteration on oyster health and oyster-reef habitat: management implications for the Faka-Union and Estero Bays. South Florida Water Management District, Technical Report, 49 p. + 35 figures.

Savarese, M. and Wingard, L. 2004. Molluscs as environmental indicators of salinity change in southern Florida's estuaries. South Florida Water Management Technical Report, 100 p.

Schink, J.J., Stockwell, J.H. and Ellis, R.A. 1978. An improved device for gasometric determination of carbonate in sediment. Journal of Sedimentary Petrology 48: 651-653.

Shier, D. E., 1969, Vermetid reefs and coastal development in the Ten Thousand Islands, Southwest Florida: Geological Society of America Bulletin, v. 80, p. 485-508.

Snedaker, S. C. 1993. Impact on mangroves. Pp. 282-305. In: Maul, G. (ed.). Climatic Change in the Intra-Americas Seas, Edward Arnold, London.

South Florida Water Management District (SFWMD) Big Cypress Basin and U.S. Department of Agriculture Natural Resources Conservation Service. 2001. Southern Golden Gate Estates watershed planning assistance cooperative study. Final Report.

Tedesco, L. P., Wanless, H. R., Scusa, L. A., Risi, J. A., and Gelsanliter, S., 1995, Impact of Hurricane Andrew on south Florida's sandy coastlines: Journal of Coastal Research 21: 59-82.

Tolley, G., Volety, A., and Savarese, M. 2003. Shellfish research and adaptive resource management in Southwest Florida: oysters as sentinels of ecosystem health. World Aquaculture 34(4):64-66.

Trefry, J. H., and Metz, S. 1984. Selective leaching of trace metals from sediments as a function of pH. Analytical Chemistry 56:745-749.

Trefry, J.H., Chen, N-C., Trocine, R.P. and Metz, S. 1992. Impingement of organic-rich, contaminated sediments on Manatee Pocket. Florida Scientist 55:160-171.

Wanless, H. R. and Parkinson, R. W. 1989. Late Holocene sea level history of Southern Florida: control on coastal stability. Proceedings of the Eighth Symposium on Coastal Sedimentology, Coastal Sediment Mobility, p. 197-214.

Wanless, H. R., Parkinson, R. W., and Tedesco, L. P. 1994. Sea level control on stability of Everglades Wetlands. Everglades, the Ecosystem and Its Restoration. St. Lucie Press, p. 199-222.

Warmke, G. L. and Abbott, R. T. 1962. Caribbean Seashells. Livingston Publishing Company, Narberth, Pennsylvania. 348 p.

Wingard, G. L., Stone, J. R., and Holmes, C. W. 2001. Molluscan faunal distribution in Florida Bay, past and present: an integration of down-core and modern data. Bulletins of American Paleontology 361: 199-231.

Wingard, G. L., Cronin, T. M., Dwyer, G. S., Ishman, S. E., Willard, D. A., Holmes, C. W., Bernhardt, C. E., Williams, C. P., Marot, M. E., Murray, J. B., Stamm, R. G., Murray, J. H., and Budet, C. 2003. Ecosystem history of southern and central Biscayne Bay: summary report on sediment core analysis. U.S. Geological Survey Open File Report 03-375.

Wingard, G. L. 2004. Geochemistry and geochronology of 2003 cores, calibration of modern ecosystem indicators and status of work. U.S. Geological Survey Special Report to the South Florida Water Management District Biscayne Bay Paleoecological Salinity Study.

Table 1. GPS coordinates of late Holocene cores taken in Estero Bay. All coordinates are in UTM, 17R relative to WGS84 (NAD83).

Core Number	Easting	Northing	Accuracy (ft)
9911-2	413137	2922878	
9911-1	414276	2923718	
9911-3	414745	2923920	
9911-4	415503	2924363	
0006-1	413990	2923587	
0006-2	413626	2923313	
0102-1	414431	2923820	
0102-2	415084	2924172	
0106-9	413178	2922854	
0106-10	414750	2923901	
0205-5	412927	2925579	9
0205-6	413078	2926681	9
0205-7	412902	2927496	12
0206-11	412403	2925105	12
0206-12	412923	2925551	9
0207-16	412754	2924507	6
0207-17	413196	2926216	9
0209-18	412768	2924521	7
0209-19	412829	2924466	7
0212-21	415628	2924209	8
0306-4	415902	2914956	6
0306-5	416015	2914714	8
0306-6	416159	2916124	8
0306-7	416411	2914314	10
0306-7A	416411	2914314	10
0306-8	416018	2914692	7
0307-9	415971	2913885	8
0307-10	416134	2913094	7
0307-11	416610	2913465	16
0307-12	416439	2913781	8
0307-13	414359	2923692	8
0307-14	413189	2922839	7
0307-15	416625	2915032	8
0308-17	415707	2913496	8
0308-18	415935	2915139	7
0308-19	413132	2927188	7
0308-20	412767	2924478	8
0309-21	414329	2918893	12
0310-22	414394	2918935	8
0310-23	414321	2918885	8
0310-24	414153	2918875	9
0312-31	412954	2926687	18
0402-4	416279	2914367	16
0405-5	416472	2916046	17

0405-6	414909	2923832	18
0406-7	416614	2913458	11
0406-8	416614	2913458	11
0406-9	416141	2913098	12
0408-10	415335	2913907	9
0408-11	410789	2922365	7

Table 2. Data quality objectives and criteria for high resolution geochronology.

Element or Sample Type Criteria	Minimum Frequency	Data Quality Objective/Acceptance
Initial Calibration	Prior to every batch of samples	3-5 point curve depending on the element and a blank.
	Standard Curve	correlation coefficient $r \geq 0.999$ for all analytes.
Continuing Calibration	Must end every analytical sequence.	% RSD<15% for all analytes
Certified and Standard Reference Materials	Two per batch of 20 samples	Values must be within 20% of accepted values.
Method Blank	Two per batch of 20 samples	No analytes to exceed 5x MDL
Matrix Spike and Spike Method Blank	Two per batch of 20 samples	% RSD 80-120%
Lab Duplicate	Two per 20 samples	RSD <25%

Table 3. Compiled results of grain size analyses from all late Holocene cores. Histograms and cumulative weight percent graphs from which these data were obtained are found in Appendix B.

Core #	Depth (cm)	Facies	Graphic Mean	Graphic Std Deviation	Wentworth Size Class	Sorting
0205-5	1--3	A	3.16	2.648	very fine sand	very poorly sorted
0205-5	21--25	B	3.20	3.173	very fine sand	very poorly sorted
0205-5	50--55	C	2.50	0.915	fine sand	moderately sorted
0205-5	81--83	D	2.50	0.839	fine sand	moderately sorted
0205-5	93--100	E	2.70	1.208	fine sand	poorly sorted
0205-5	155--160	F1	2.36	0.075	fine sand	very well sorted
0205-5	215--220	F2	2.50	0.603	fine sand	moderately well sorted
0205-6	1--5	A	2.73	0.613	fine sand	moderately well sorted
0205-6	30-35	B	2.40	0.698	fine sand	moderately well sorted
0205-6	55-60	C	2.50	0.603	fine sand	moderately well sorted
0205-6	70-75	D	2.46	0.643	fine sand	moderately well sorted
0205-6	105-110	E	2.40	0.698	fine sand	moderately well sorted
0205-6	155-160	E1	2.46	0.658	fine sand	moderately well sorted
0206-11	35-40	A	3.13	1.593	very fine sand	poorly sorted
0206-11	93-98	B	3.30	1.733	very fine sand	poorly sorted
0206-11	135&139-144	C	2.83	1.027	fine sand	poorly sorted
0206-11	170-175	D	2.67	1.092	fine sand	poorly sorted
0206-11	193-198	E	2.47	0.658	fine sand	moderately well sorted
0206-11	231-236	F	2.60	0.603	fine sand	moderately well sorted
0206-12	6--11	B	3.60	1.758	very fine sand	poorly sorted
0206-12	70--74	C	2.53	0.769	fine sand	moderately sorted
0206-12	81--84	D	2.40	0.779	fine sand	moderately sorted
0206-12	93--98	E	2.90	1.358	fine sand	poorly sorted
0206-12	152-157	F1	2.37	0.754	fine sand	moderately sorted
0206-12	195-198 & 212-217	F2	2.70	1.167	fine sand	poorly sorted
0207-17	29-34	A	3.87	1.778	very fine sand	poorly sorted
0207-17	63-68	B1	2.70	0.588	fine sand	moderately well sorted

0207-17	115-120	B2	2.70	0.588	fine sand	moderately well sorted
0207-17	155-160	C	2.70	0.618	fine sand	moderately well sorted
0207-17	175-180	D	2.70	0.588	fine sand	moderately well sorted
0207-17	207-212	E	2.57	0.563	fine sand	moderately well sorted
0207-17	234-237	F	2.47	0.643	fine sand	moderately well sorted
0207-17	248-251	G	4.07	2.558	coarse silt	very poorly sorted
0207-17	267-272	H	2.50	0.603	fine sand	moderately well sorted
0207-17	300-305	I	2.57	0.548	fine sand	moderately well sorted
0207-17	355-360	J	2.60	0.492	fine sand	well sorted
0209-18	17-25	A	3.93	3.757	very fine sand	very poorly sorted
0209-18	50-60	B1	7.13	3.730	fine silt	very poorly sorted
0209-18	150-160	B2	2.40	2.163	fine sand	very poorly sorted
0209-18	220-230	B3	2.80	0.618	fine sand	moderately well sorted
0209-18	247-253	C	2.83	0.673	fine sand	moderately well sorted
0209-18	270-275	D	2.66	1.627	fine sand	poorly sorted
0209-18	283-292	E	2.73	1.536	fine sand	poorly sorted
0209-18	322-327	F1	2.53	1.314	fine sand	poorly sorted
0209-18	357--362	F2	2.50	0.698	fine sand	moderately well sorted
0209-19	65--70	A	4.16	3.567	coarse silt	very poorly sorted
0209-19	125-130	B1	2.86	0.916	fine sand	moderately sorted
0209-19	185-190	B2	3.00	3.069	very fine sand	very poorly sorted
0209-19	245-250	B3	2.70	1.060	fine sand	poorly sorted
0209-19	285-290	C1	2.76	1.309	fine sand	poorly sorted
0209-19	315-320	C2	2.70	1.329	fine sand	poorly sorted
0209-19	365-370	E1	2.60	1.424	fine sand	poorly sorted
0209-19	395-400	E2	2.50	1.223	fine sand	poorly sorted
0306-4	43-48	A2	3.43	1.577	very fine sand	poorly sorted
0306-4	81-86	B2	3.10	0.698	very fine sand	moderately well sorted
0306-4	161-166	C	3.63	1.362	very fine sand	poorly sorted
0306-4	268-273	D	3.70	1.633	very fine sand	poorly sorted
0306-4	304-309	E	2.50	0.588	fine sand	moderately well sorted
0306-6	70-75	B1	3.27	1.432	very fine sand	poorly sorted

0306-6	253-258	B3	2.63	0.916	fine sand	moderately sorted
0306-6	375-378	D	2.63	0.689	fine sand	moderately well sorted
0306-7	13-18	A	2.37	0.452	fine sand	well sorted
0306-7	34-39	B	2.57	0.533	fine sand	moderately well sorted
0306-7	121-126	C2	2.80	1.183	fine sand	poorly sorted
0306-8	4--9	A	2.50	0.508	fine sand	moderately well sorted
0306-8	71-76	B2	3.57	1.482	very fine sand	poorly sorted
0306-8	108-113	C	3.70	1.562	very fine sand	poorly sorted
0306-8	214-219	D2	3.10	1.382	very fine sand	poorly sorted
0306-8	236-241	E	3.57	1.522	very fine sand	poorly sorted
0306-8	275-280	F	3.73	1.658	very fine sand	poorly sorted
0306-8	301-306	G2	3.50	1.633	very fine sand	poorly sorted
0307-9	29-34	B	3.43	1.848	very fine sand	poorly sorted
0307-9	83-88	C	4.37	1.944	coarse silt	poorly sorted
0307-9	146-151	E	4.03	1.914	coarse silt	poorly sorted
0307-9	225-230	F	3.20	1.042	very fine sand	poorly sorted
0307-9	264-269	G	3.87	1.689	very fine sand	poorly sorted
0307-9	360-365	H	3.00	0.573	very fine sand	moderately well sorted
0307-10	10--18	B	2.93	0.593	fine sand	moderately well sorted
0307-10	33-38	C	3.00	1.062	very fine sand	poorly sorted
0307-10	79-84	D2	4.17	1.728	coarse silt	poorly sorted
0307-10	153-158	E	4.03	1.668	coarse silt	poorly sorted
0307-10	175-180	F	4.30	1.879	coarse silt	poorly sorted
0307-10	208-213	G	4.50	2.135	coarse silt	very poorly sorted
0307-10	255-260	H	4.20	2.014	coarse silt	very poorly sorted
0307-11	5--10	A	2.87	0.533	fine sand	moderately well sorted
0307-11	36-41	B	2.93	0.578	fine sand	moderately well sorted
0307-11	135-140	C2	2.57	0.997	fine sand	moderately sorted
0307-11	227-233	D	4.17	1.794	coarse silt	poorly sorted
0307-12	16-21	B	2.90	0.508	fine sand	moderately well sorted
0307-12	89-94	C	3.00	0.492	very fine sand	well sorted
0307-12	147-152	E	4.13	1.814	coarse silt	poorly sorted

0307-12	220-225	F	3.00	0.588	very fine sand	moderately well sorted
0307-15	5--10	A	5.03	1.894	medium silt	poorly sorted
0307-15	51-56	B	3.03	0.905	very fine sand	moderately sorted
0307-15	94-99	C	3.43	1.329	very fine sand	poorly sorted
0307-15	138-143	D1	2.87	0.870	fine sand	moderately sorted
0307-15	164-169	D2	2.90	0.573	fine sand	moderately well sorted

Table 4. Means ± standard deviations and ranges for selected data from sediment core 22 from southern Estero Bay.

Core 22 Parameter	Mean ± Std. Dev.	Range
Water content (% by wt.)	51 ± 13	28 – 77
Excess ^{210}Pb (dpm/g)	3.7 ± 2.6	0.5 – 8.2
^{137}Cs (dpm/g)	0.09 ± 0.04	0.03 – 0.12
^{226}Ra (dpm/g)	1.7 ± 0.3	1.2 – 2.2
Total Al (%)	1.27 ± 0.40	0.54 – 1.83
Total Organic Carbon (%)	3.0 ± 1.4	0.8 – 5.6
$CaCO_3$ (%)	13.1 ± 3.4	6.4 – 18.1

Table 5. Means ± standard deviations and ranges for selected data from sediment core 1 from southern Estero Bay.

Core 1 Parameter	Mean ± Std. Dev.	Range
Excess ^{210}Pb (dpm/g)	1.7 ± 1.5	<0.03 – 4.0
^{137}Cs (dpm/g)	0.03 ± 0.01	0.01 – 0.07
^{226}Ra (dpm/g)	1.2 ± 0.2	1.0 – 1.6
Total Al (%)	0.78 ± 0.18	0.52 – 1.05
Total Organic Carbon (%)	0.51 ± 0.14	0.34– 0.72
$CaCO_3$ (%)	9.5 ± 2.5	6.6 – 17.0

Table 6. Means ± standard deviations and ranges for selected data from sediment core 16.

Parameter	Mean ± Std. Dev.	Range
Water content (%)	52 ± 11	34 – 76
Excess ^{210}Pb (dpm/g)	3.1 ± 1.5	0.5 – 5.8
^{137}Cs (dpm/g)	0.07 ± 0.04	0.01 – 0.16
^{226}Ra (dpm/g)	1.8 ± 0.4	1.2 – 2.4
Total Al (%)	1.60 ± 0.31	0.91 – 2.15
Total Organic Carbon (%)	2.0 ± 0.6	1.3 – 3.2
$CaCO_3$ (%)	31.0 ± 3.3	24.8 – 38.0

Figure Captions

Figure 1. Sea level curve for the late Holocene compiled for south Florida taken from Wanless et al. (1994). Three phases of sea level rise are highlighted: 1. from 5500-3200 ybp with a rate of 23 cm / 100 yrs; 2. from 3200-200 ybp with a rate of 4 cm / 100 yrs; and 3. from 200-present with a rate of 30-40 cm / 100 yrs.

Figure 2. A high-frequency sea-level oscillation curve for the late Holocene of south Florida; modified after Gelsanliter and Wanless (1995).

Figure 3. Satellite image of the Greater Everglades of south Florida. Two regions are highlighted: Ten Thousand Islands and Estero Bay. The former is the type region for the Ten Thousand Islands Geomorphology. Estero Bay is the study region for this project. It too exhibits the Ten Thousand Islands Geomorphology, but also has coastal barrier islands at the seaward margin.

Figure 4. Close-up satellite view of the Ten Thousand Islands in Southwest Florida exhibiting the Ten Thousand Islands Geomorphology. Characterisitic elements of the geomorphology include: inner bay margin, inner bay, inner bay islands, and outer bays and islands. Longshore transport is minimal here so barrier islands are absent.

Figure 5. The approximate position of the coastline in south Florida is depicted here assuming no sedimentation occurred and sea level rise proceeded at the rate measured during the late Holocene. This effectively would eliminate coastal progradation during the last 3200 years. Taken from Wanless et al. (1994).

Figure 6. Tide gauge data compiled for Key West from 1910-1990. Taken from Maul and Martin (1993). The smoothed curve represents the position of sea level for the same time interval and has a slope equal to approximately 30 cm / 100 yrs. This sea level rise rate is an order of magnitude higher than those measured for the preceding 3000 years.

Figure 7. Tide gauge data compiled for Fort Myers from 1966-1997. The smoothed curve yields a sea level rise rate of 12 cm / 100 yrs. When this analysis is completed and compiled for all localities peninsular coastal Florida, the rise rate ranges from 12 – 48 cm / 100 yrs.

Figure 8. Photograph of oyster reef exposed at low tide in the Horseshoe Keys region of north-central Estero Bay. The effects of progradation are shown: mangrove propagules and seedlings have rooted on the oyster reef.

Figure 9. Satellite image of Estero Bay showing 3 watersheds included in this study: 1. Hendry and Mullock Creek; 2. Estero River; and 3. Imperial River. The following geomorphologic features are noted: inner bay margin, inner bay islands, barrier islands, and flood tidal delta islands.

Figure 10. Location of late Holocene sediment cores taken in northern Estero Bay. Localities fall on 2 transects: the Hendry Creek transect, and the Estero River transect. Cores 0207-16, 0209-18, are 0209-19 from the Horseshoe Keys used in the study of oyster reef history.

Figure 11. Location of late Holocene sediment cores taken in southern Estero Bay. Localities fall on 2 transects within the Imperial River: an inshore transect that traverses the eastern margin of Estero Bay, and the offshore transect that traverses the western margin of Estero Bay. Cores taken in the northwest region (0309-21, 0310-22, 0310-23, and 0310-24) are located on an inactive tidal delta behind a closed tidal inlet (due to road construction). These cores were part of a student project; data are not included herein, but are available upon request.

Figure 12. Photograph of a hand core being taken.

Figure 13. Photograph of a vibracore being taken on a Horseshoe Keys' reef.

Figure 14. A split core showing some of the common facies. 1: Supratidal / subaerial sands. 2: Intertidal mangrove peat. 3: Vermetiform-dominated shallow subtidal reef. 4: Oyster-dominated intertidal brackish reef.

Figure 15. Sample grain size histogram (core 0206-11, facies C) for data derived from laser coulter counter. Grain size reported in units of phi. The complete set of histograms is included in Appendix B.

Figure 16. Cumulative percent weight frequency plot for same sediment sample plotted in Figure 15. The Folk graphical method was used to acquire a value for mean grain size and sorting. The complete set of plots is included in Appendix B.

Figure 17. Histogram of salinity occurrences of the living bivalve *Anomalocardia auberiana* derived from recent monitoring data in Florida and Biscayne Bays (by U.S. Geological Survey). This is a sample of one histogram; the complete set is available in the report by Savarese & Wingard (2004).

Figure 18. Satellite image of the Horseshoe Keys region in north-central Estero Bay. This is the region in which the oyster reef history study was conducted. Inset shown as close-up image in Figure 19.

Figure 19. Close-up image of reefs in northern Horseshoe Keys. Arrows denote the locations of the 3 cores.

Figure 20. Map showing location of sediment samples taken in northern Estero Bay for recent sedimentation rate determination. Location 16 had the best in-sediment radiogenetic activity and therefore was chosen for further study.

Figure 21. Similar image for southern Estero Bay showing the location of sediment samples for recent sedimentation rate determination. Location 22 had the best in-sediment radiogenetic activity and therefore was chosen for further study.

Figure 22. Photograph of a SCUBA diver taking one of the sedimentation rate cores.

Figure 23. Photograph of core sediment extraction for high-resolution geochronology work.

Figure 24. Photograph of reef-forming vermetiform gastropods (the turritellid *Vermicularia*) removed from a core traversing the vermetiform gastropod-dominated reef facies. Specimens were oriented in the core tube as displayed by the up arrow.

Figure 25. Stratigraphic column for core 0206-12 taken from the outer edge of the inner bay, Hendry Creek transect. Stratigraphy shows the younger transgressive – regressive cycle; facies interpretations are noted alongside the column and are color-coded (following the same scheme defined for the fence diagrams [see Figure 28]).

Figure 26. Stratigraphic column for core 0207-17 taken from the middle region of the inner bay, Hendry Creek transect. Stratigraphy shows the younger transgressive – regressive cycle; interpretations are noted alongside the column, and facies are color-coded (following the same scheme defined for the fence diagrams [see Figure 28]).

Figure 27. Stratigraphic column for core 0307-9 taken from the middle region of Fishtrap Bay, Imperial River transect. Stratigraphy shows the younger and older transgressive – regressive cycles; interpretations are noted alongside the column, and facies are color-coded (following the same scheme defined for the fence diagrams [see Figure 28]).

Figure 28. Fence diagram for the Hendry Creek transect. Cores are oriented, from left to right, downstream (south) to upstream (north). Positions and ages of the basal transgressive peats were used to calculate a sea level rise rate of 8 cm / 100 yrs. Facies are colored-coded as follows: tan = regolith; brown = supratidal / subaerial; dark green = freshwater peat; light green = intertidal, mangrove peat; dark blue = organic-rich, shell-poor subtidal sands and muds; purple = shell-rich subtidal sands and muds; light blue = intertidal, oyster reef; pink = subtidal vermetiform gastropod-dominated reef; magenta = subtidal oyster – vermetiform gastropod reef; red = intertidal mud or sand flat; yellow = riverine.

Figure 29. Fence diagram for the Estero River transect. Cores are oriented, from left to right, downstream (west) to upstream (east). Facies color-codes same as in Figure 28.

Figure 30. Fence diagram for the inshore transect of the Imperial River. Cores are oriented, from left to right, downstream (north) to upstream (south). Facies color-codes same as in Figure 28.

Figure 31. Fence diagram for the offshore transect of the Imperial River. Cores are oriented, from left to right, downstream (north) to upstream (south). Facies color-codes same as in Figure 28.

Figure 32. Stratigraphic column for core 0306-7 taken from the inner edge of Big Hickory Bay, near the old mouth of the Imperial River. Stratigraphy shows the riverine facies overlying subtidal estuarine sediments. Age of riverine onset dated at 460 ybp.

Figure 33. Stratigraphic column for core 0307-12 taken from of the old channel of the Imperial River. Stratigraphy shows the riverine facies in the context of the progradation sequence.

Figure 34. Satellite image of southern Estero Bay showing the position of the old and recent mouths of the Imperial River.

Figure 35. Fence diagram for the cores taken in the Horseshoe Keys through modern oyster reefs. Facies color-codes same as in Figure 28.

Figure 36. Sea level curve after Wanless et al. (1994) with timing of reef development, relative to the 2 transgressive – regressive cycles, plotted.

Figure 37. Stratigraphic column for core 0312-31 taken from of the inner bay margin along the Hendry Creek transect. Core shows the persistence of the mangrove peat facies through time, down to the time of supratidal / subaerial deposition. Peat persisted for at least 2320 years.

Figure 38. Stratigraphic column for core 0307-15 taken approximately 5 m seaward from of the inner bay margin along the shores of Big Hickory Bay. Core shows step-back or transgression of the inner bay margin. A storm event, represented by the shell bed sitting on top of the mangrove peat, eroded down into the underlying peat, stripping away approximately 2600 years of deposition.

Figure 39. Stratigraphic column for core 0408-11 taken from the back-barrier environment of Fort Myers Beach. Core shows history of barrier island formation.

Figure 40. Amino acid racemization dating calibration curve, relative to radiocarbon dates, for oysters collected from one core taken in the Horseshoe Keys. Calibration for D/L glutamic acid ratios. Best fit linear regression equation and goodness of fit measure reported.

Figure 41. Stratigraphic disordering among oyster amino acid racemization dates, acquired from the radiocarbon calibration equation, for samples taken from core 0307-9 (from the middle region of Fishtrap Bay, Imperial River offshore transect). The taphonomic grade of each oyster is noted; grades run from 1 (pristine) to 4 (very poorly preserved). Red dates represent the most likely disordered oysters. The lowermost date,

in purple, represents a date that is far too young given the older radiocarbon dates obtained from these depths in other cores.

Figure 42. Locations of sites 1, 6, and 22 in Estero Bay where surface sediment samples were collected for determining the activity of excess ^{210}Pb; resulting data are shown in the inset box. Sediment cores were collected at sites 1 and 22 for determination of excess ^{210}0Pb, ^{137}Cs, total aluminum, total organic carbon, and calcium carbonate.

Figure 43. Vertical profile showing water content as % wet weight for core 22.

Figure 44. Vertical profiles for natural logarithm (ln) of the activity of excess ^{210}Pb and the activity of ^{137}7Cs for core 22. Solid line on ^{210}Pb graph shows linear regression fit to the data, S = sedimentation rate, r = correlation coefficient. Dashed line on the ^{137}Cs plot shows the approximate analytical detection limit.

Figure 45. Vertical profiles for the natural logarithm (ln) of the activity of excess ^{210}Pb versus cumulative dry mass of sediment (upper graph) and activity of ^{137}Cs versus year determined from the excess ^{210}Pb data (CIC model). Right-hand axes show sediment depths in cm. Solid line on upper graph shows best fit linear regression line, S = sediment accumulation rate and r = correlation coefficient. Dashed line on the lower graph shows analytical detection limit for activity of ^{137}Cs.

Figure 46. Comparison of ages obtained by constant initial concentration (CIC) model and constant rate of supply (CRS) model for excess ^{210}Pb for core 22 from Estero Bay. Ideal 1:1 agreement between the two models is shown as a dashed line.

Figure 47. Vertical profiles for concentrations of aluminum (Al), total organic carbon (TOC) and calcium carbonate ($CaCO_3$) for sediments for core 22 from Estero Bay. Shaded area shows depth interval that corresponds to ~1950.

Figure 48. Concentrations of Al versus activity of ^{226}Ra for sediment samples from all cores collected in Estero Bay. Solid line shows linear regression fit to data, r = correlation coefficient, n = number of data points, and the dashed lines show the 95% prediction interval.

Figure 49. Vertical profiles for natural logarithm of the activity of excess ^{210}Pb and the activity of ^{137}Cs for core 1. Dashed line on the 137Cs plot shows the approximate analytical detection limit.

Figure 50. Vertical profiles for concentrations of aluminum (Al), total organic carbon (TOC) and calcium carbonate ($CaCO_3$) for sediments from core 1 in Estero Bay.

Figure 51. Locations of sites 11, 16, 17, 18, and 19 in Estero Bay where surface sediment samples were collected for determining the activity of excess ^{210}Pb; resulting data are

shown in the inset box. A sediment core was collected at site 16 for determination of excess ^{210}Pb, ^{137}Cs, total aluminum, total organic carbon, and calcium carbonate.

Figure 52. Vertical profile showing water content as % wet weight for core 16.

Figure 53. Vertical profiles for natural logarithm of the activity of excess ^{210}Pb and the activity of ^{137}Cs for core 16. Solid line on ^{210}Pb graph shows linear regression fit to the data, S = sedimentation rate, r = correlation coefficient. Dashed line on the ^{137}Cs plot shows the approximate analytical detection limit.

Figure 54. Vertical profiles for the natural logarithm (ln) of the activity of excess ^{210}Pb versus cumulative dry mass of sediment (upper graph) and activity of ^{137}Cs versus year determined from the excess ^{210}Pb data (CIC model). Right-hand axes show sediment depths in cm. Solid line on upper graph shows best fit linear regression line, S = sediment accumulation rate, and r = correlation coefficient. Dashed line on the lower graph shows analytical detection limit for activity of ^{137}Cs.

Figure 55. Vertical profiles for concentrations of aluminum (Al), total organic carbon (TOC), and calcium carbonate ($CaCO_3$) for sediments for core 16 from Estero Bay. Shaded areas shows depth intervals that corresponds to ~1950 and 1980.

Sea Level Compilation

1. 23 cm / 100 yrs
2. 4 cm / 100 yrs
3. 30-40 cm / 100 yrs

Compiled by:
Wanless et al. 1994

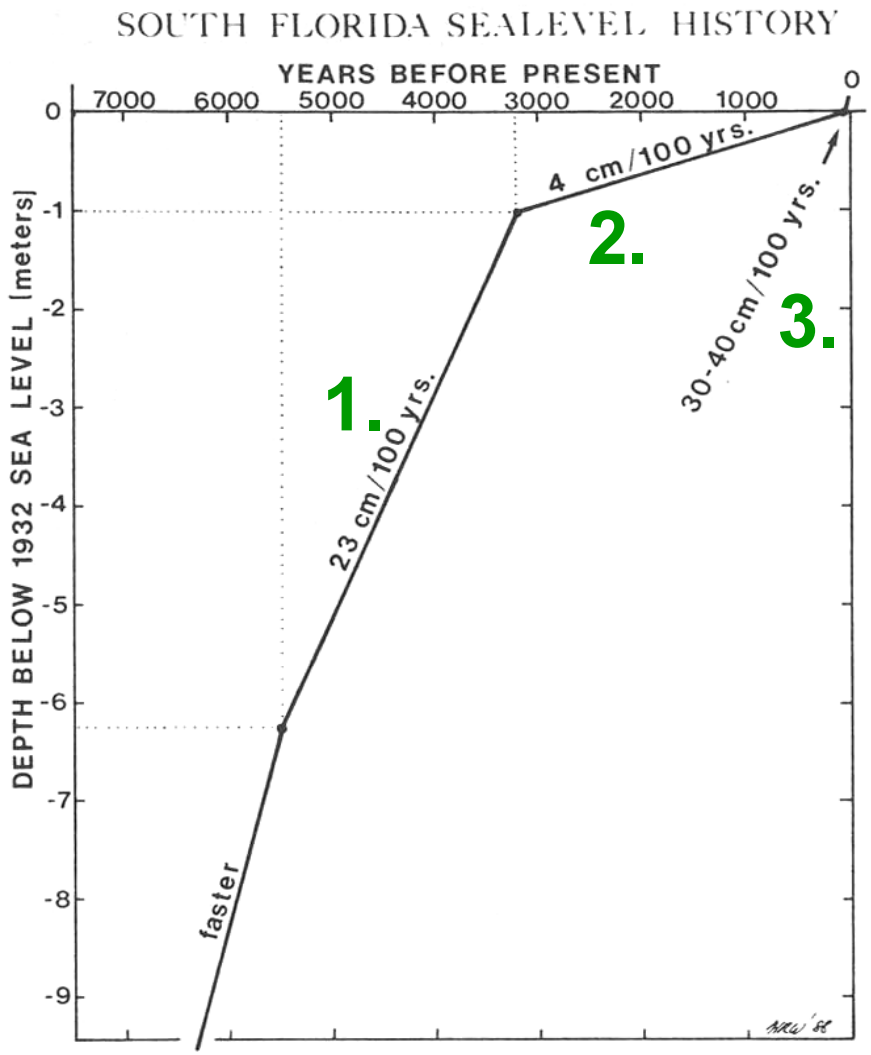

Figure 1. Sea level curve for the late Holocene compiled for south Florida taken from Wanless et al. (1994). Three phases of sea level rise are highlighted: 1. from 5500-3200 ybp with a rate of 23 cm / 100 yrs; 2. from 3200-200 ybp with a rate of 4 cm / 100 yrs; and 3. from 200-present with a rate of 30-40 cm / 100 yrs.

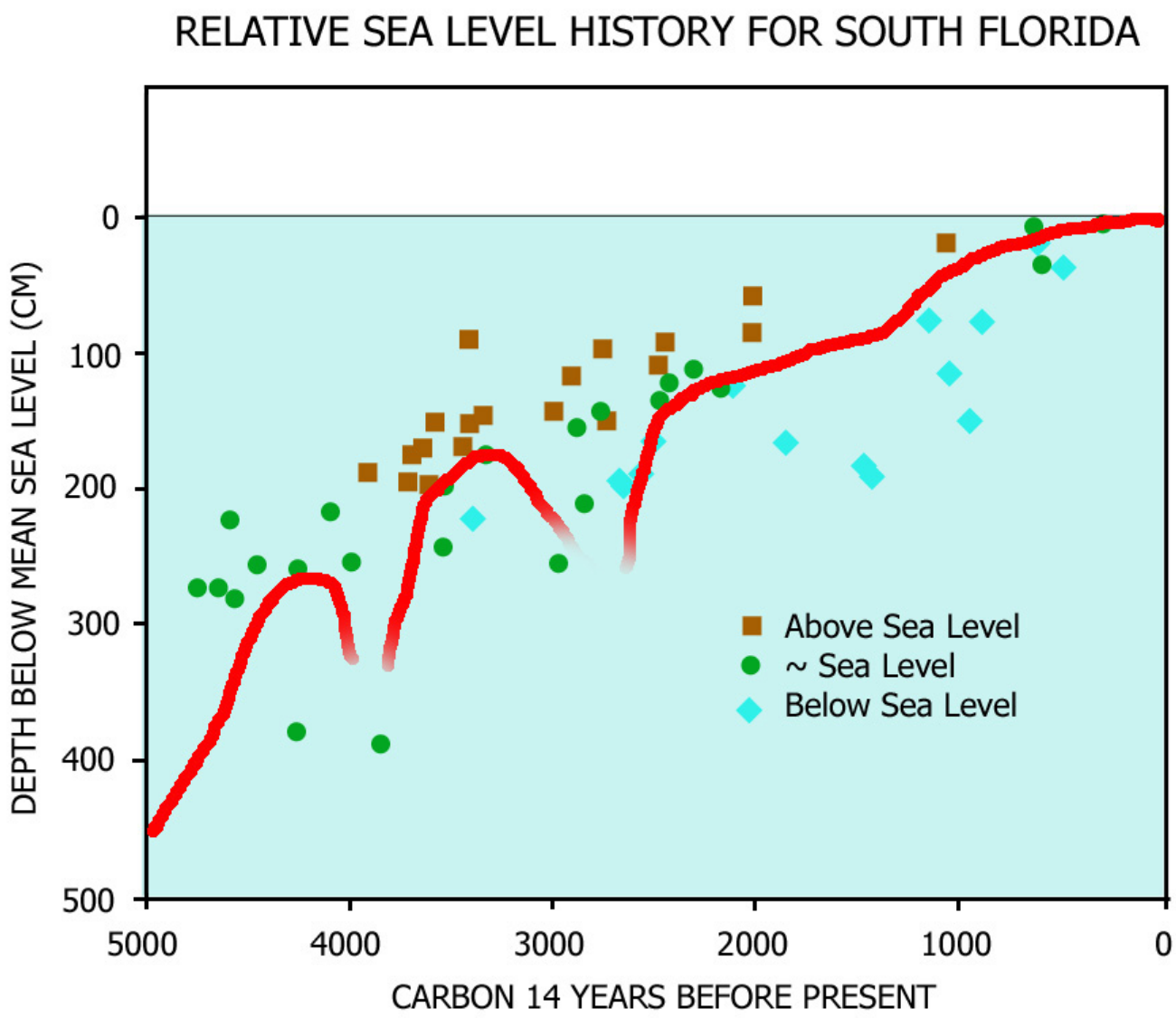

Figure 2. A high-frequency sea-level oscillation curve for the late Holocene of south Florida; modified after Gelsanliter and Wanless (1995).

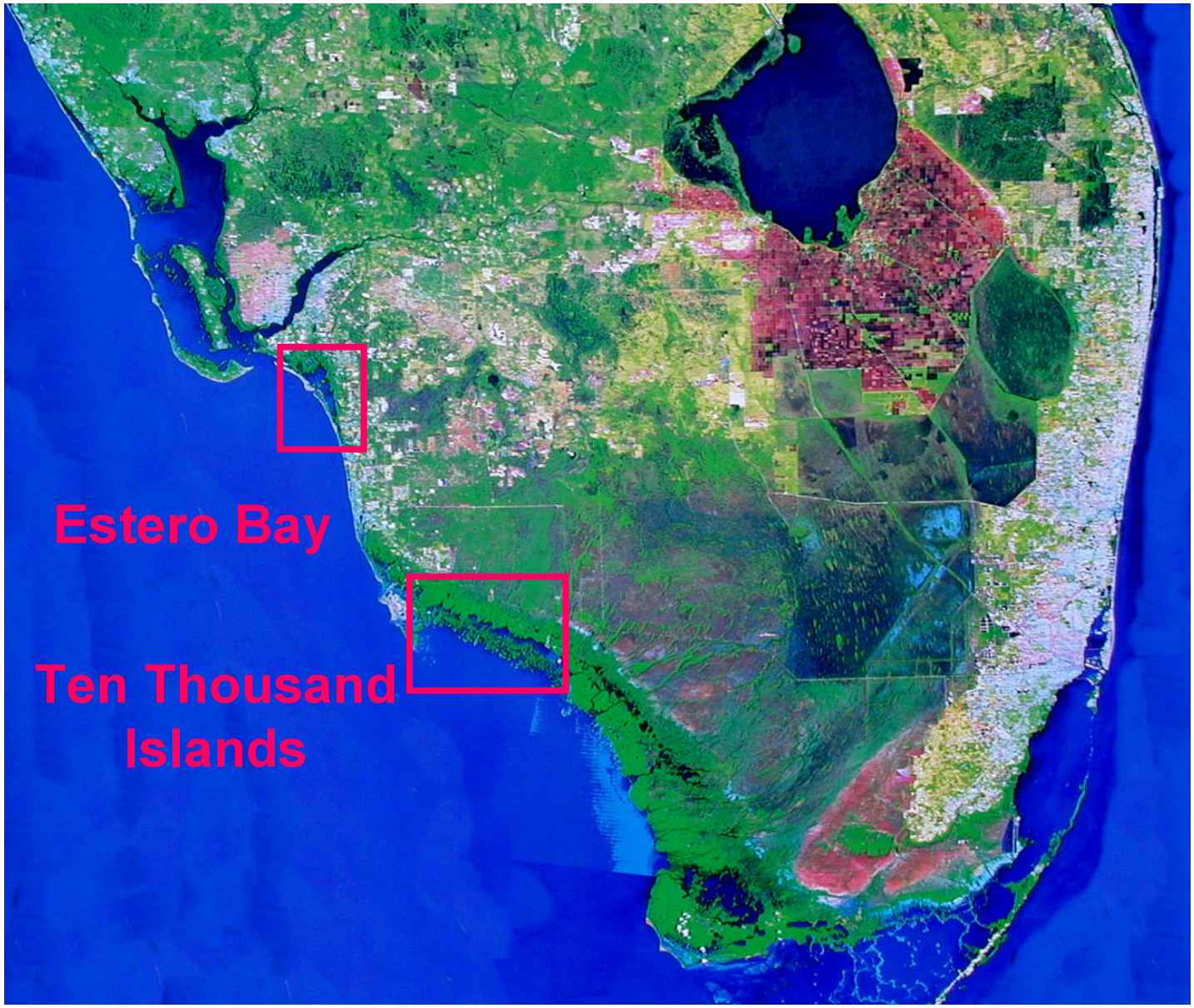

Figure 3. Satellite image of the Greater Everglades of south Florida. Two regions are highlighted: Ten Thousand Islands and Estero Bay. The former is the type region for the Ten Thousand Islands Geomorphology. Estero Bay is the study region for this project. It too exhibits the Ten Thousand Islands Geomorphology, but also has coastal barrier islands at the seaward margin.

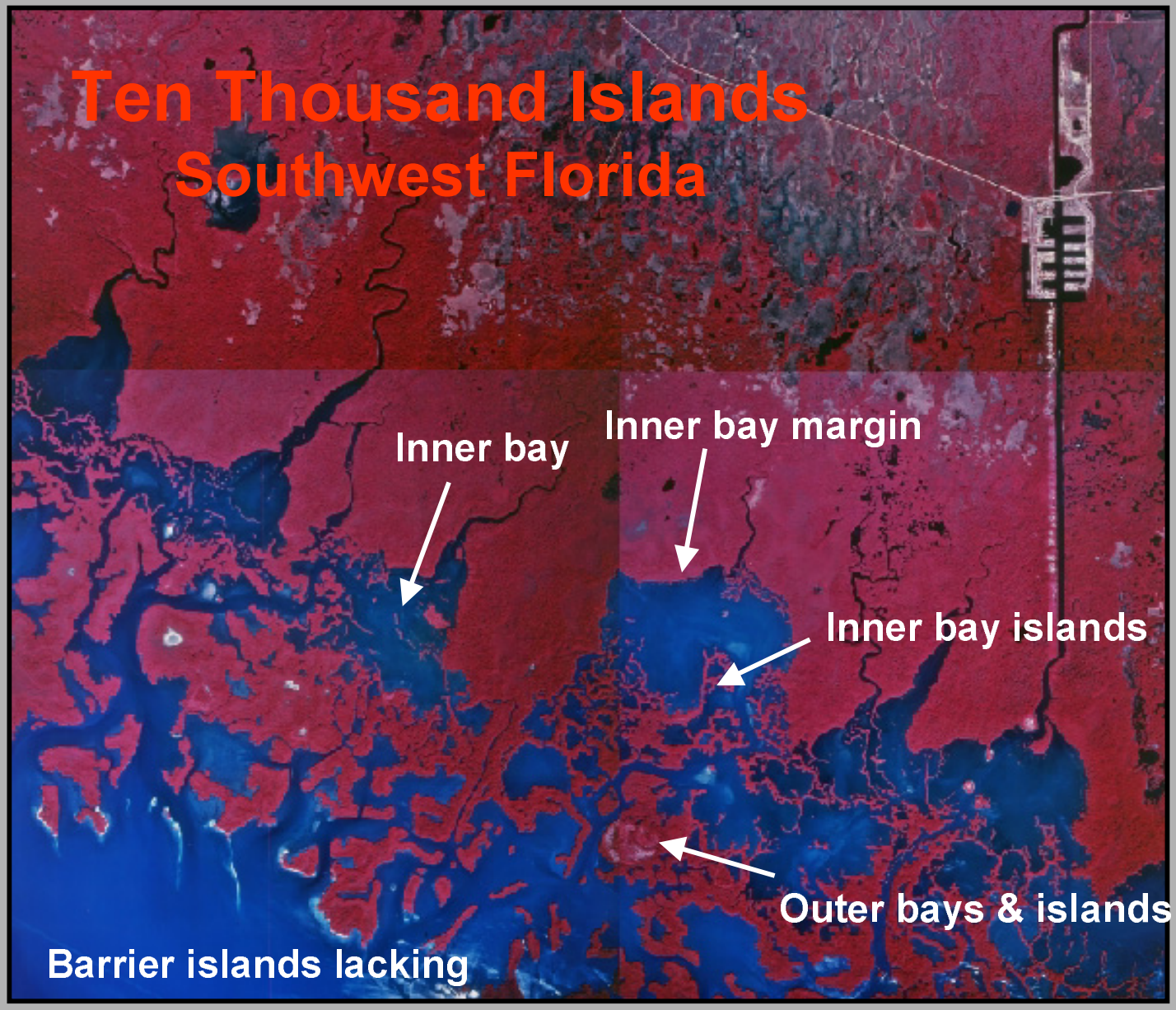

Figure 4. Close-up satellite view of the Ten Thousand Islands in Southwest Florida exhibiting the Ten Thousand Islands Geomorphology. Characterisitic elements of the geomorphology include: inner bay margin, inner bay, inner bay islands, and outer bays and islands. Longshore transport is minimal here so barrier islands are absent.

Position of Shoreline without Late Holocene Sedimentation

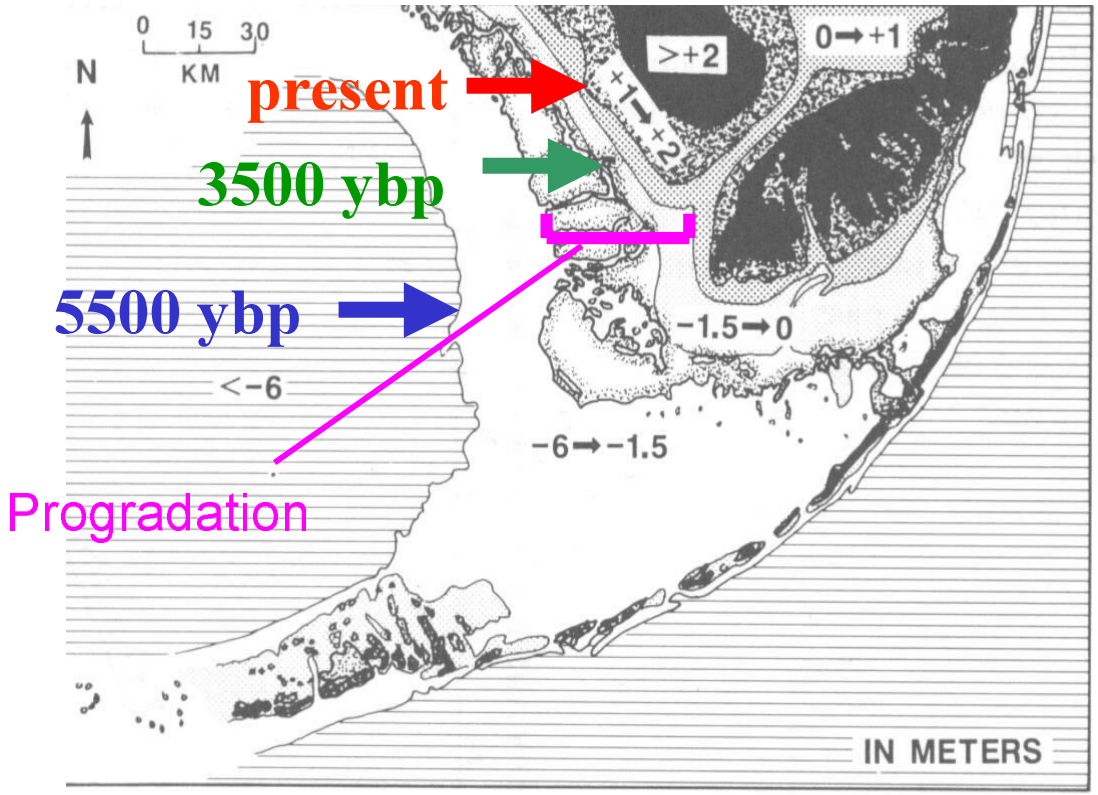

From Wanless et al. 1994.

Figure 5. The approximate position of the coastline in south Florida is depicted here assuming no sedimentation occurred and sea level rise proceeded at the rate measured during the late Holocene. This effectively would eliminate coastal progradation during the last 3200 years. Taken from Wanless et al. (1994).

Tide Gauge Data for Key West

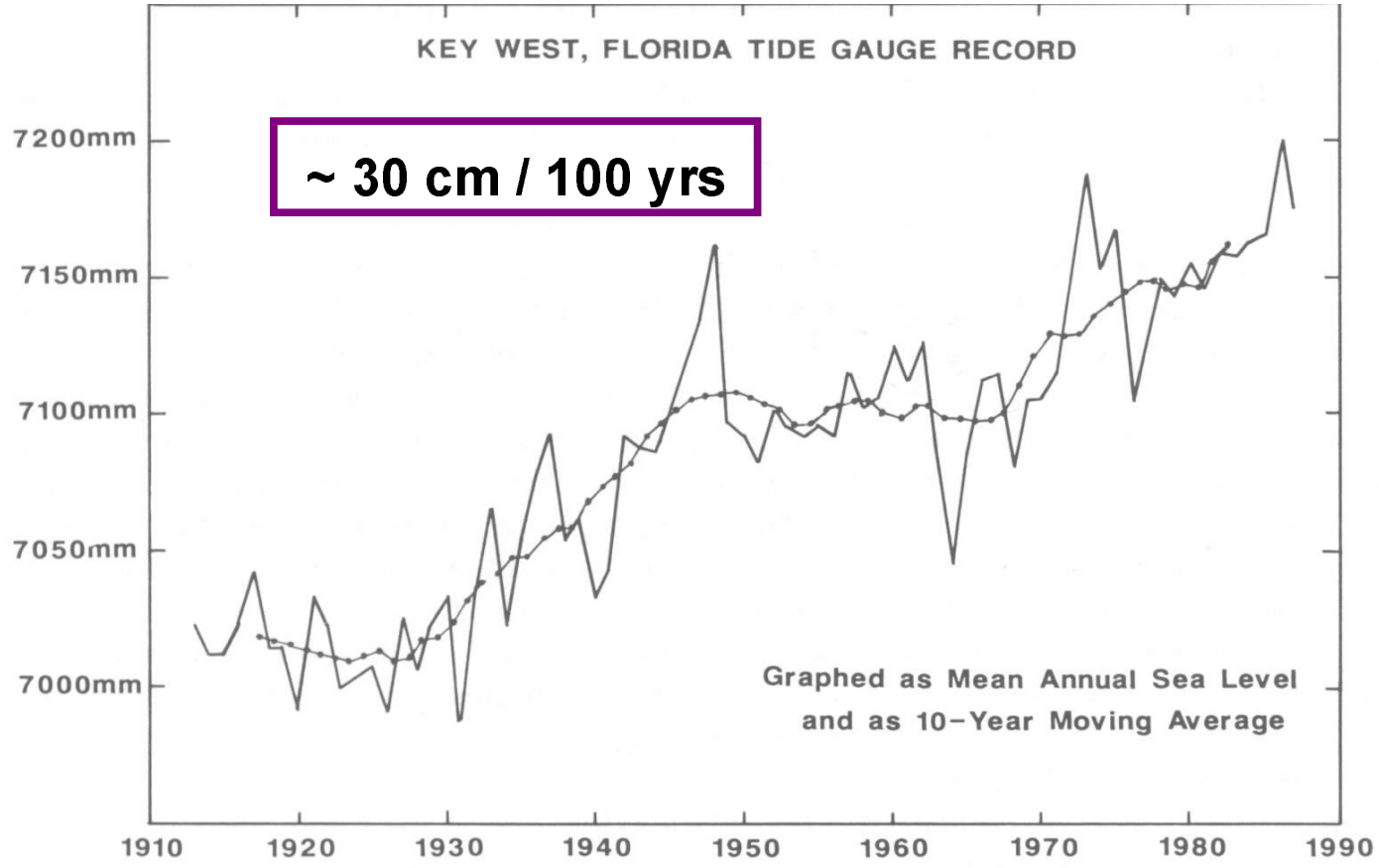

From Maul & Martin 1993

Figure 6. Tide gauge data compiled for Key West from 1910-1990. Taken from Maul and Martin (1993). The smoothed curve represents the position of sea level for the same time interval and has a slope equal to approximately 30 cm / 100 yrs. This sea level rise rate is an order of magnitude higher than those measured for the preceding 3000 years.

Ft Myers Tide Data
1966-1997

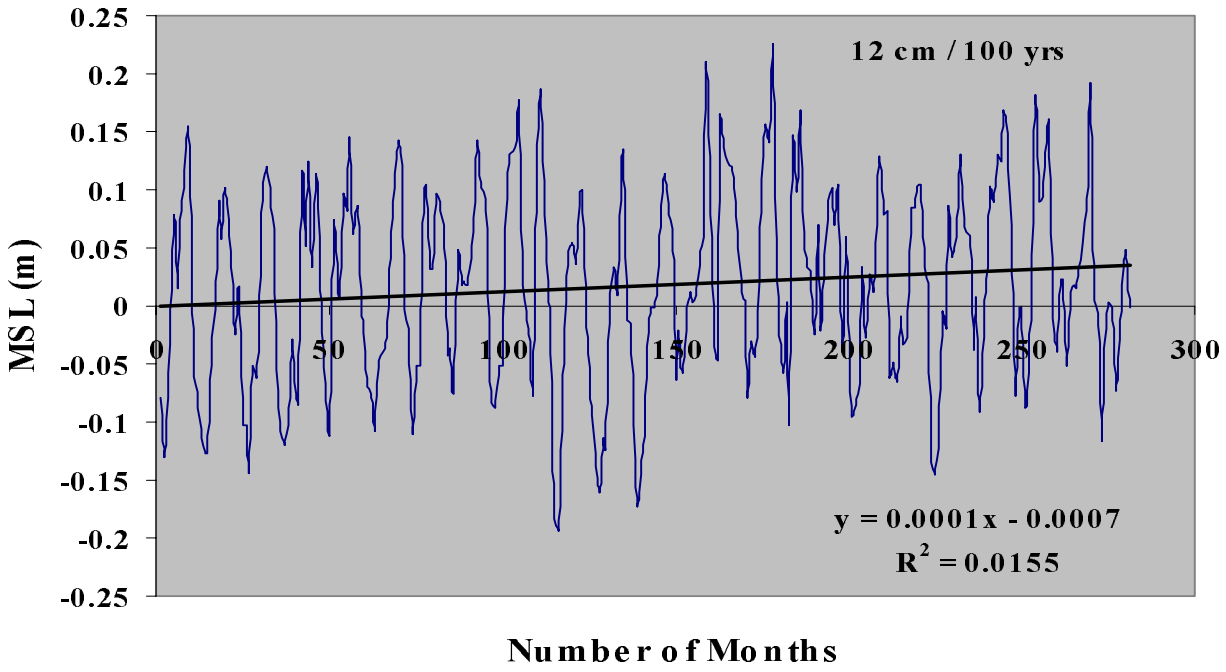

Rise rates between 12 - 48 cm / 100 years for S FL locations

Figure 7. Tide gauge data compiled for Fort Myers from 1966-1997. The smoothed curve yields a sea level rise rate of 12 cm / 100 yrs. When this analysis is completed and compiled for all localities peninsular coastal Florida, the rise rate ranges from 12 – 48 cm / 100 yrs.

Figure 8. Photograph of oyster reef exposed at low tide in the Horseshoe Keys region of north-central Estero Bay. The effects of progradation are shown: mangrove propagules and seedlings have rooted on the oyster reef.

Figure 9. Satellite image of Estero Bay showing 3 watersheds included in this study: 1. Hendry and Mullock Creek; 2. Estero River; and 3. Imperial River. The following geomorphologic features are noted: inner bay margin, inner bay islands, barrier islands, and flood tidal delta islands.

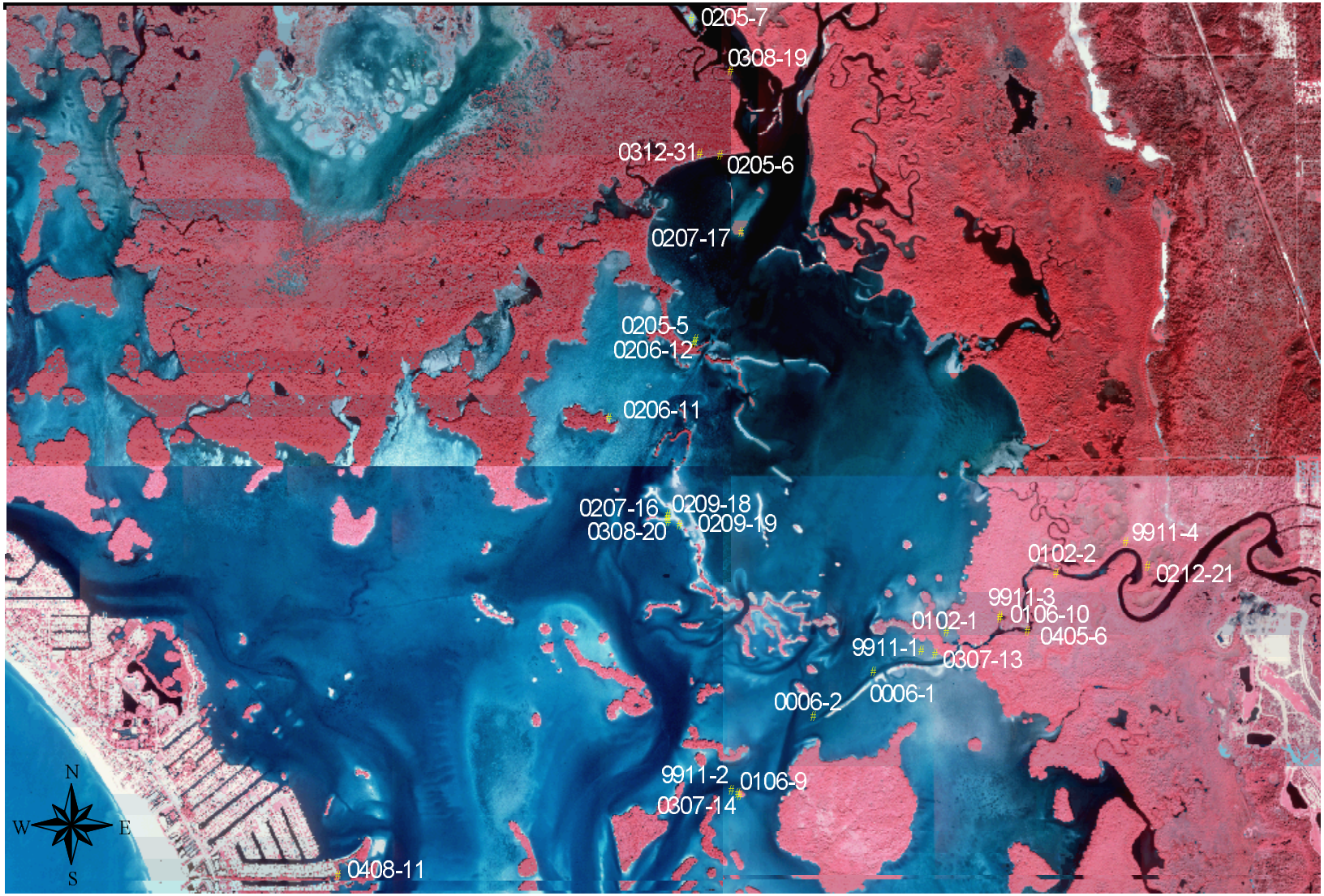

Figure 10. Location of late Holocene sediment cores taken in northern Estero Bay. Localities fall on 2 transects: the Hendry Creek transect, and the Estero River transect. Cores 0207-16, 0209-18, are 0209-19 from the Horseshoe Keys used in the study of oyster reef history.

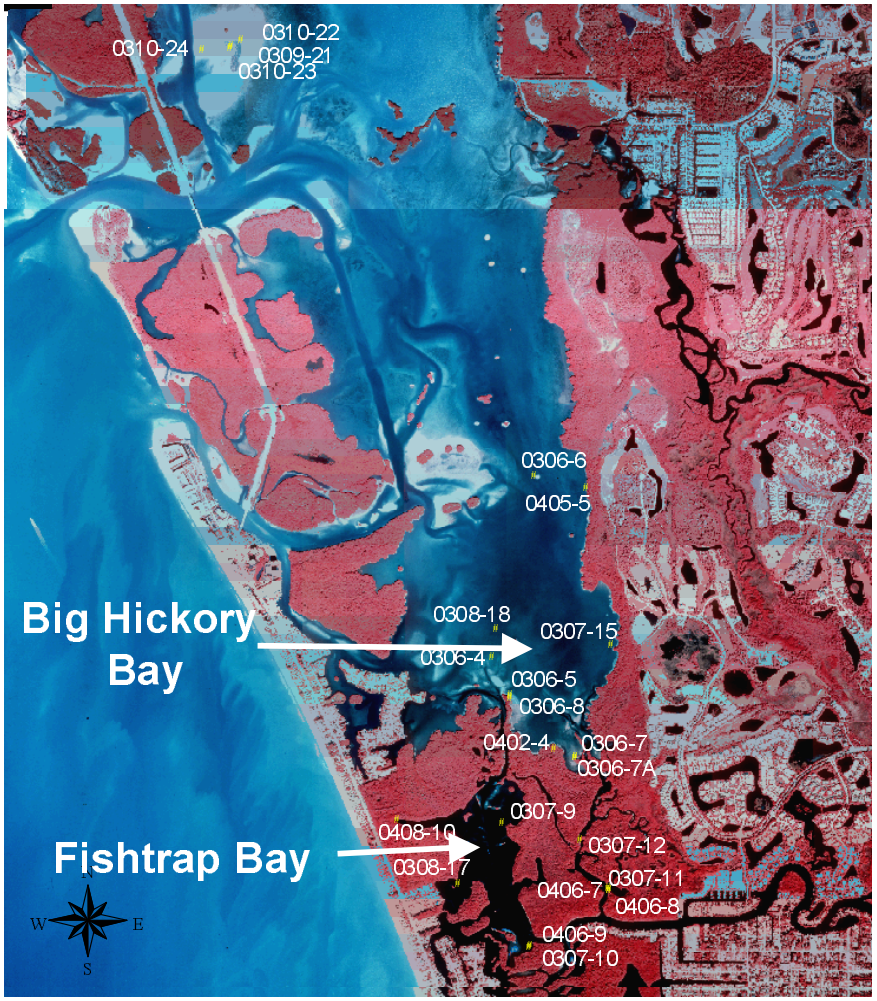

Figure 11. Location of late Holocene sediment cores taken in southern Estero Bay. Localities fall on 2 transects within the Imperial River: an inshore transect that traverses the eastern margin of Estero Bay, and the offshore transect that traverses the western margin of Estero Bay. Cores taken in the northwest region (0309-21, 0310-22, 0310-23, and 0310-24) are located on an inactive tidal delta behind a closed tidal inlet (due to road construction). These cores were part of a student project; data are not included herein, but are available upon request.

Figure 12. Photograph of a hand core being taken.

Figure 13. Photograph of a vibracore being taken on a Horseshoe Keys' reef.

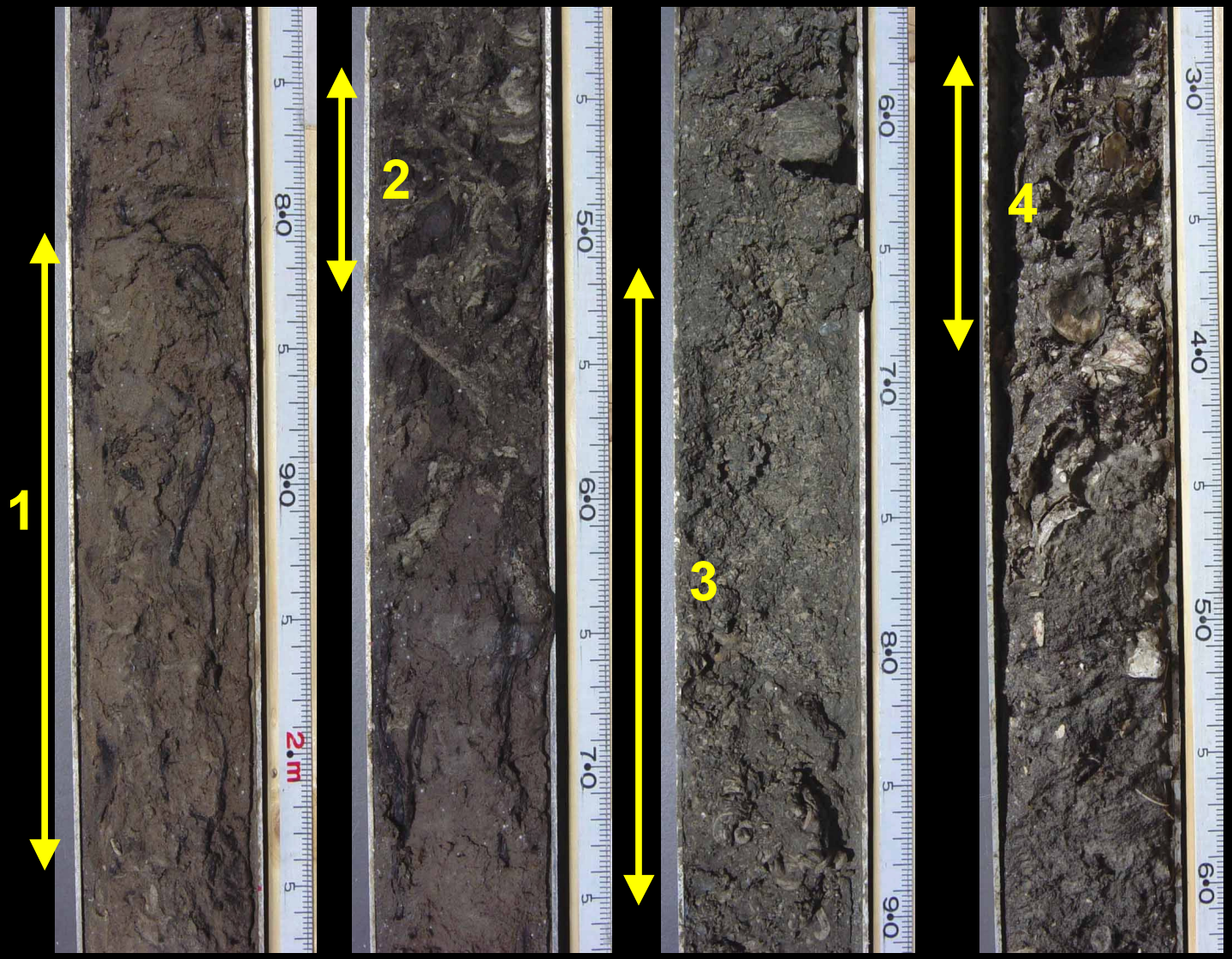

Figure 14. A split core showing some of the common facies. 1: Supratidal / subaerial sands. 2: Intertidal mangrove peat. 3: Vermetiform-dominated shallow subtidal reef. 4: Oyster-dominated intertidal brackish reef.

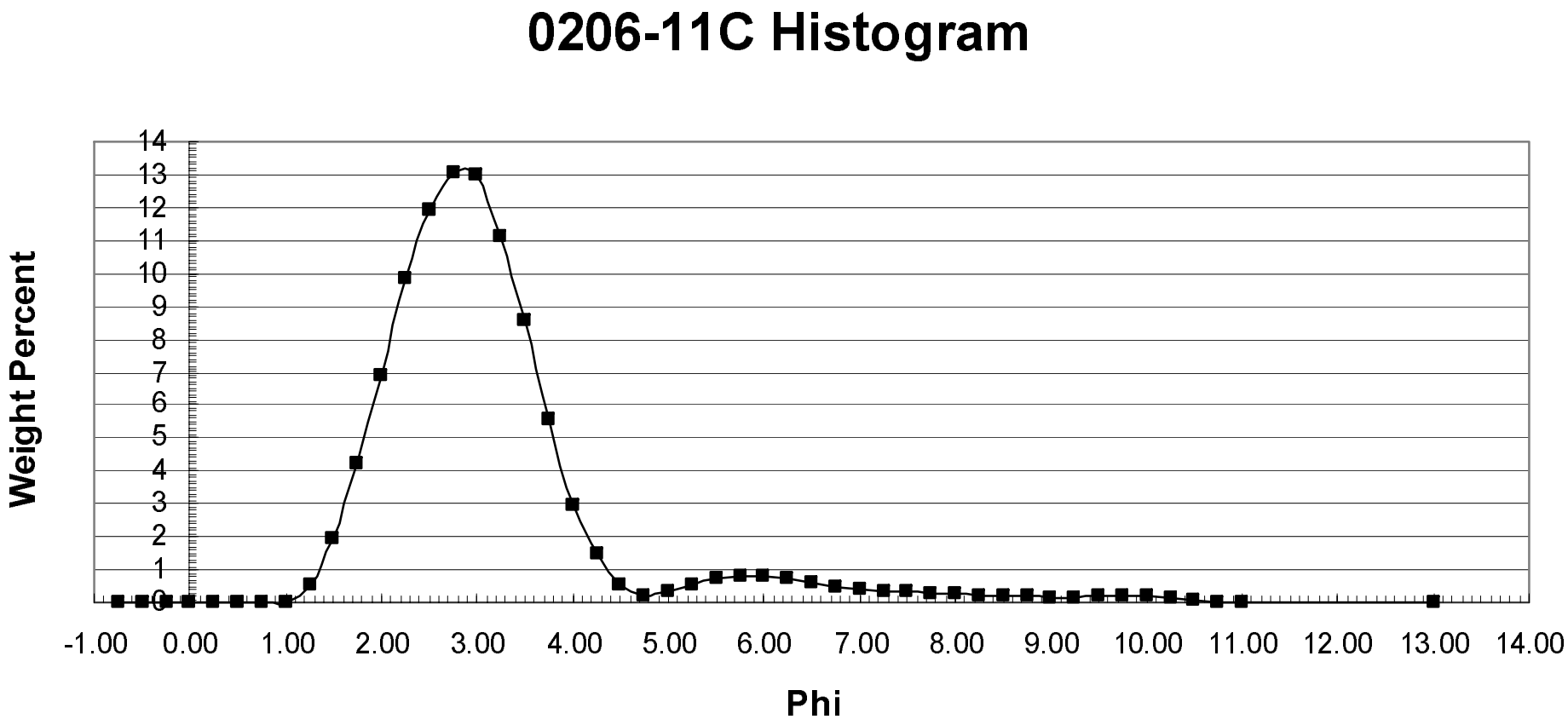

Figure 15. Sample grain size histogram (core 0206-11, facies C) for data derived from laser coulter counter. Grain size reported in units of phi. The complete set of histograms is included in Appendix B.

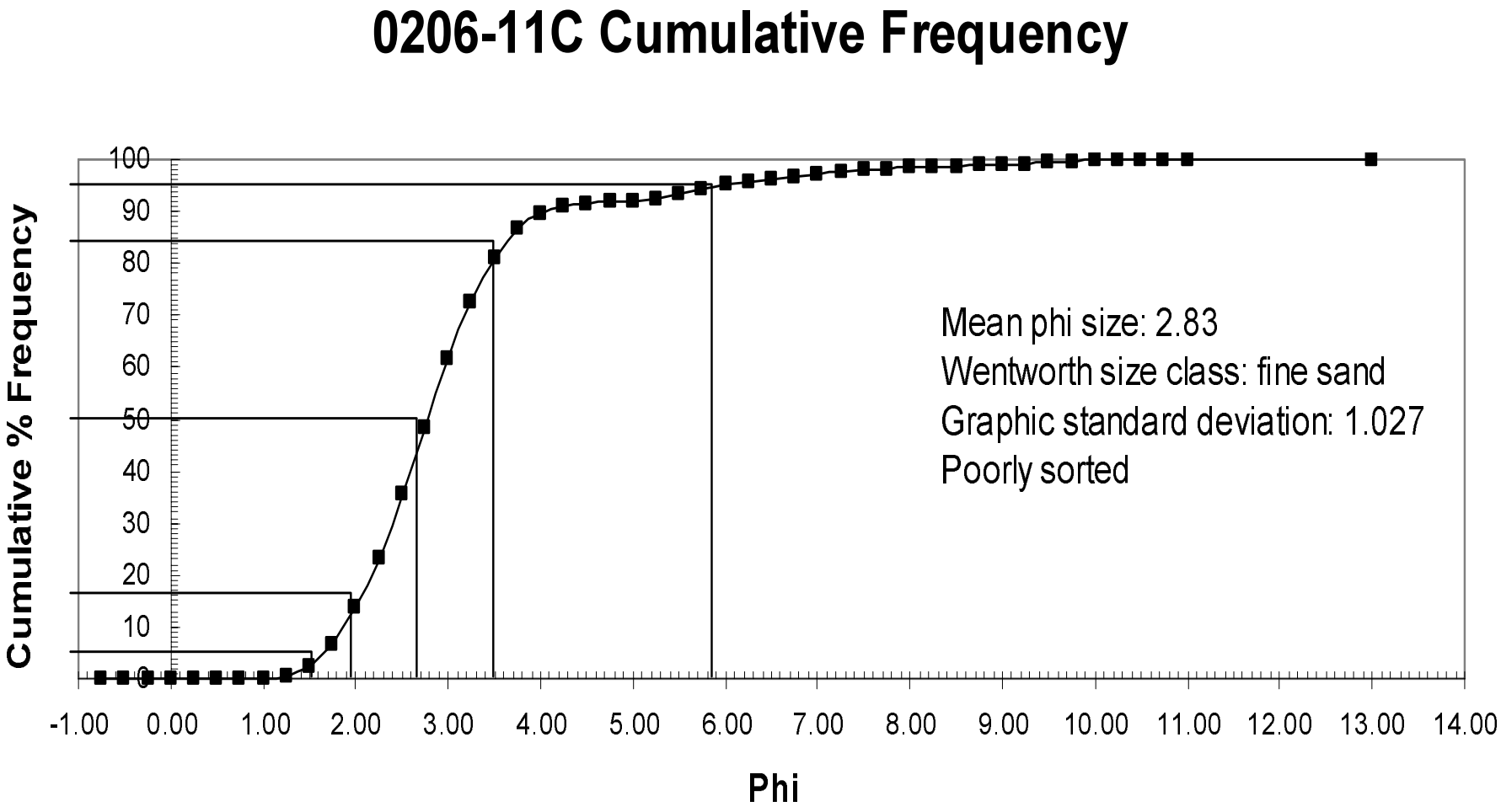

Figure 16. Cumulative percent weight frequency plot for same sediment sample plotted in Figure 15. The Folk graphical method was used to acquire a value for mean grain size and sorting. The complete set of plots is included in Appendix B.

Anomalocardia auberiana

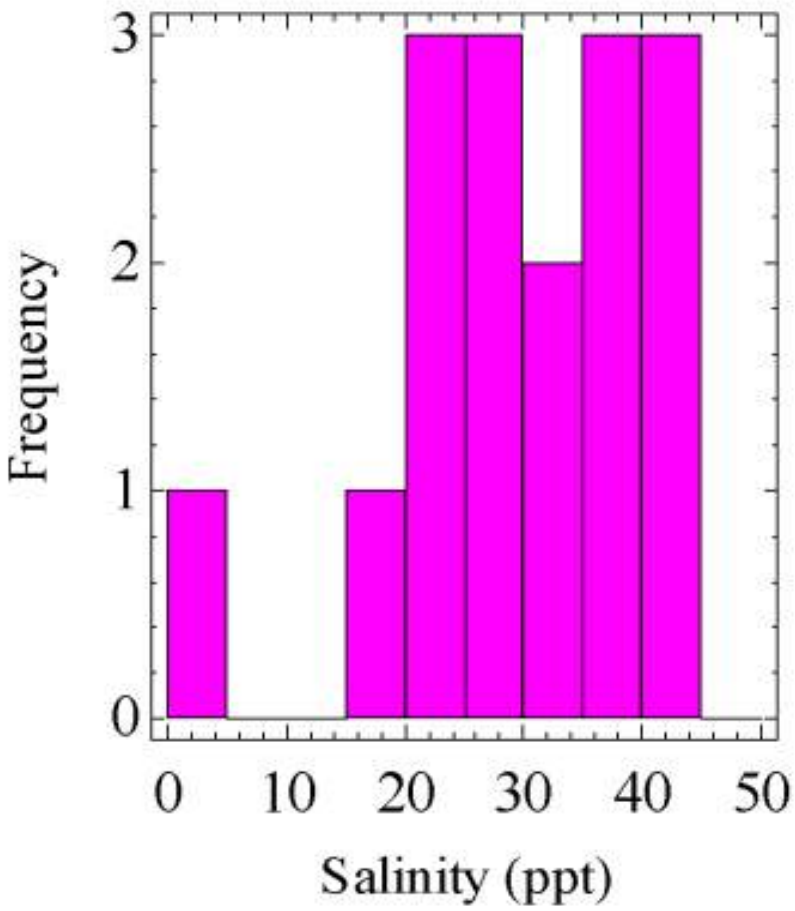

Salinities of Occurrence For Bivalve *Anomalocardia*

- **Living occurrences from FL and Biscayne Bays**
- **Monitoring by L. Wingard, USGS**

Figure 17. Histogram of salinity occurrences of the living bivalve *Anomalocardia auberiana* derived from recent monitoring data in Florida and Biscayne Bays (by U.S. Geological Survey). This is a sample of one histogram; the complete set is available in the report by Savarese & Wingard (2004).

Figure 18. Satellite image of the Horseshoe Keys region in north-central Estero Bay. This is the region in which the oyster reef history study was conducted. Inset shown as close-up image in Figure 19.

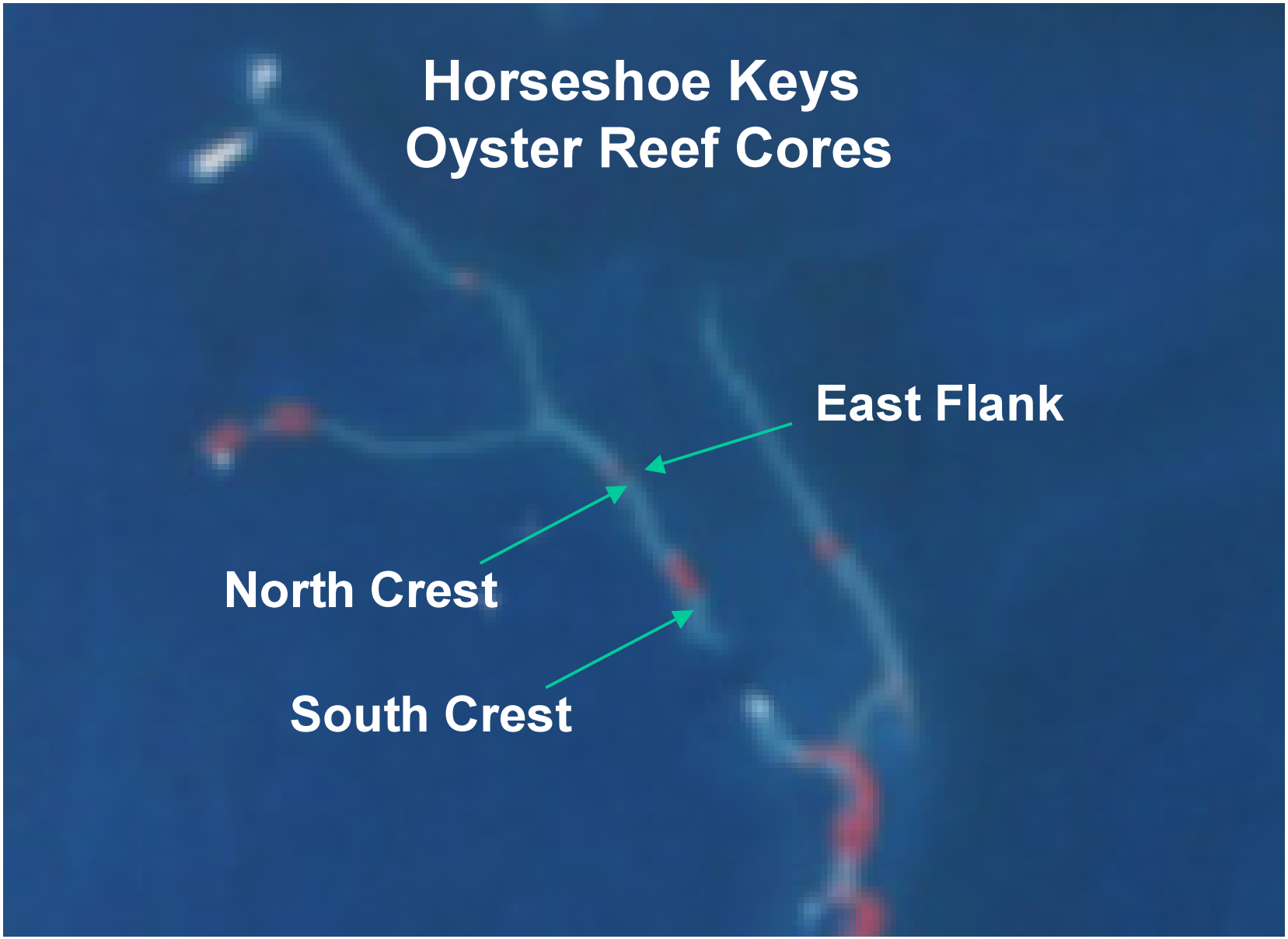

Figure 19. Close-up image of reefs in northern Horseshoe Keys. Arrows denote the locations of the 3 cores.

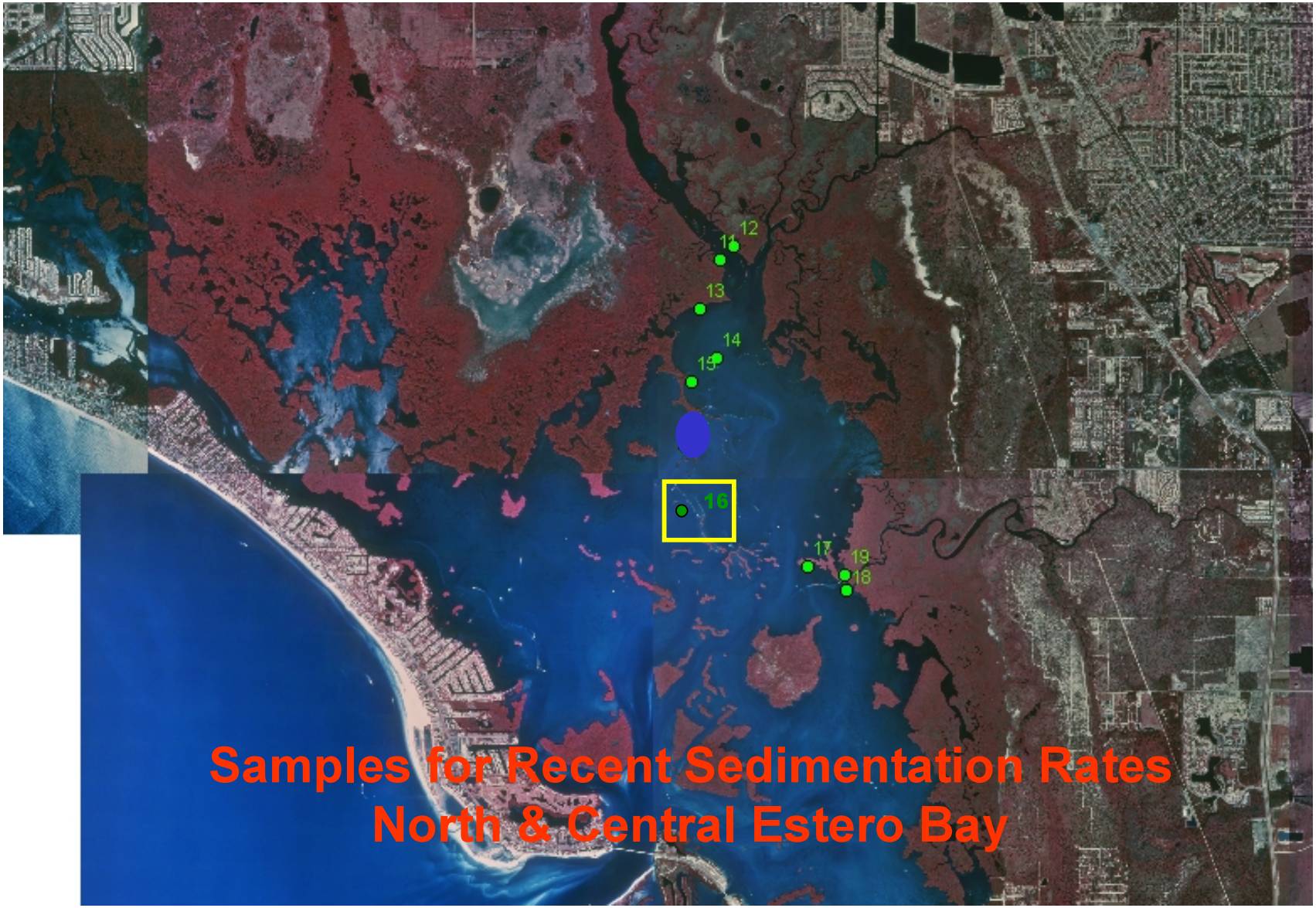

Figure 20. Map showing location of sediment samples taken in northern Estero Bay for recent sedimentation rate determination. Location 16 had the best in-sediment radiogenetic activity and therefore was chosen for further study.

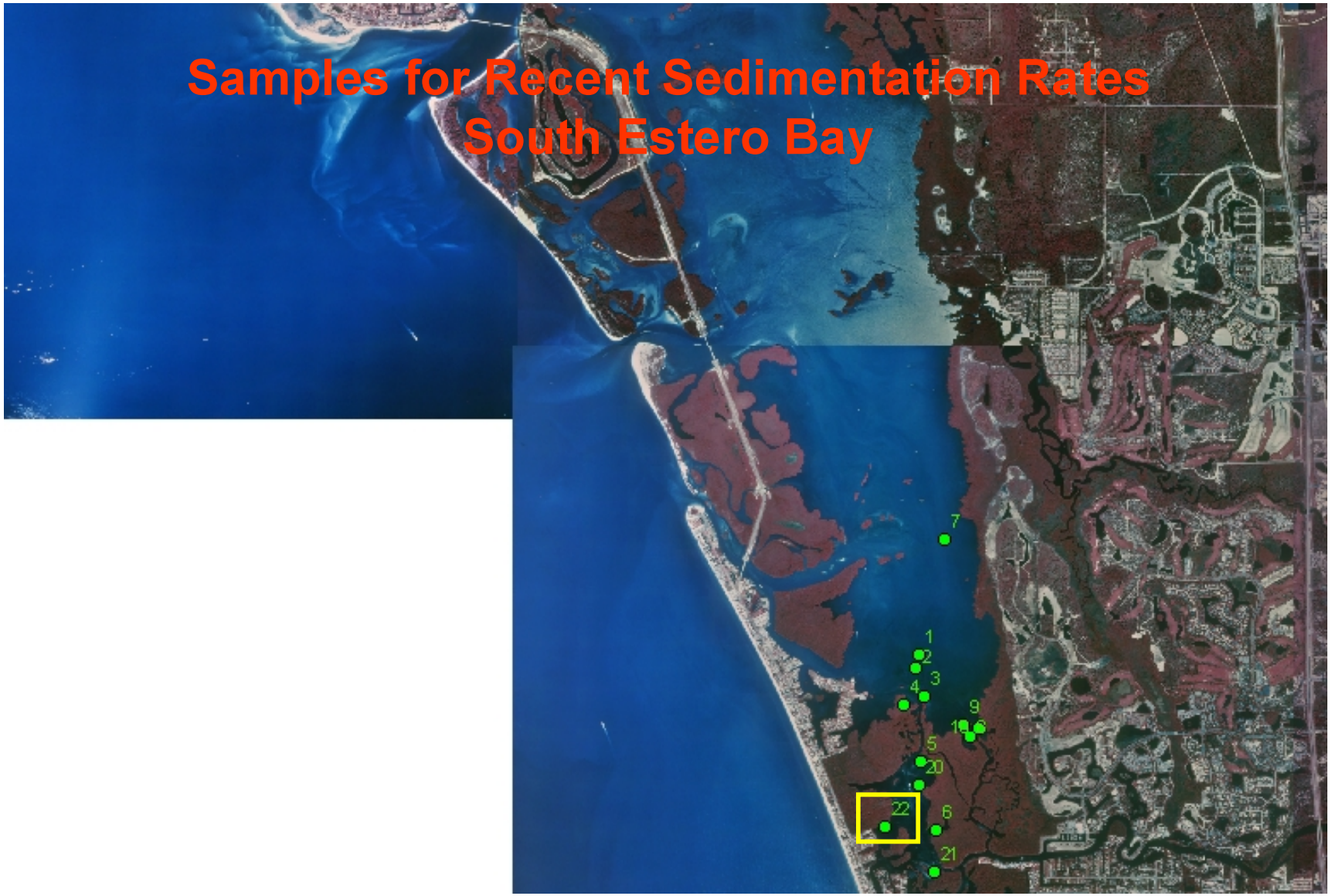

Figure 21. Similar image for southern Estero Bay showing the location of sediment samples for recent sedimentation rate determination. Location 22 had the best in-sediment radiogenetic activity and therefore was chosen for further study.

Figure 22. Photograph of a SCUBA diver taking one of the sedimentation rate cores.

Figure 23. Photograph of core sediment extraction for high-resolution geochronology work.

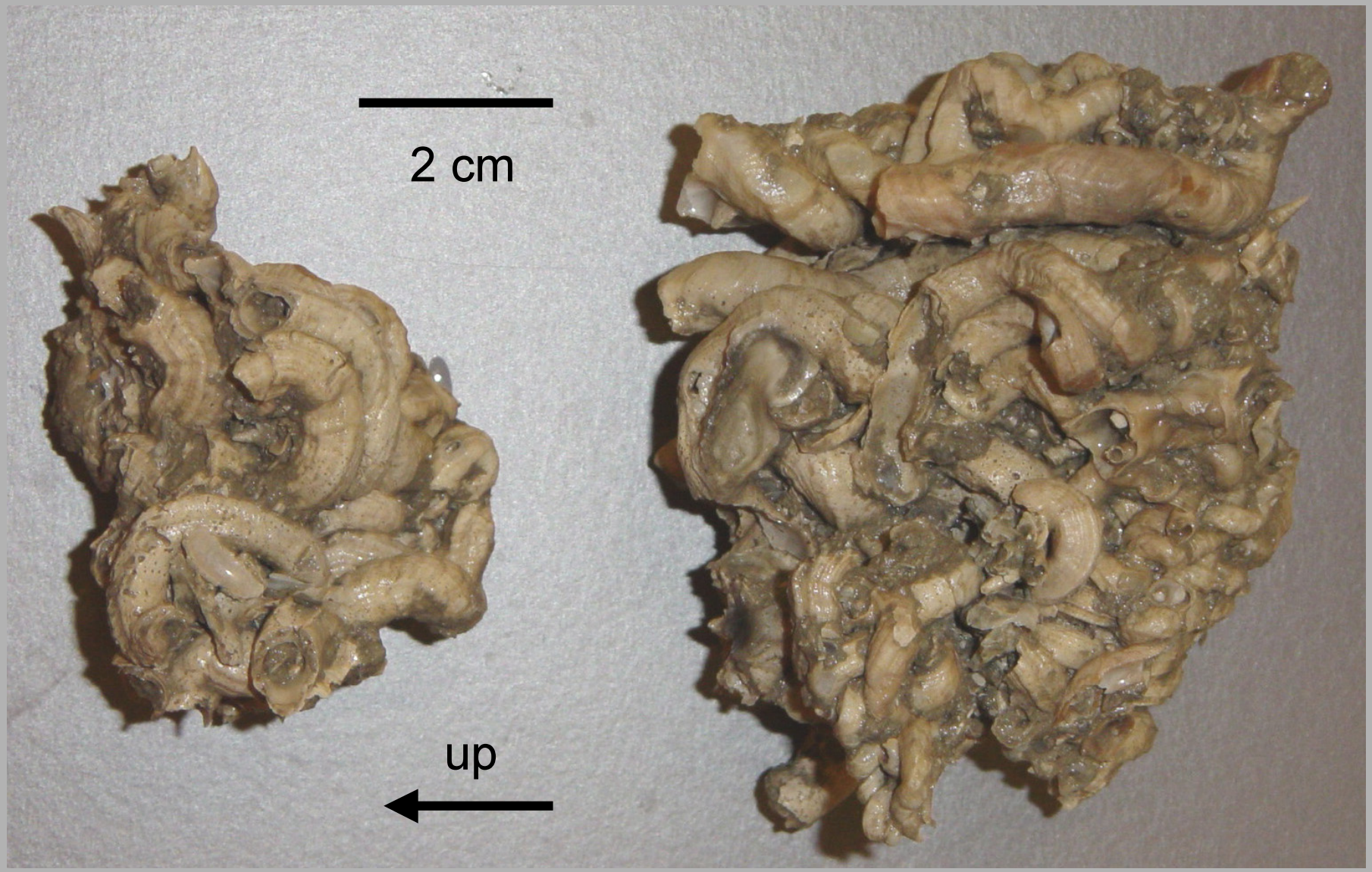

Figure 24. Photograph of reef-forming vermetiform gastropods (the turritellid *Vermicularia*) removed from a core traversing the vermetiform gastropod-dominated reef facies. Specimens were oriented in the core tube as displayed by the up arrow.

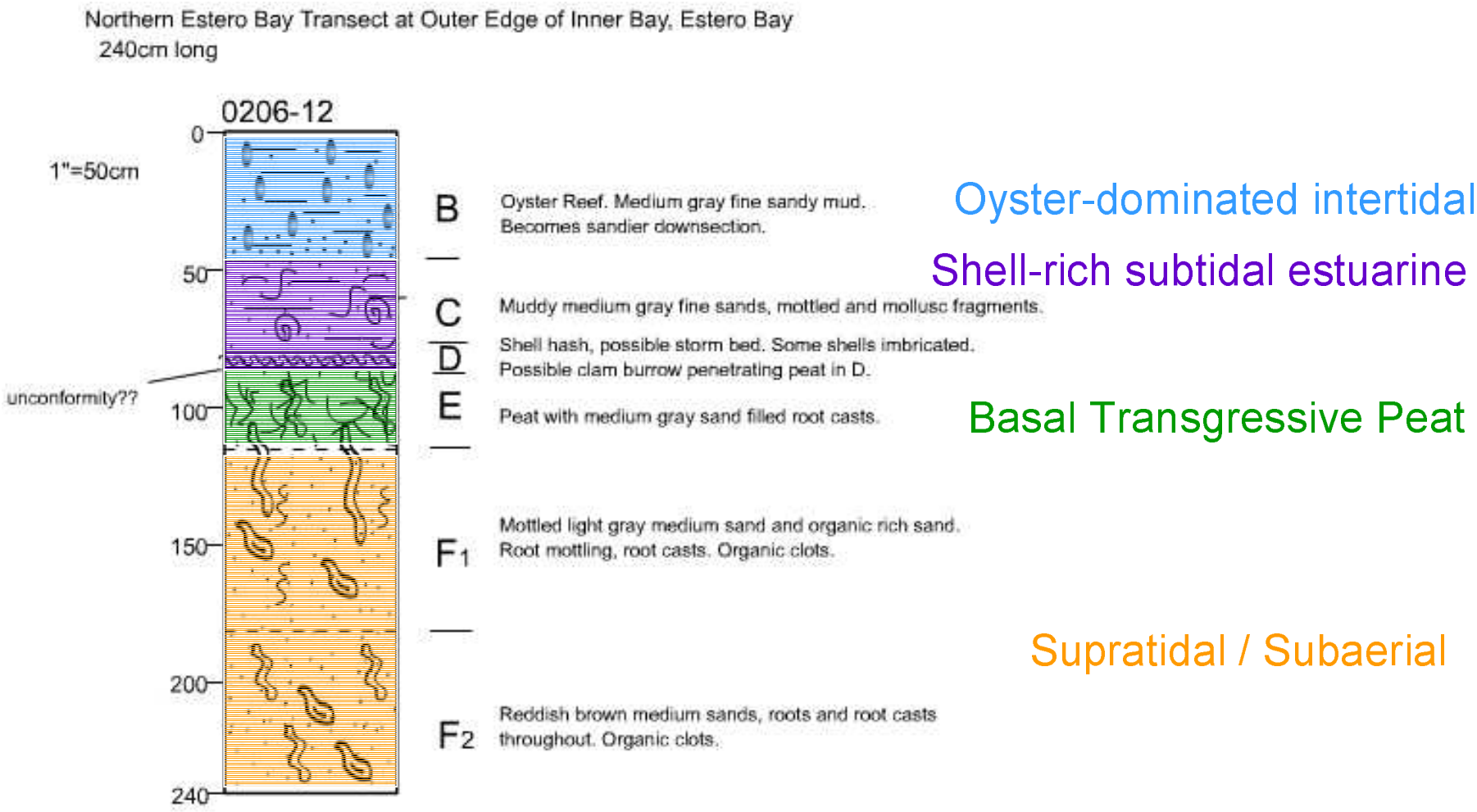

Figure 25. Stratigraphic column for core 0206-12 taken from the outer edge of the inner bay, Hendry Creek transect. Stratigraphy shows the younger transgressive – regressive cycle; facies interpretations are noted alongside the column and are color-coded (following the same scheme defined for the fence diagrams [see Figure 28]).

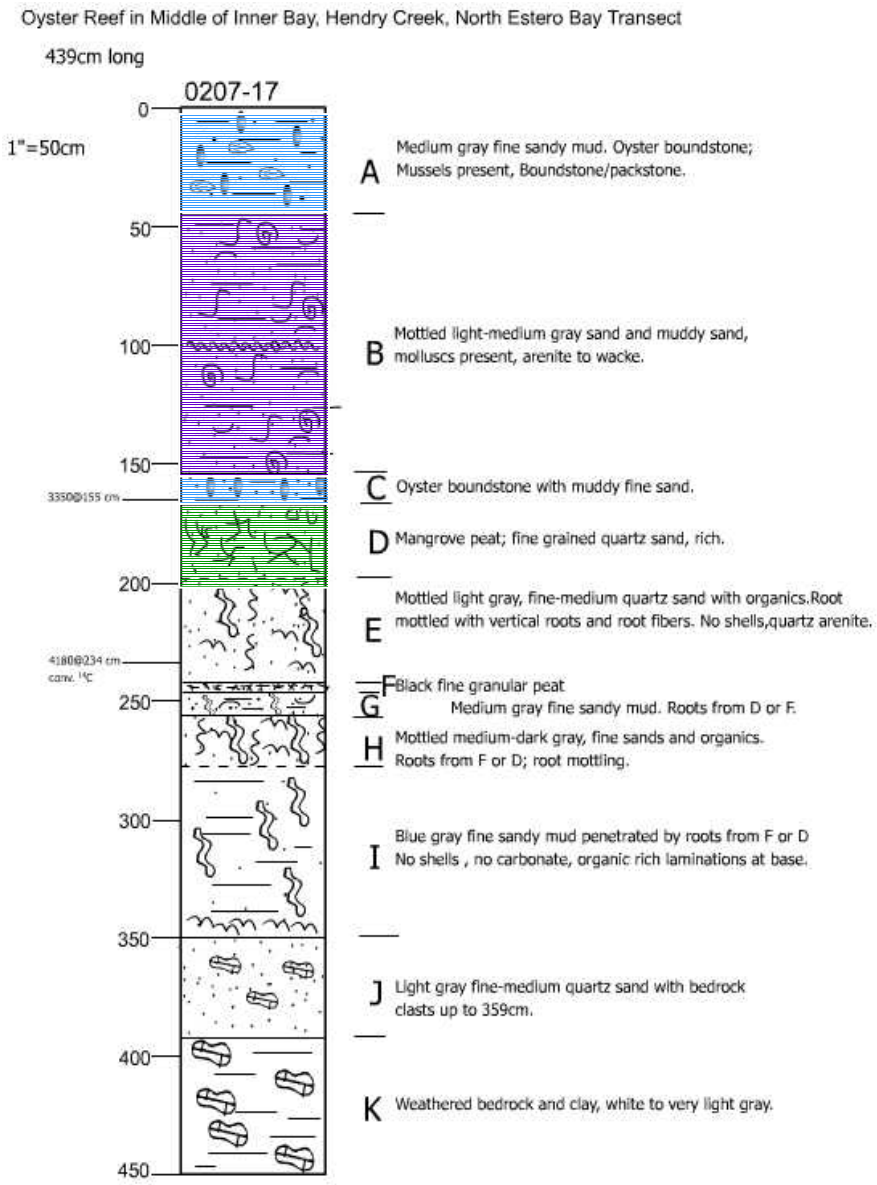

- **B-A: Regr to more brackish**
- **C-B: Transgr to high salinity estuarine**
- **D-C: Transgr to brackish**
- **D: Basal transgr peat**

Figure 26. Stratigraphic column for core 0207-17 taken from the middle region of the inner bay, Hendry Creek transect. Stratigraphy shows the younger transgressive – regressive cycle; interpretations are noted alongside the column, and facies are color-coded (following the same scheme defined for the fence diagrams [see Figure 28]).

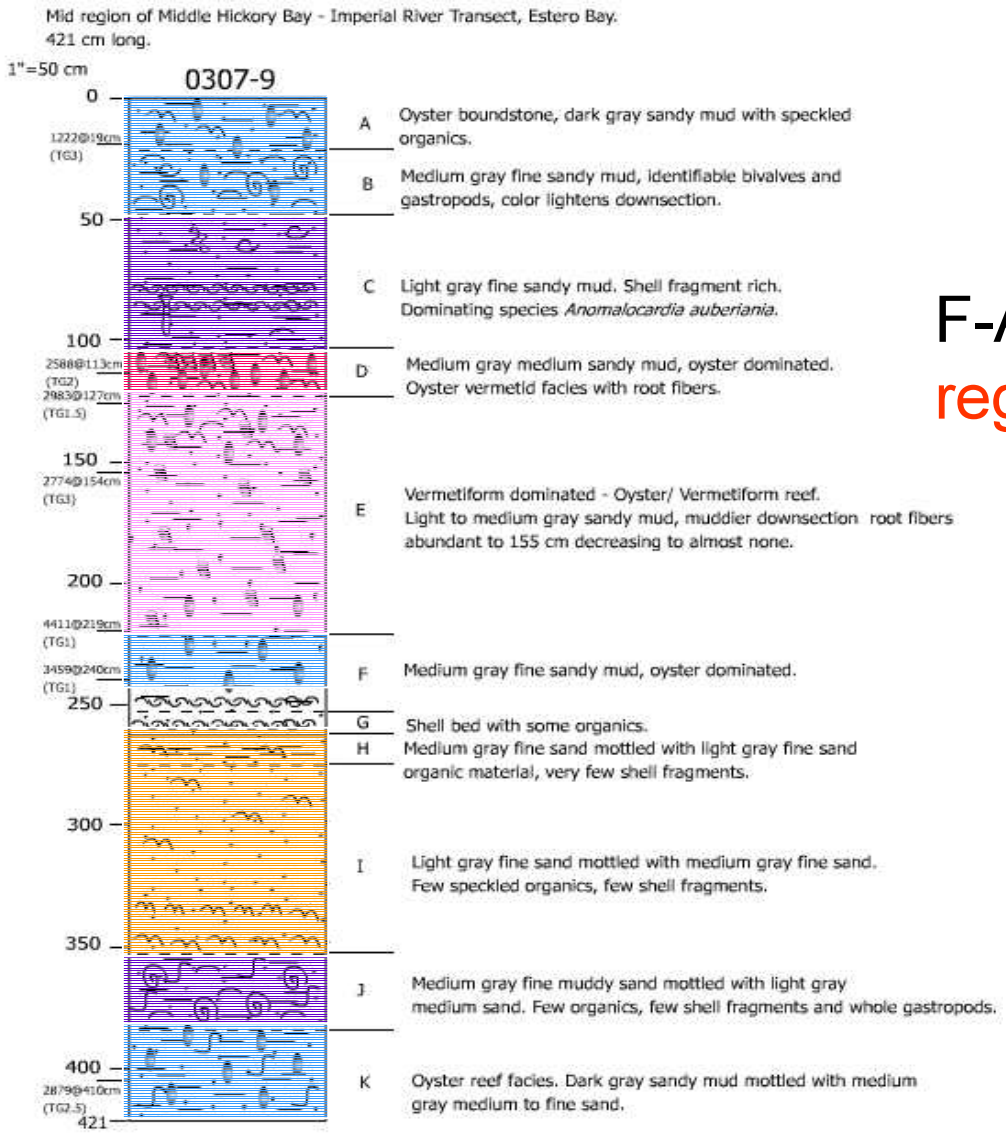

F-A: Second transgr / regr cycle

K-H: First transgr / regr cycle

Figure 27. Stratigraphic column for core 0307-9 taken from the middle region of Fishtrap Bay, Imperial River transect. Stratigraphy shows the younger and older transgressive – regressive cycles; interpretations are noted alongside the column, and facies are color-coded (following the same scheme defined for the fence diagrams [see Figure 28]).

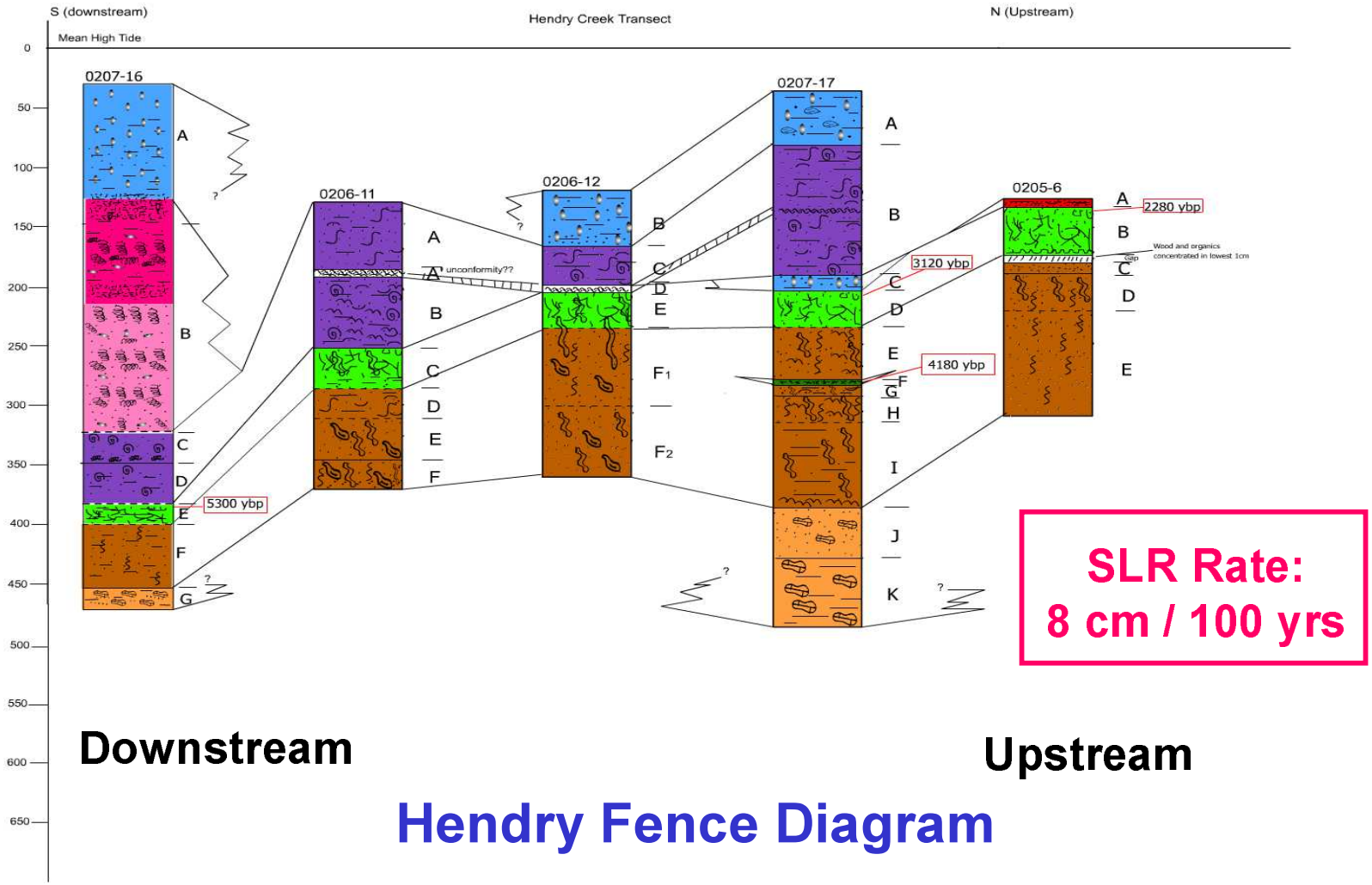

Figure 28. Fence diagram for the Hendry Creek transect. Cores are oriented, from left to right, downstream (south) to upstream (north). Positions and ages of the basal transgressive peats were used to calculate a sea level rise rate of 8 cm / 100 yrs. Facies are colored-coded as follows: tan = regolith; brown = supratidal / subaerial; dark green = freshwater peat; light green = intertidal, mangrove peat; dark blue = organic-rich, shell-poor subtidal sands and muds; purple = shell-rich subtidal sands and muds; light blue = intertidal, oyster reef; pink = subtidal vermetiform gastropod-dominated reef; magenta = subtidal oyster – vermetiform gastropod reef; red = intertidal mud or sand flat; yellow = riverine.

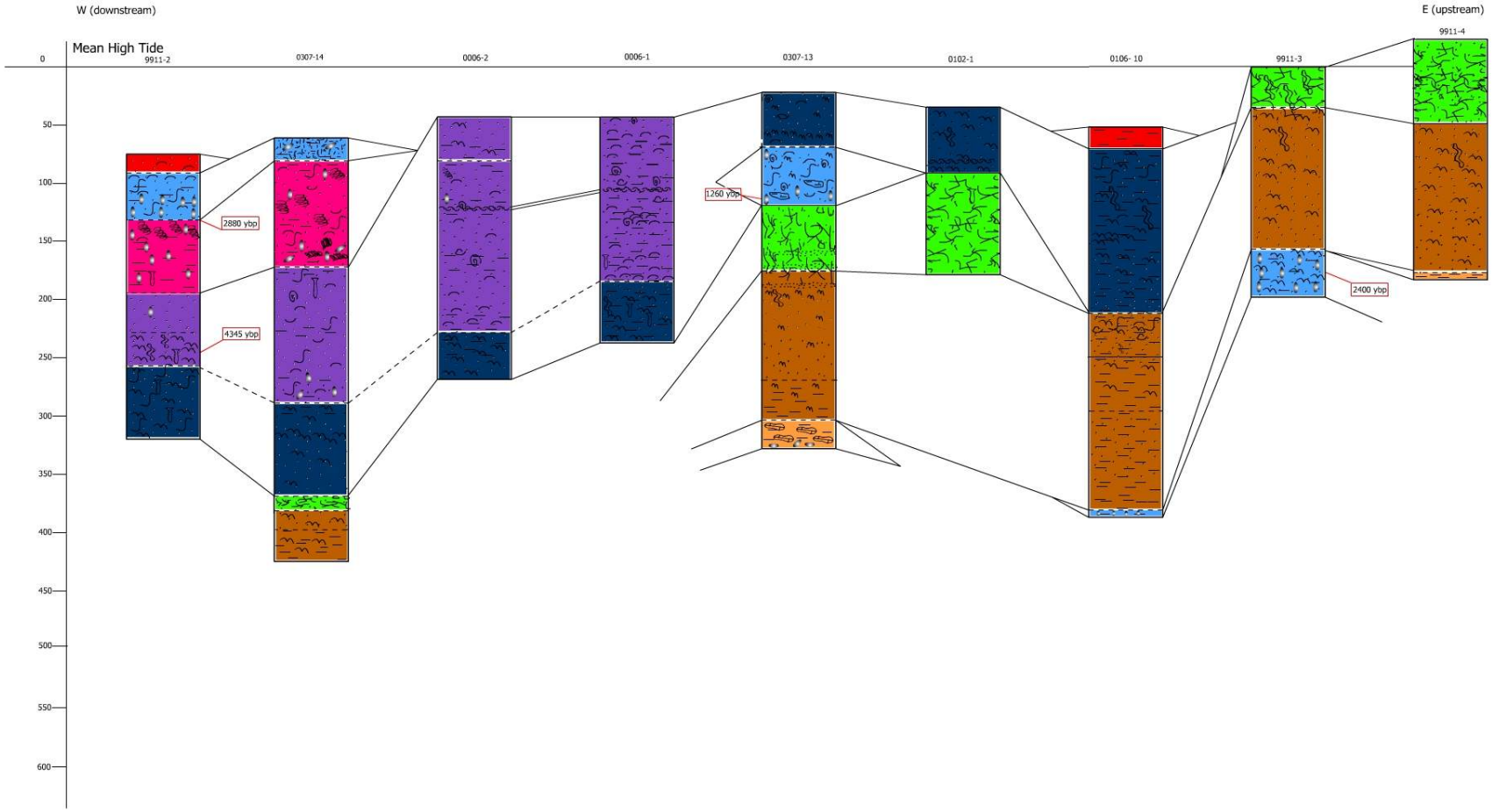

Downstream **Upstream**

Estero River Fence Diagram

Figure 29. Fence diagram for the Estero River transect. Cores are oriented, from left to right, downstream (west) to upstream (east). Facies color-codes same as in Figure 28.

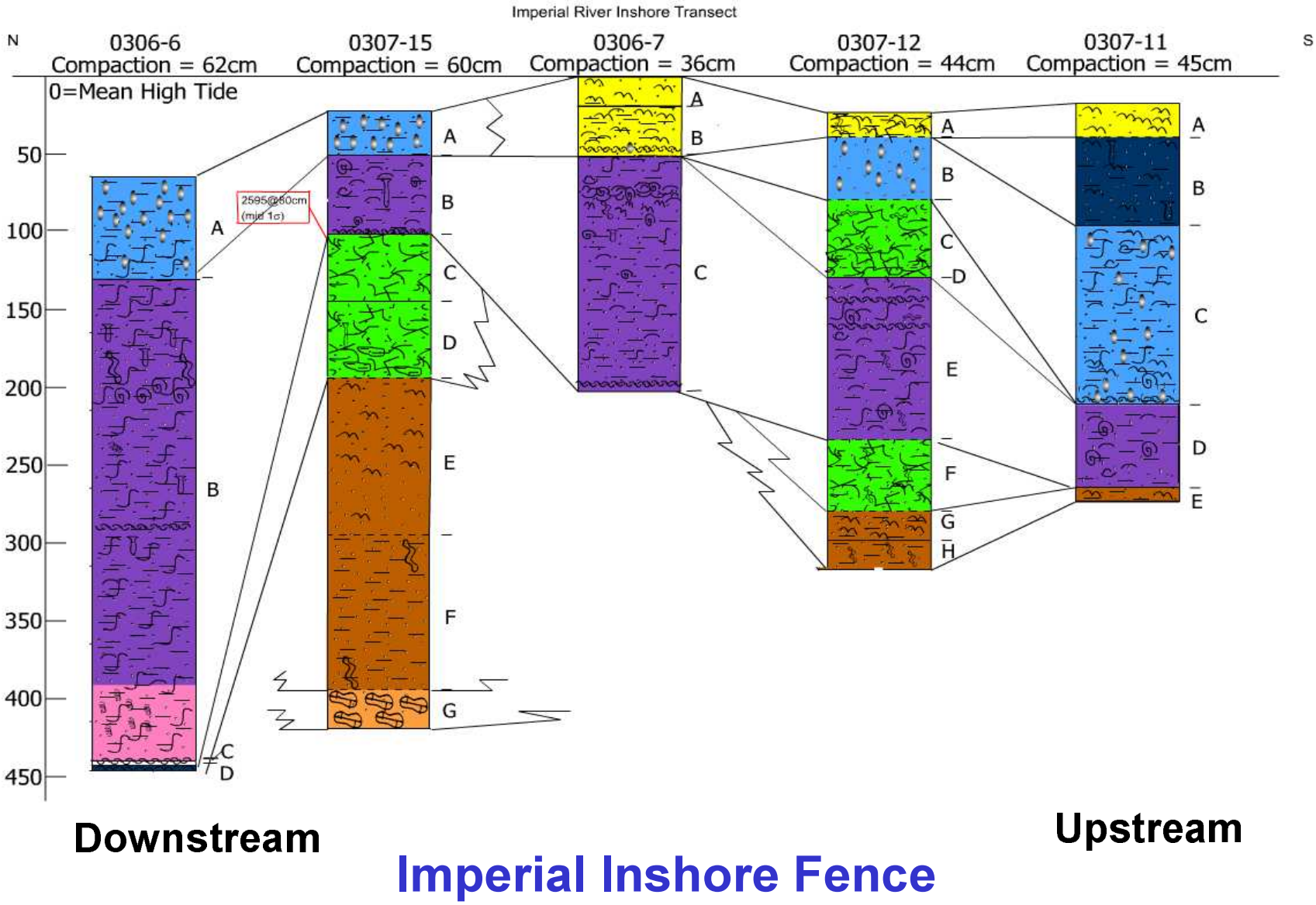

Figure 30. Fence diagram for the inshore transect of the Imperial River. Cores are oriented, from left to right, downstream (north) to upstream (south). Facies color-codes same as in Figure 28.

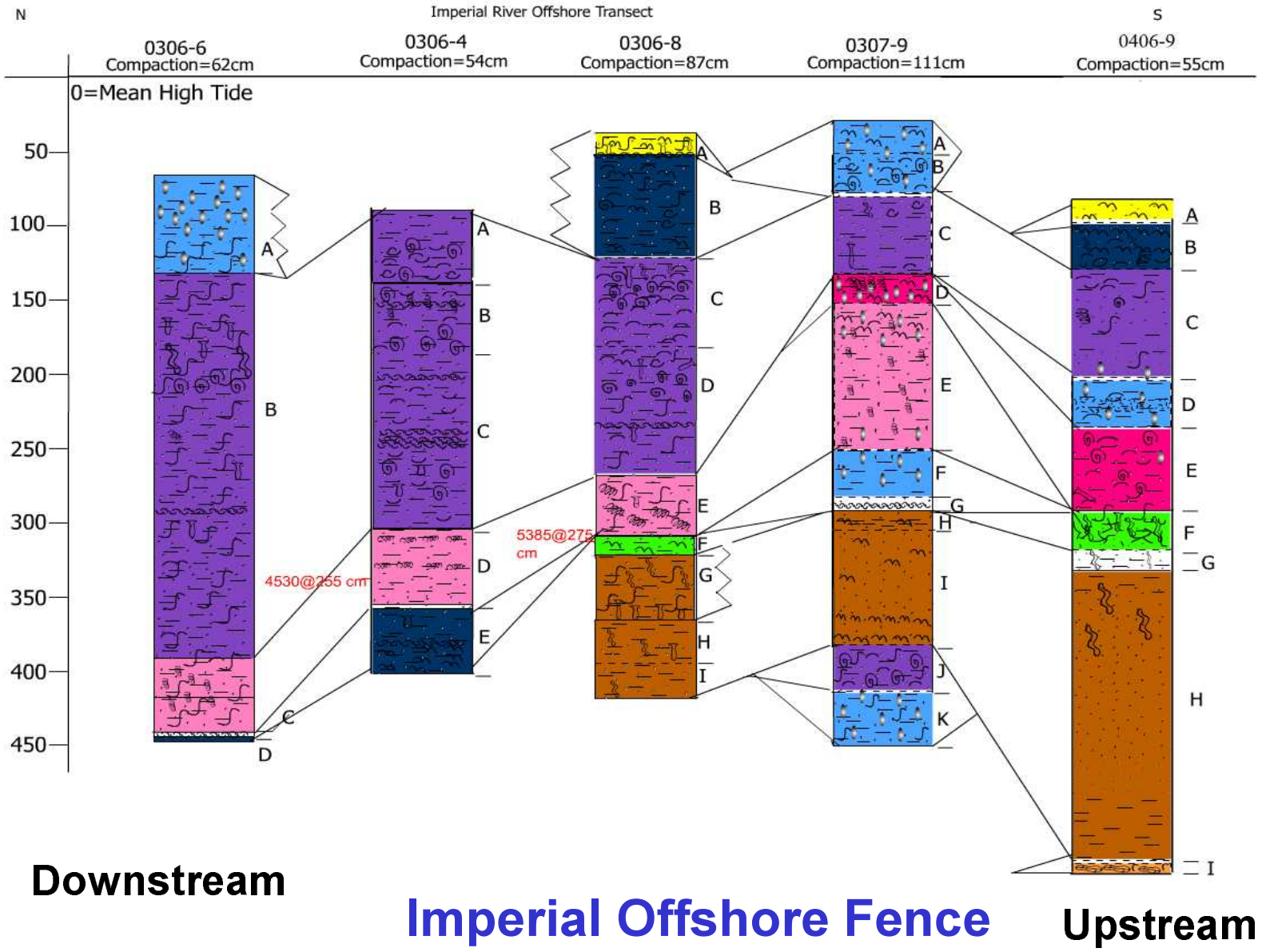

Figure 31. Fence diagram for the offshore transect of the Imperial River. Cores are oriented, from left to right, downstream (north) to upstream (south). Facies color-codes same as in Figure 28.

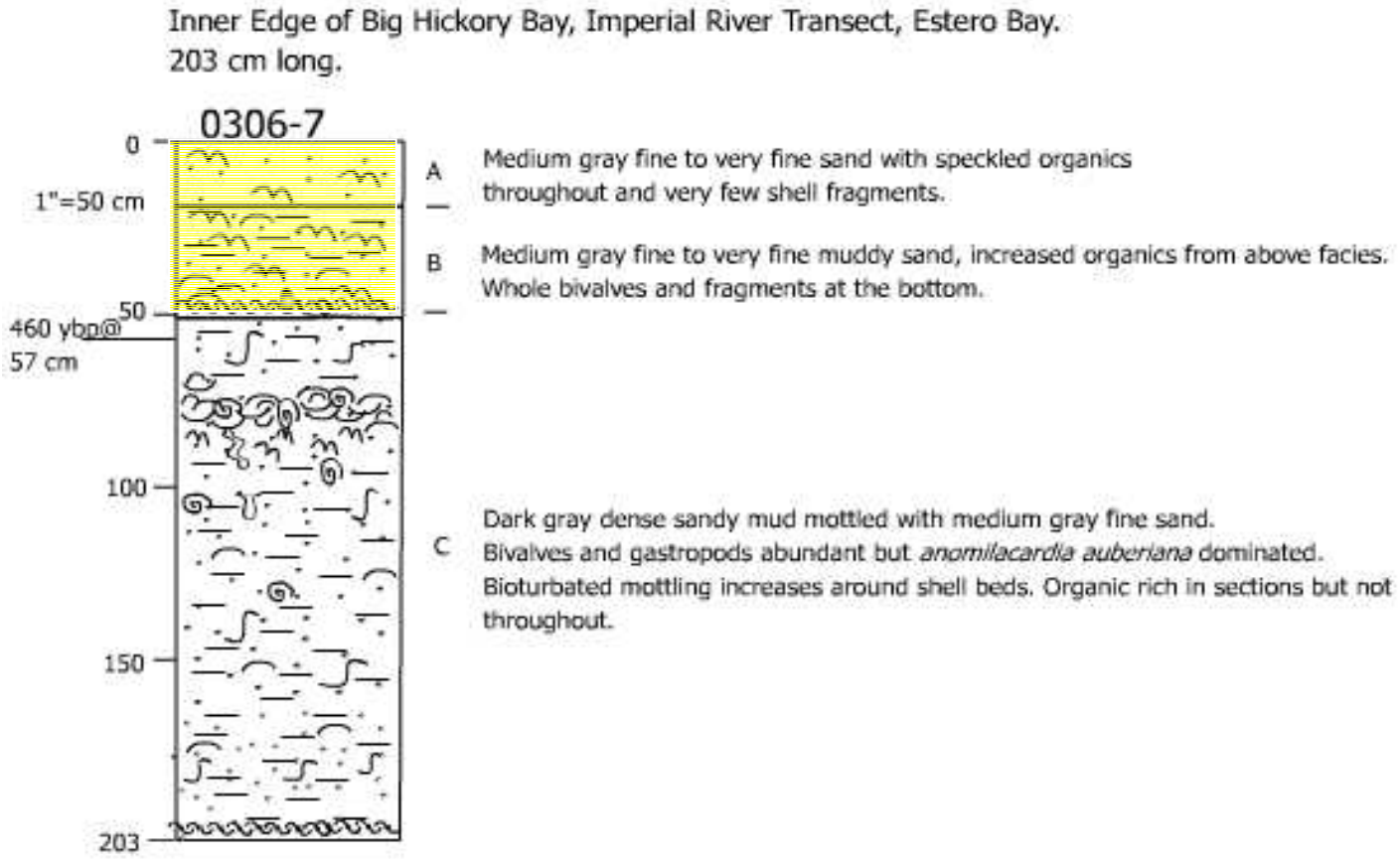

- Fluvial record at old mouth of Imperial River
- Onset at 460 ybp.

Figure 32. Stratigraphic column for core 0306-7 taken from the inner edge of Big Hickory Bay, near the old mouth of the Imperial River. Stratigraphy shows the riverine facies overlying subtidal estuarine sediments. Age of riverine onset dated at 460 ybp.

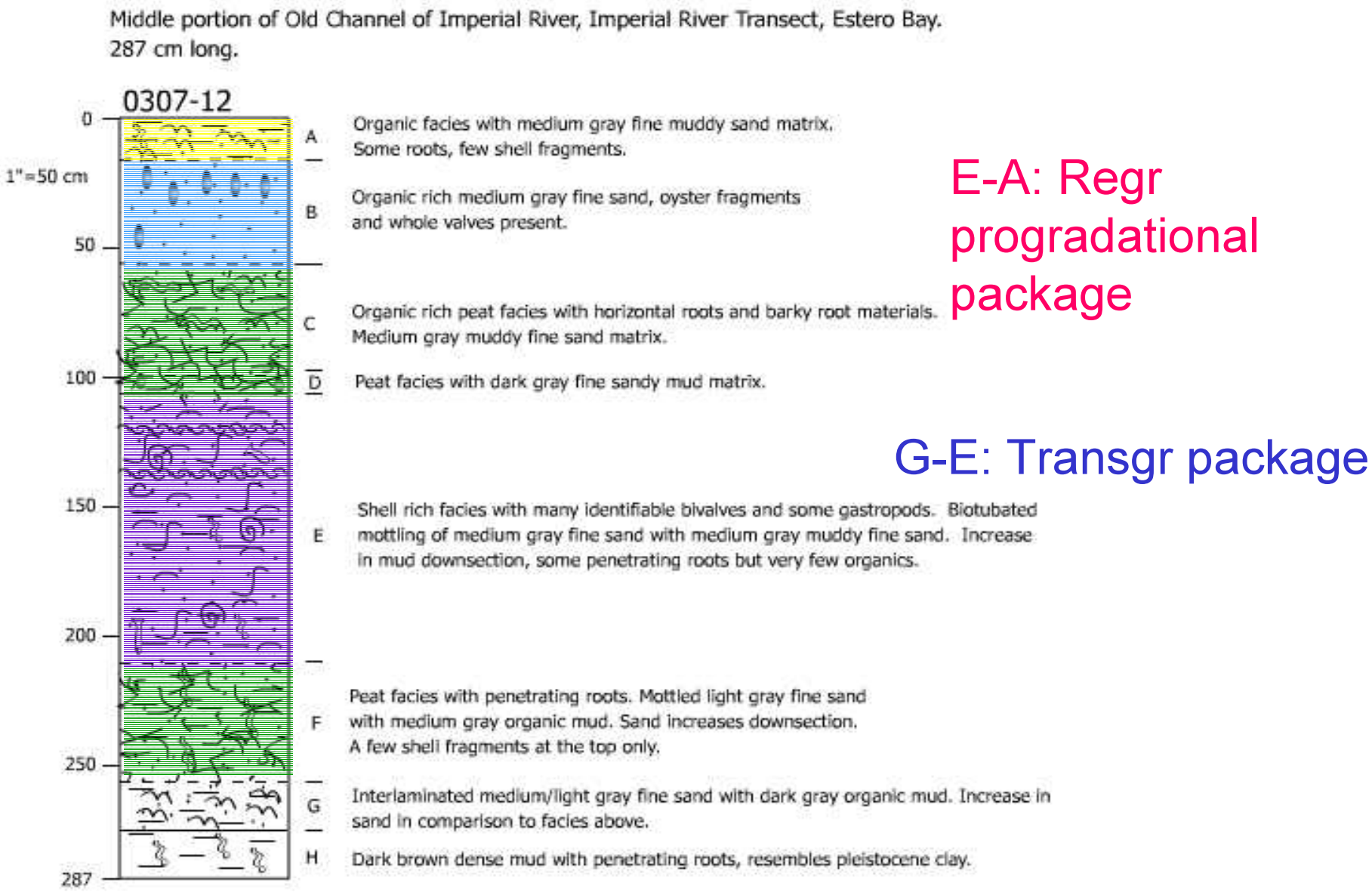

Figure 33. Stratigraphic column for core 0307-12 taken from of the old channel of the Imperial River. Stratigraphy shows the riverine facies in the context of the progradation sequence.

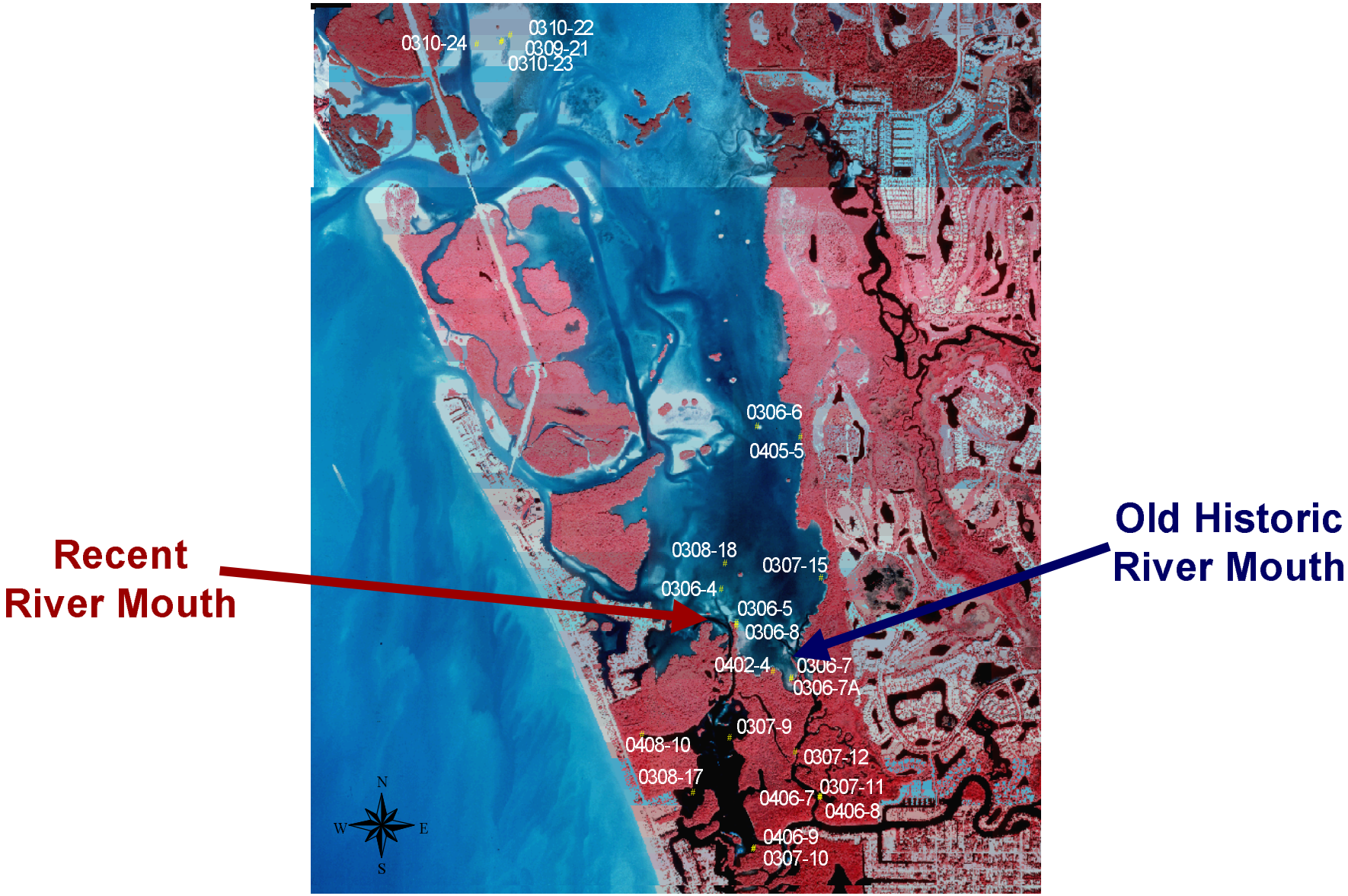

Figure 34. Satellite image of southern Estero Bay showing the position of the old and recent mouths of the Imperial River.

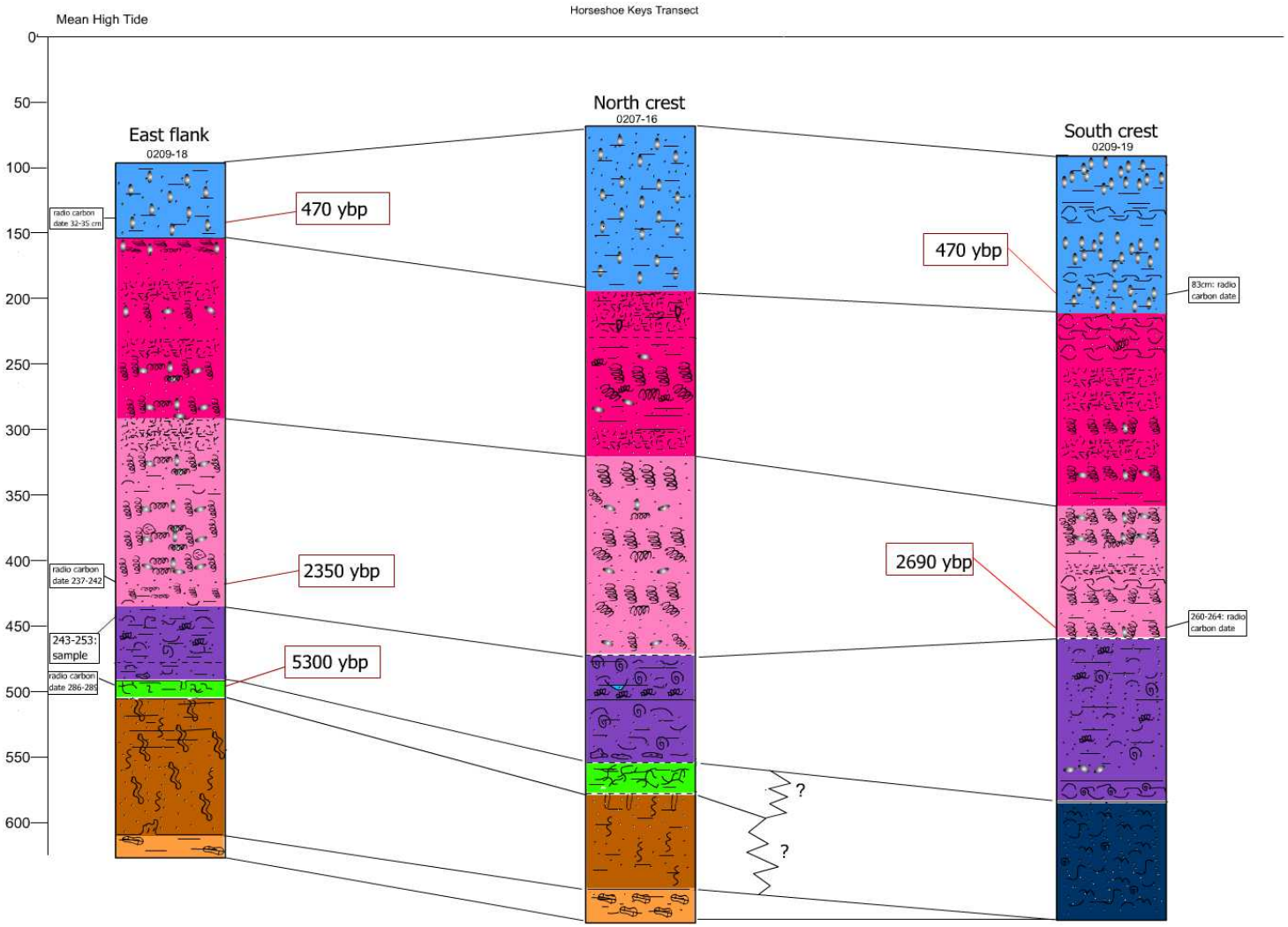

Horseshoe Keys Reef Fence

Figure 35. Fence diagram for the cores taken in the Horseshoe Keys through modern oyster reefs. Facies color-codes same as in Figure 28.

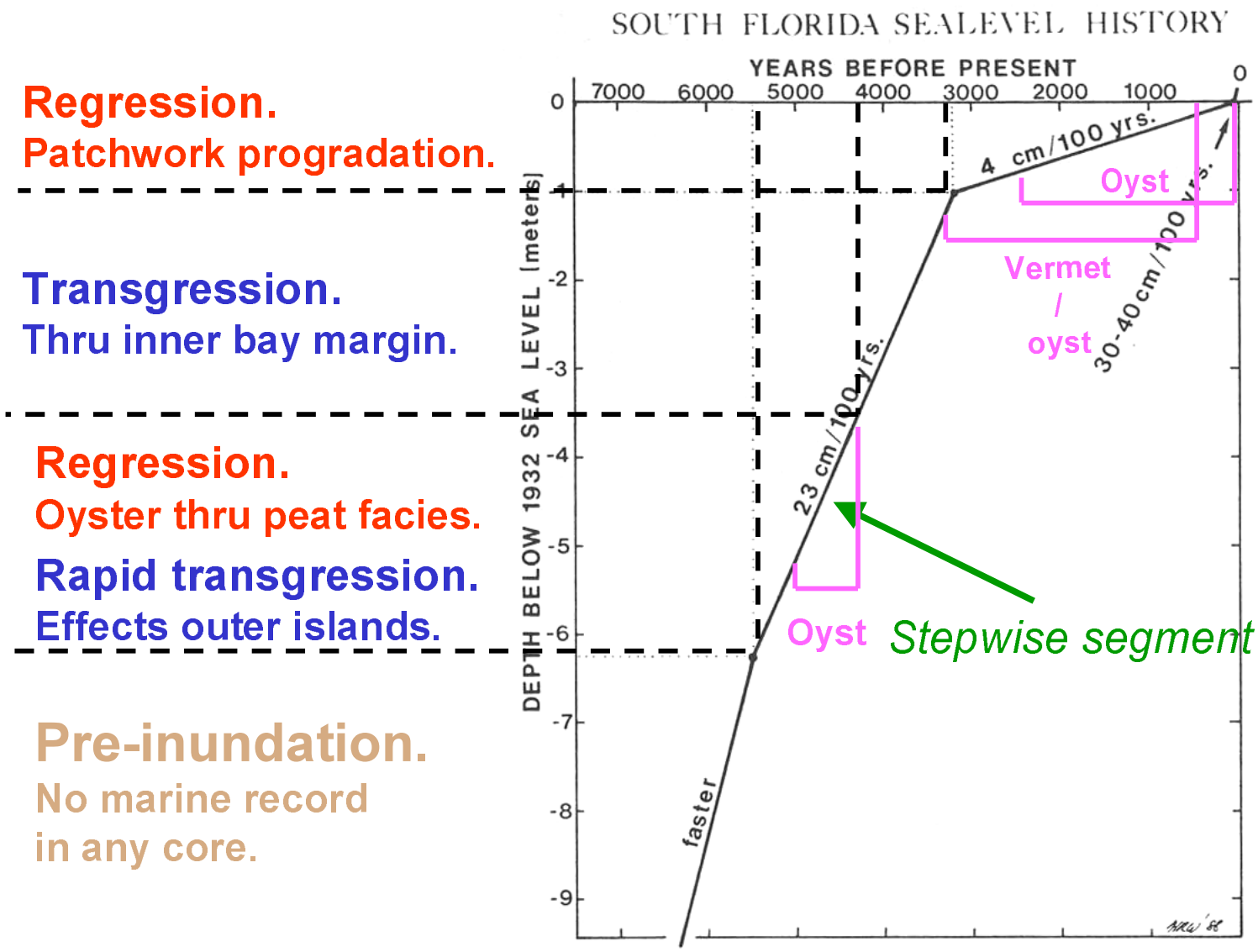

Figure 36. Sea level curve after Wanless et al. (1994) with timing of reef development, relative to the 2 transgressive – regressive cycles, plotted.

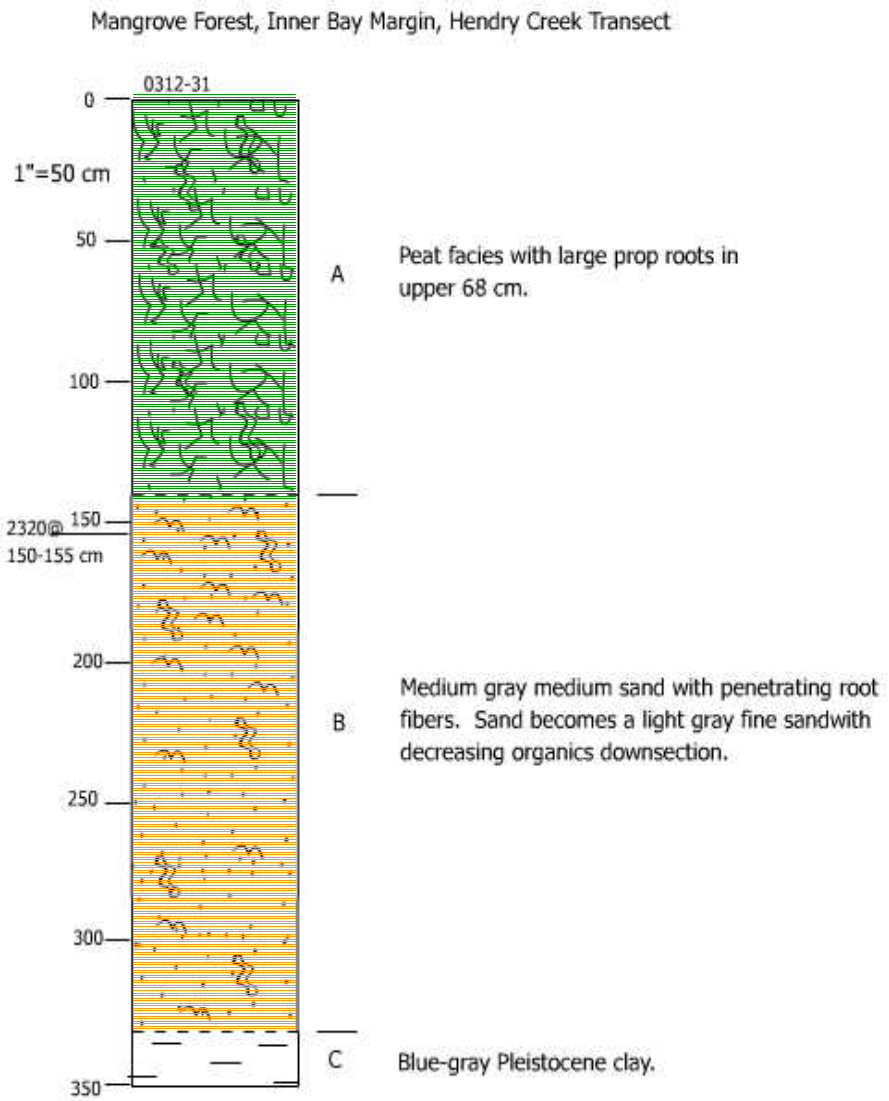

Inner Bay Margin, Hendry

- Mangrove forest peat overlying supratidal sands.
- Peat ~ 2320 ybp.

Figure 37. Stratigraphic column for core 0312-31 taken from of the inner bay margin along the Hendry Creek transect. Core shows the persistence of the mangrove peat facies through time, down to the time of supratidal / subaerial deposition. Peat persisted for at least 2320 years.

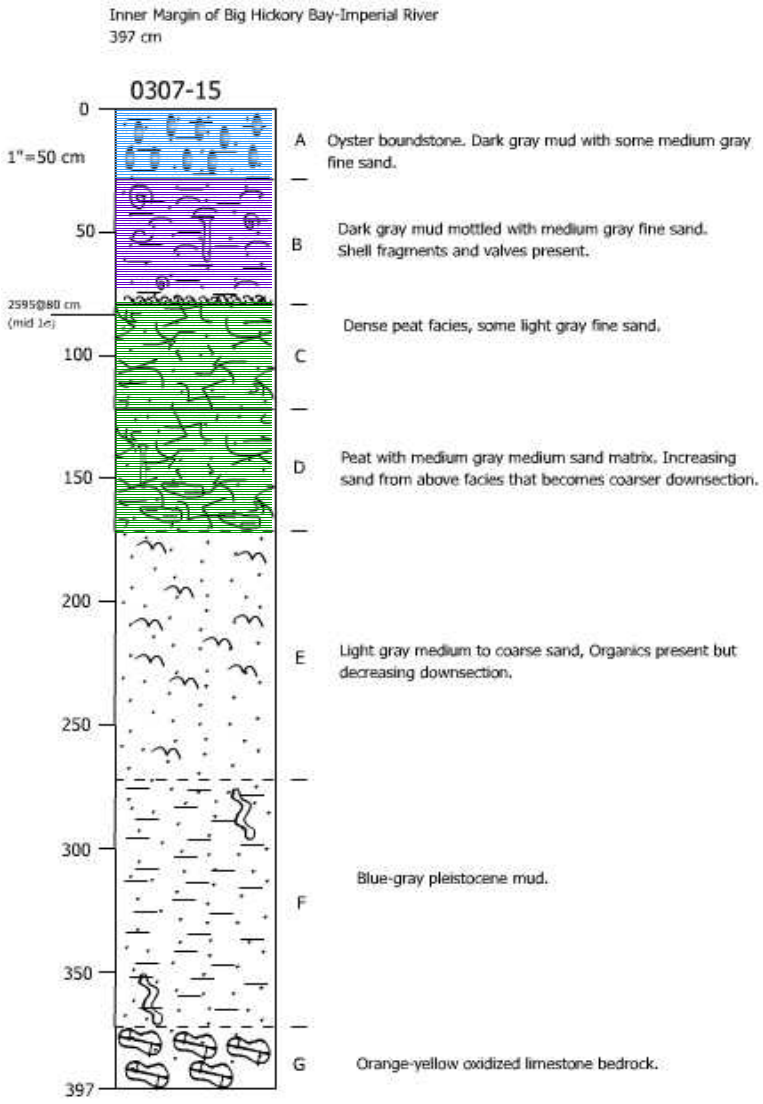

Just Seaward of Inner Bay Margin, Imperial

- Mangrove forest eroded back.
- Step back < 2595 ybp.

Figure 38. Stratigraphic column for core 0307-15 taken approximately 5 m seaward from of the inner bay margin along the shores of Big Hickory Bay. Core shows step-back or transgression of the inner bay margin. A storm event, represented by the shell bed sitting on top of the mangrove peat, eroded down into the underlying peat, stripping away approximately 2600 years of deposition.

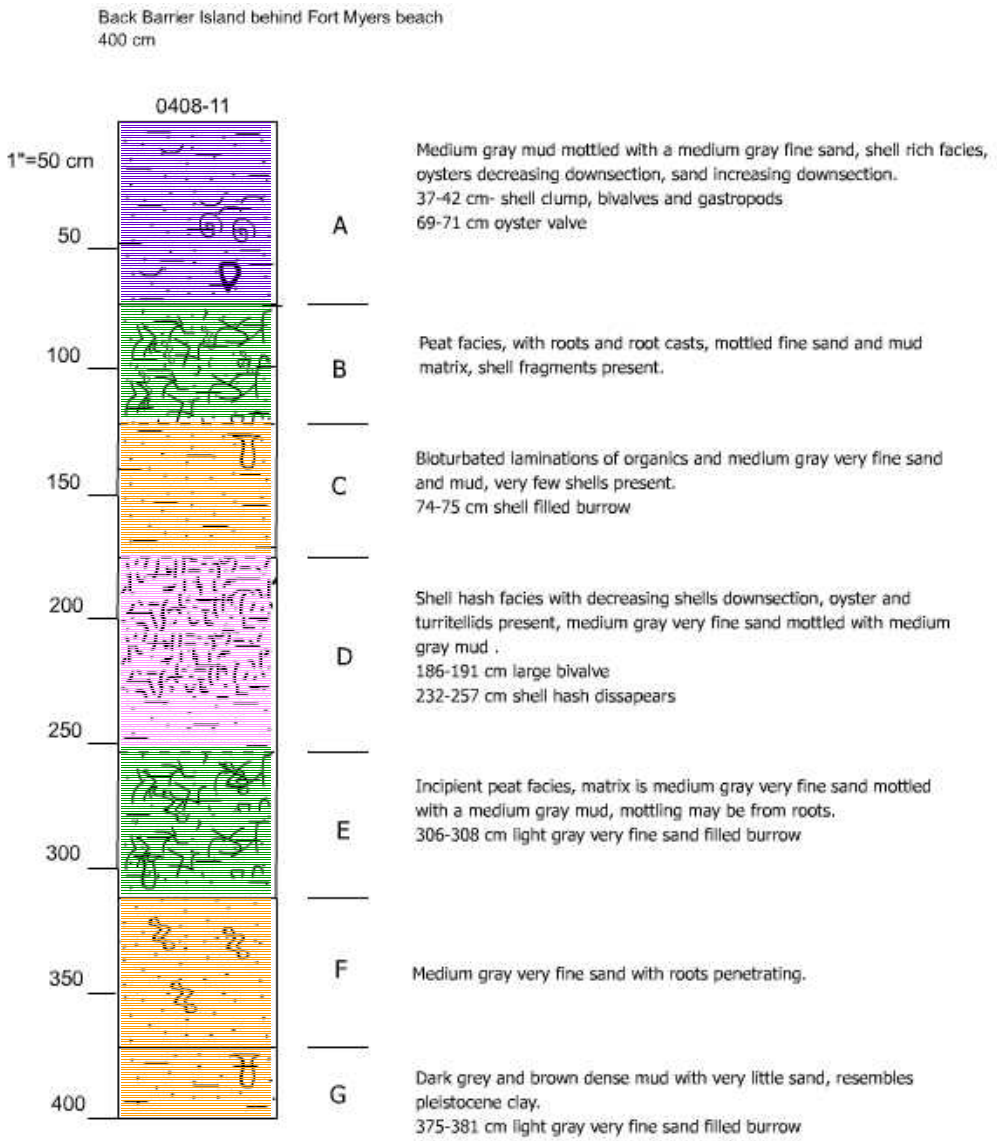

Back-barrier Island, Behind Ft. Myers Beach

A: Subtidal estuarine

B: Back-barrier mangroves

C: Barrier island development

D: Transgr marine, high energy open coast

E: Basal transgr peat

Figure 39. Stratigraphic column for core 0408-11 taken from the back-barrier environment of Fort Myers Beach. Core shows history of barrier island formation.

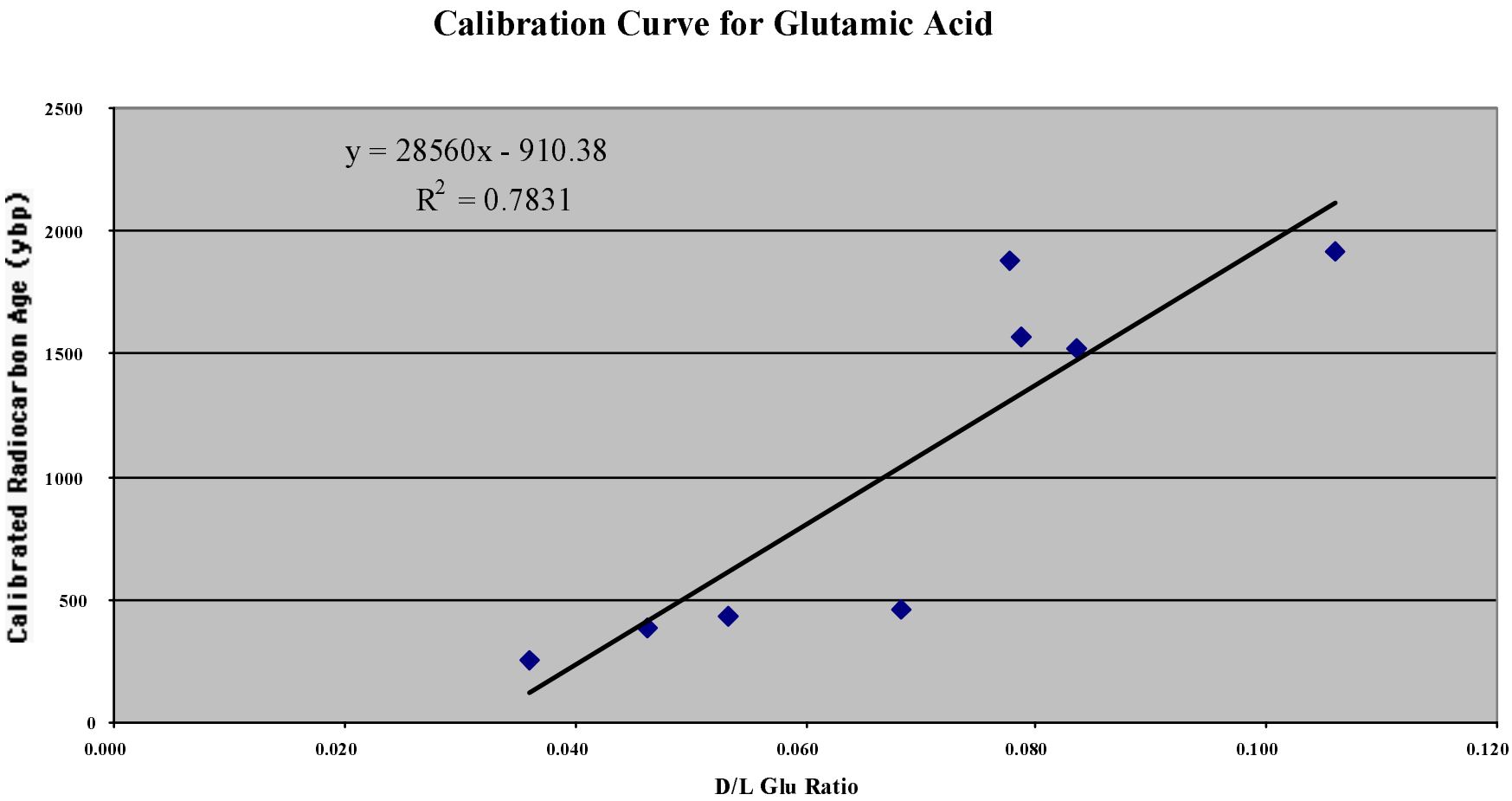

Figure 40. Amino acid racemization dating calibration curve, relative to radiocarbon dates, for oysters collected from one core taken in the Horseshoe Keys. Calibration for D/L glutamic acid ratios. Best fit linear regression equation and goodness of fit measure reported.

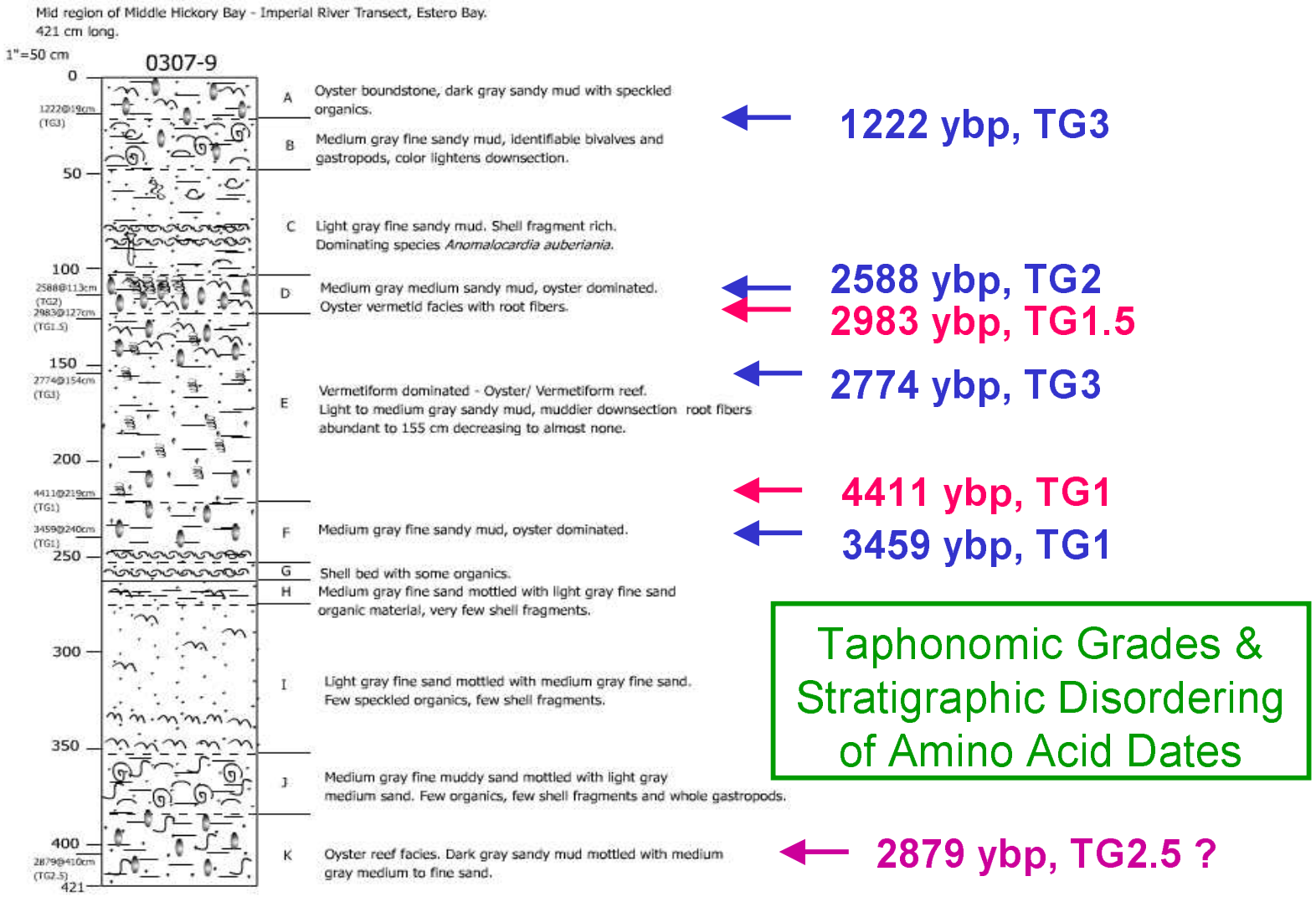

Figure 41. Stratigraphic disordering among oyster amino acid racemization dates, acquired from the radiocarbon calibration equation, for samples taken from core 0307-9 (from the middle region of Fishtrap Bay, Imperial River offshore transect). The taphonomic grade of each oyster is noted; grades run from 1 (pristine) to 4 (very poorly preserved). Red dates represent the most likely disordered oysters. The lowermost date, in purple, represents a date that is far too young given the older radiocarbon dates obtained from these depths in other cores.

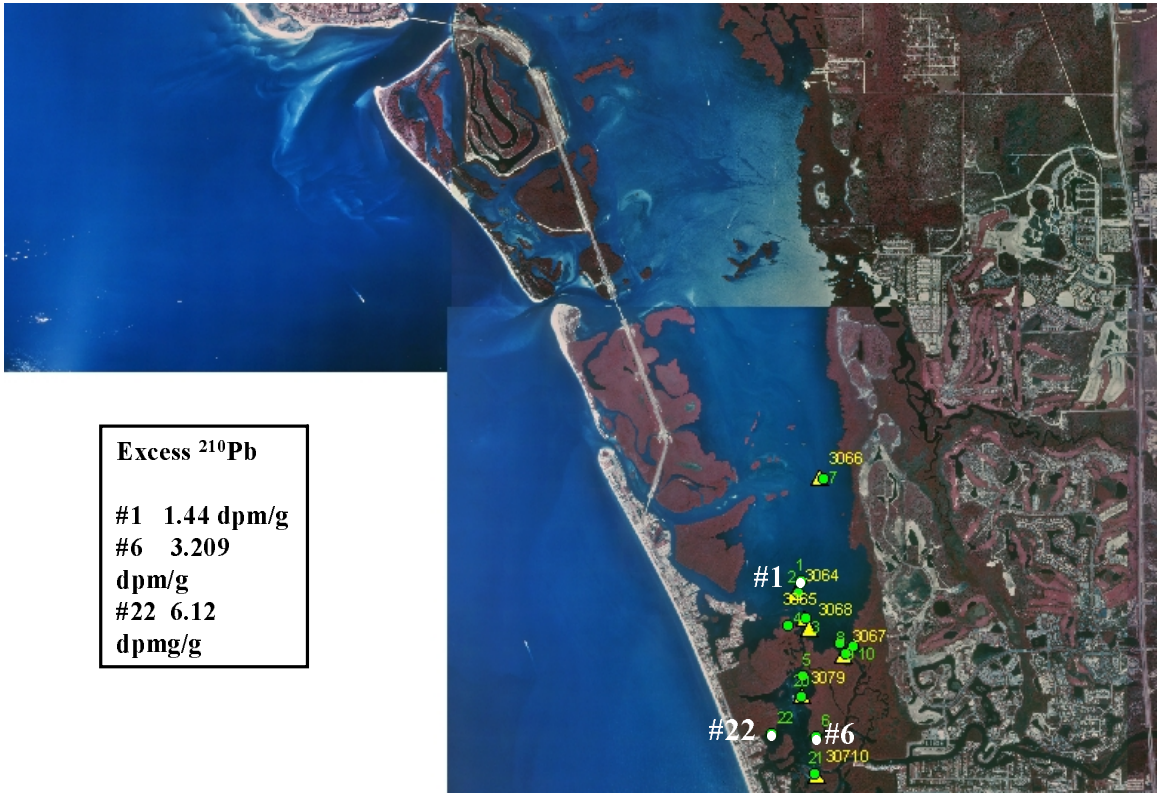

Figure 42. Locations of sites 1, 6, and 22 in Estero Bay where surface sediment samples were collected for determining the activity of excess ^{210}Pb; resulting data are shown in the inset box. Sediment cores were collected at sites 1 and 22 for determination of excess ^{210}Pb, ^{137}Cs, total aluminum, total organic carbon, and calcium carbonate.

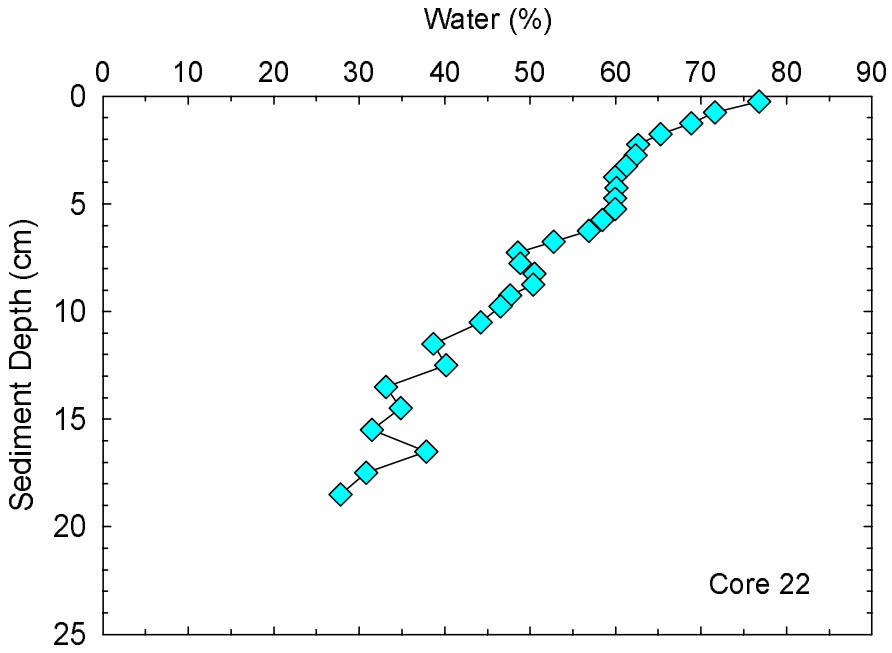

Figure 43. Vertical profile showing water content as % wet weight for core 22.

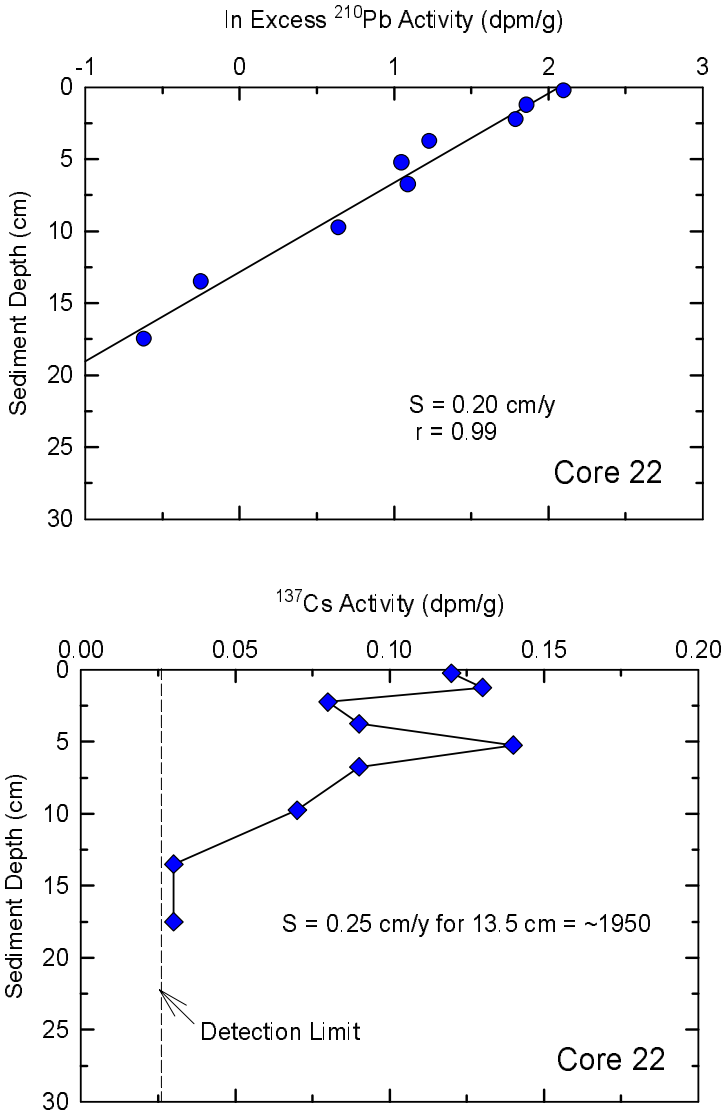

Figure 44. Vertical profiles for natural logarithm (ln) of the activity of excess ^{210}Pb and the activity of ^{137}Cs for core 22. Solid line on ^{210}Pb graph shows linear regression fit to the data, S = sedimentation rate, r = correlation coefficient. Dashed line on the ^{137}Cs plot shows the approximate analytical detection limit.

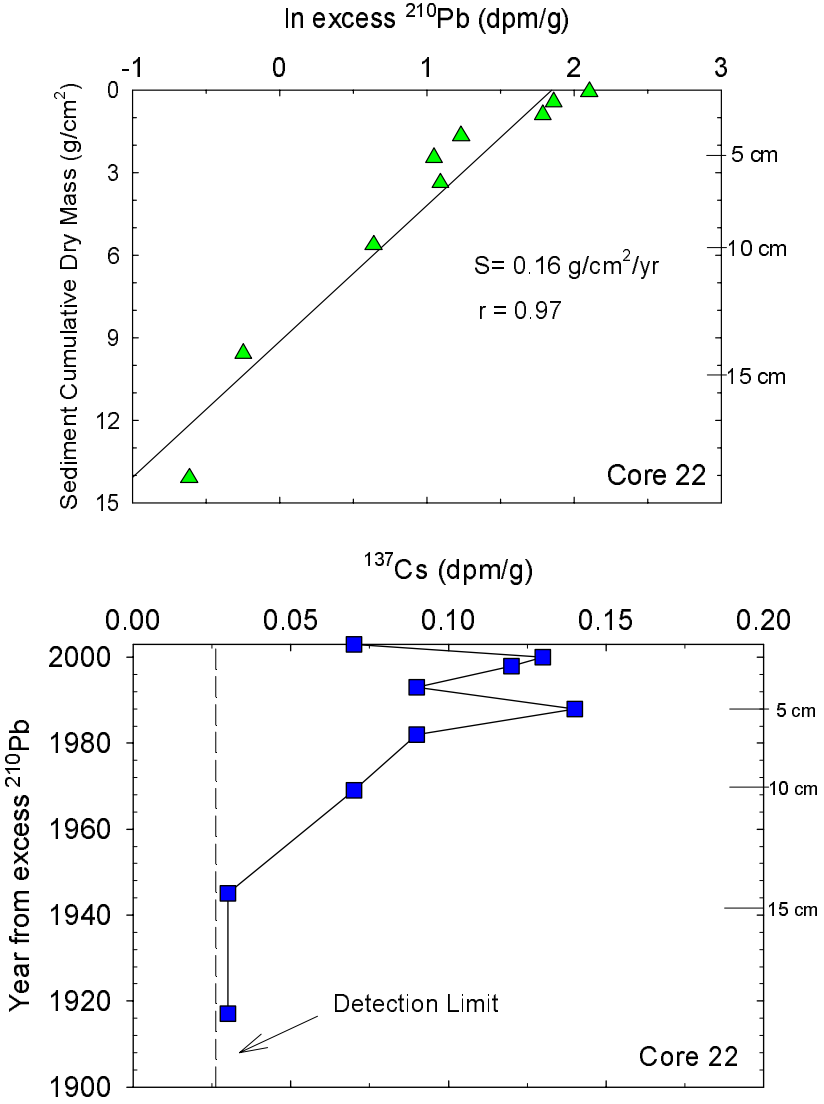

Figure 45. Vertical profiles for the natural logarithm (ln) of the activity of excess ^{210}Pb versus cumulative dry mass of sediment (upper graph) and activity of ^{137}Cs versus year determined from the excess ^{210}Pb data (CIC model). Right-hand axes show sediment depths in cm. Solid line on upper graph shows best fit linear regression line, S = sediment accumulation rate and r = correlation coefficient. Dashed line on the lower graph shows analytical detection limit for activity of ^{137}Cs.

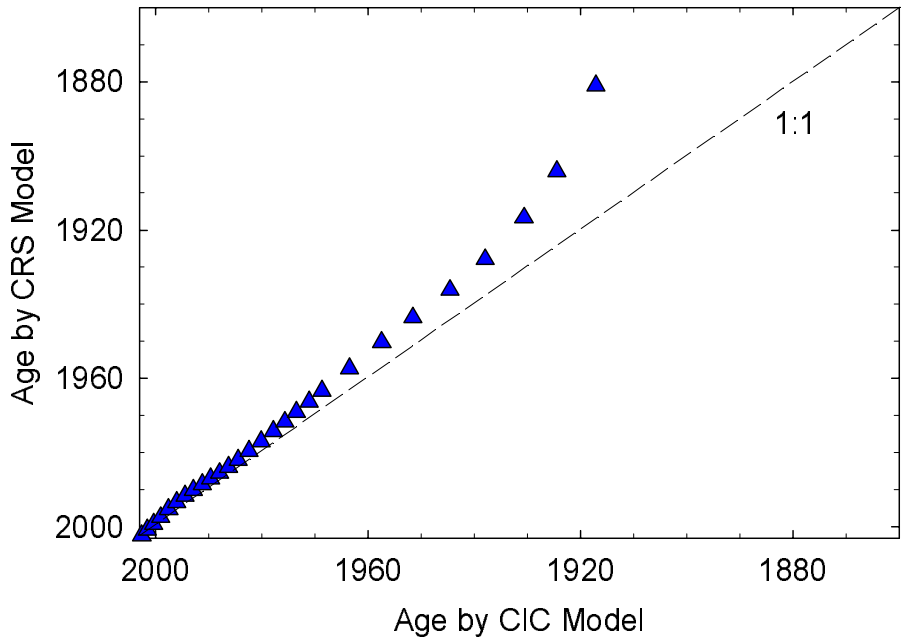

Figure 46. Comparison of ages obtained by constant initial concentration (CIC) model and constant rate of supply (CRS) model for excess ^{210}Pb for core 22 from Estero Bay. Ideal 1:1 agreement between the two models is shown as a dashed line.

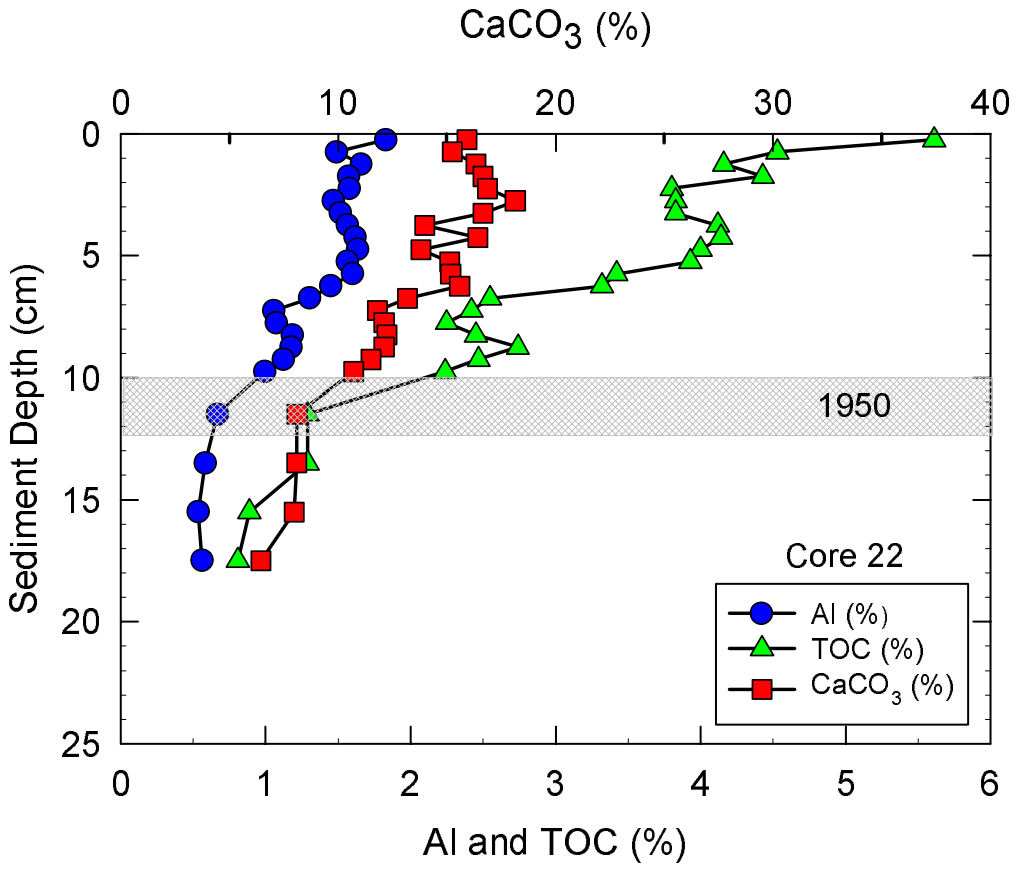

Figure 47. Vertical profiles for concentrations of aluminum (Al), total organic carbon (TOC) and calcium carbonate ($CaCO_3$) for sediments for core 22 from Estero Bay. Shaded area shows depth interval that corresponds to ~1950.

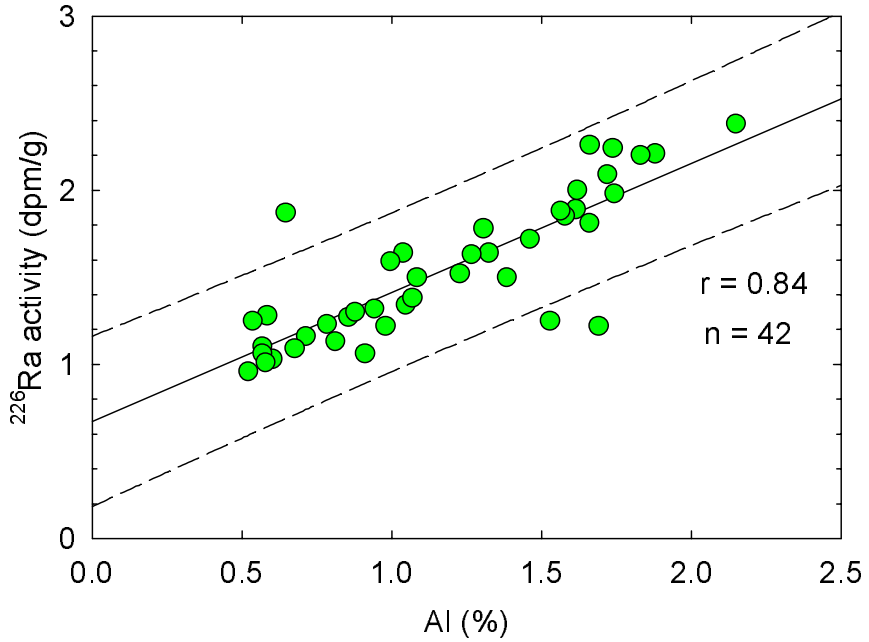

Figure 48. Concentrations of Al versus activity of ^{226}Ra for sediment samples from all cores collected in Estero Bay. Solid line shows linear regression fit to data, r = correlation coefficient, n = number of data points, and the dashed lines show the 95% prediction interval.

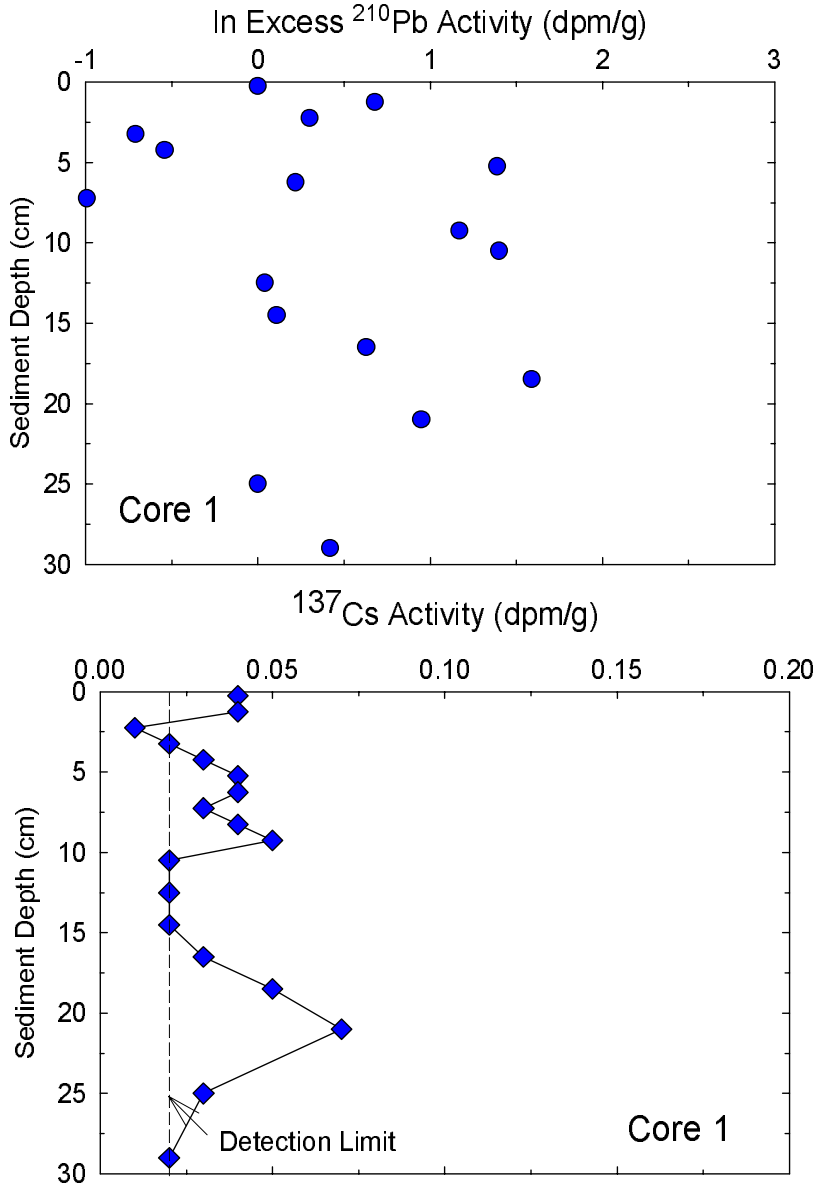

Figure 49. Vertical profiles for natural logarithm of the activity of excess ^{210}Pb and the activity of ^{137}Cs for core 1. Dashed line on the ^{137}Cs plot shows the approximate analytical detection limit.

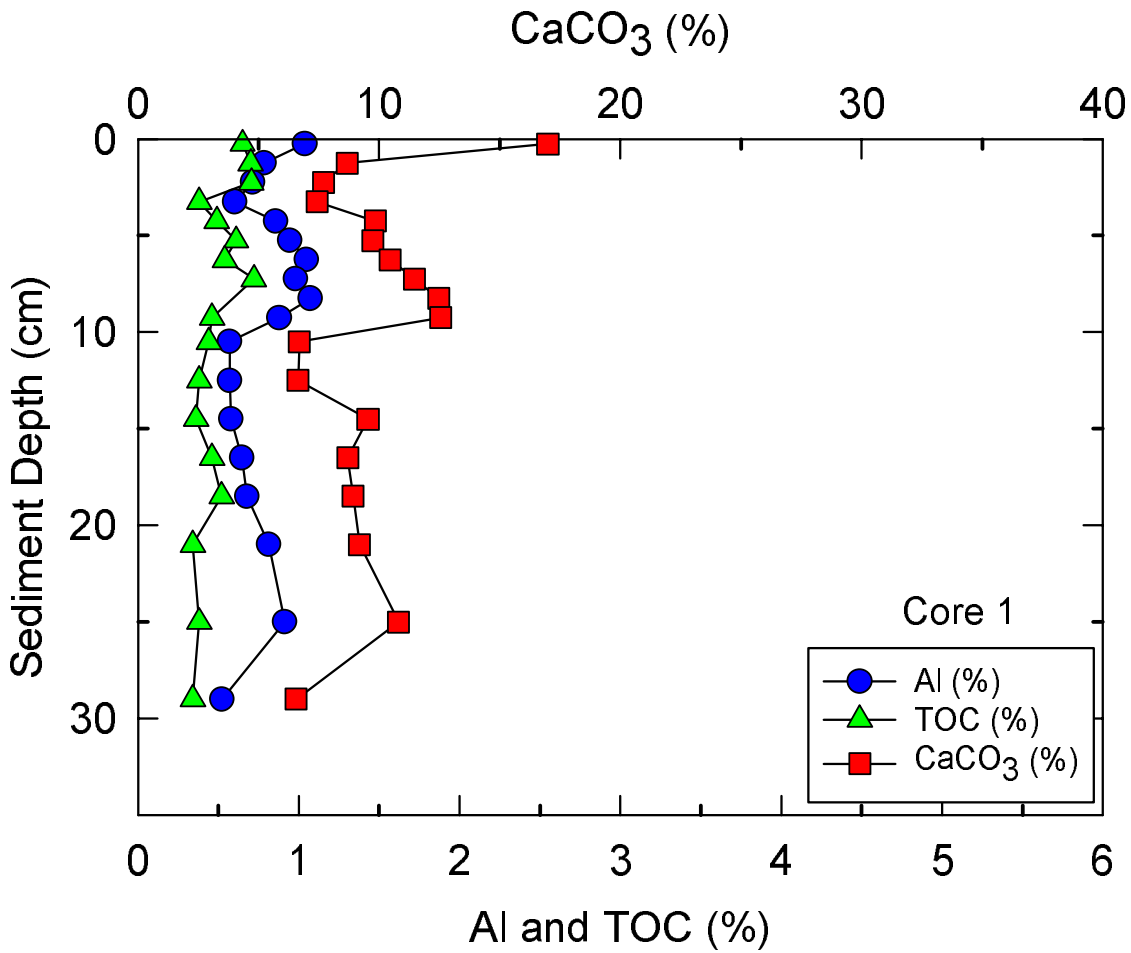

Figure 50. Vertical profiles for concentrations of aluminum (Al), total organic carbon (TOC) and calcium carbonate ($CaCO_3$) for sediments from core 1 in Estero Bay.

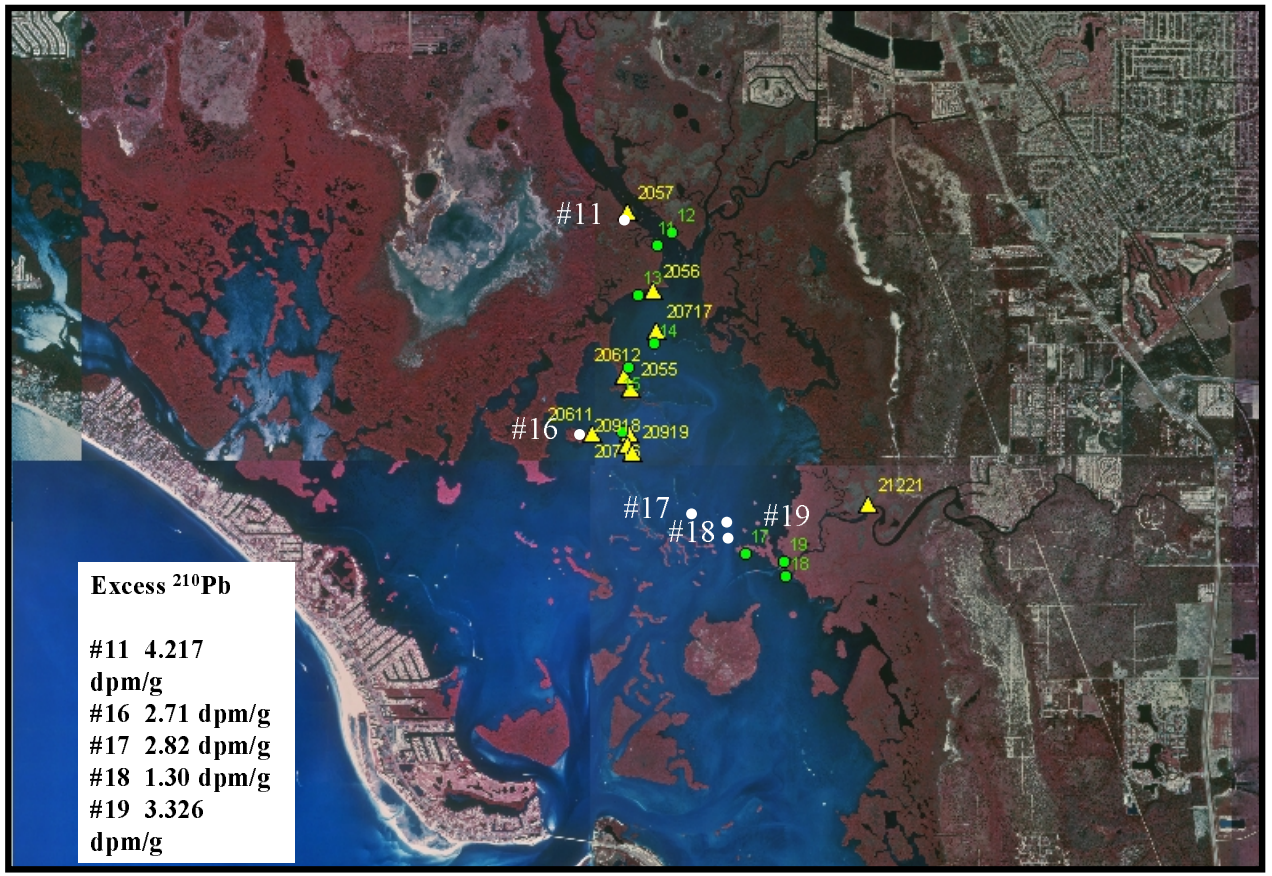

Figure 51. Locations of sites 11, 16, 17, 18, and 19 in Estero Bay where surface sediment samples were collected for determining the activity of excess ^{210}Pb; resulting data are shown in the inset box. A sediment core was collected at site 16 for determination of excess ^{210}Pb, ^{137}Cs, total aluminum, total organic carbon, and calcium carbonate.

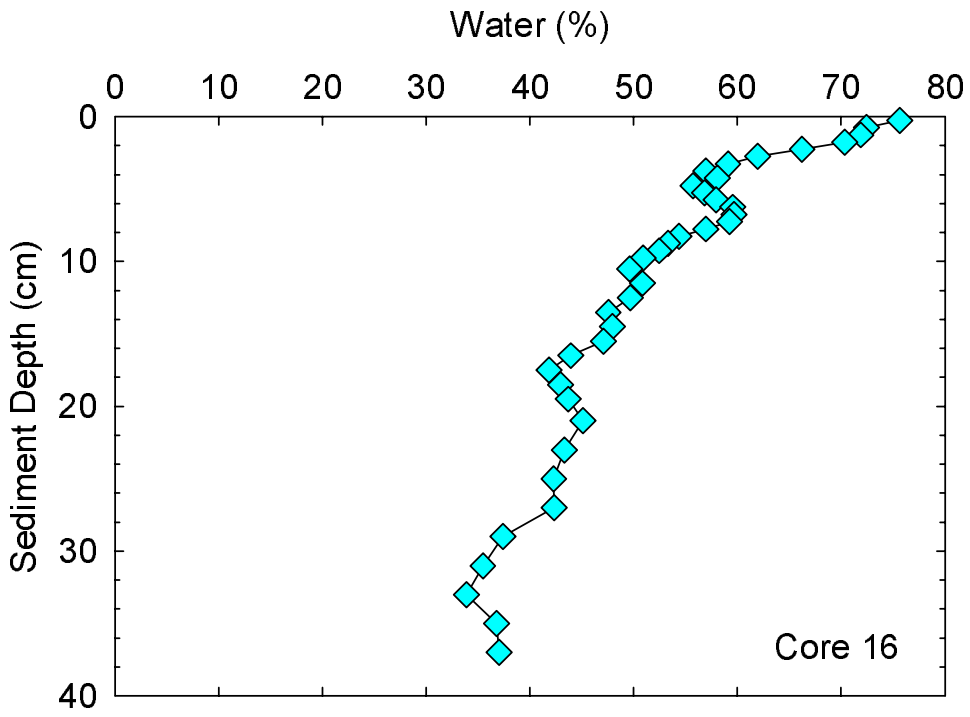

Figure 52. Vertical profile showing water content as % wet weight for core 16.

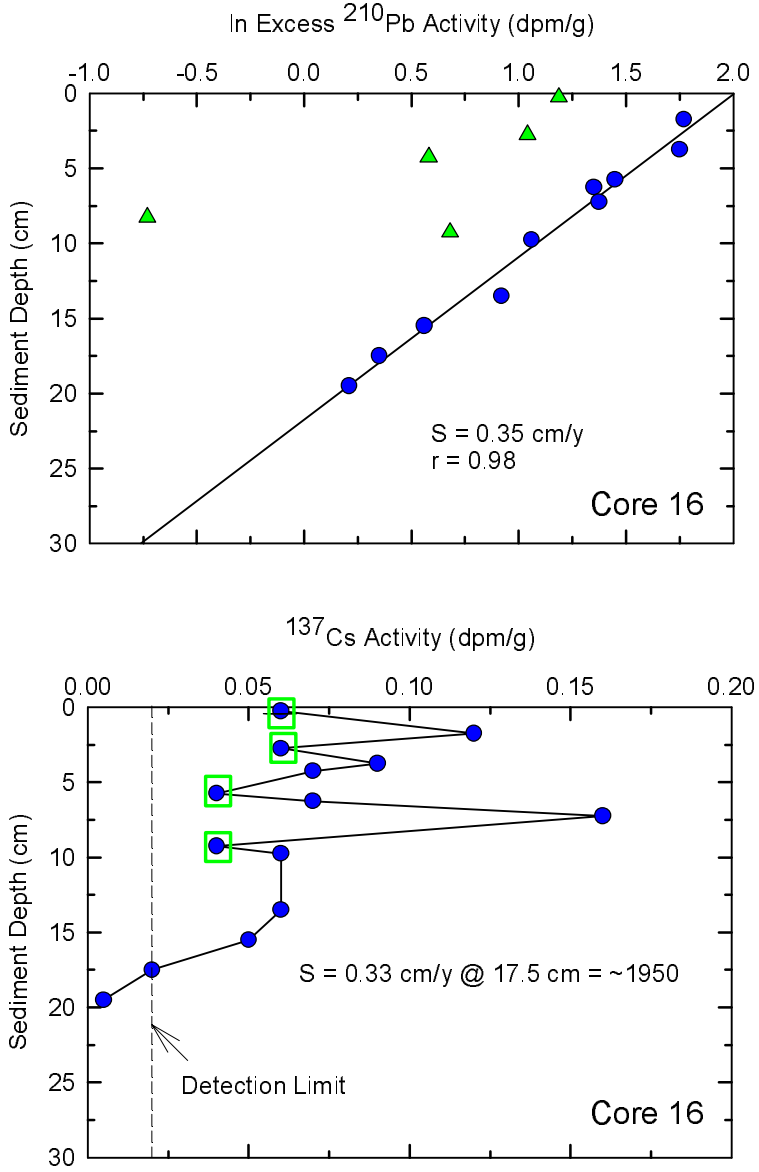

Figure 53. Vertical profiles for natural logarithm of the activity of excess ^{210}Pb and the activity of ^{137}Cs for core 16. Solid line on ^{210}Pb graph shows linear regression fit to the data, S = sedimentation rate, r = correlation coefficient. Dashed line on the ^{137}Cs plot shows the approximate analytical detection limit.

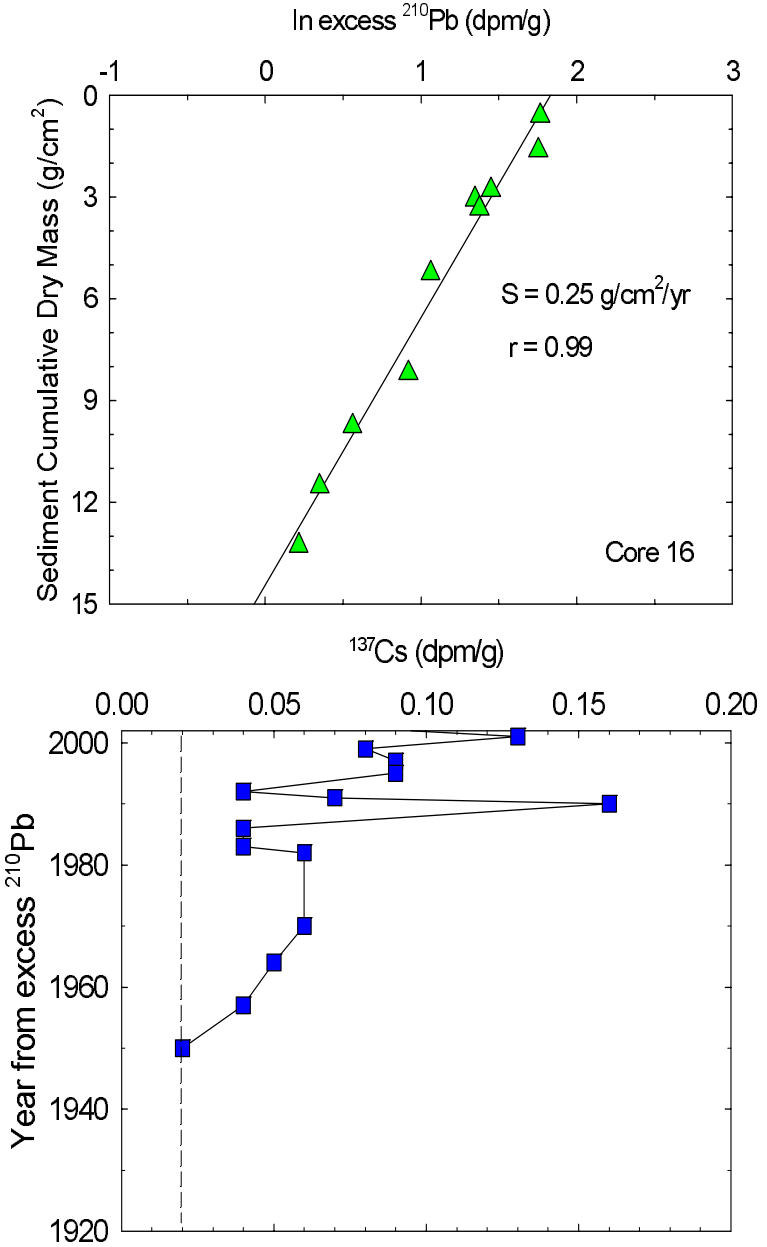

Figure 54. Vertical profiles for the natural logarithm (ln) of the activity of excess ^{210}Pb versus cumulative dry mass of sediment (upper graph) and activity of ^{137}Cs versus year determined from the excess ^{210}Pb data (CIC model). Right-hand axes show sediment depths in cm. Solid line on upper graph shows best fit linear regression line, S = sediment accumulation rate, and r = correlation coefficient. Dashed line on the lower graph shows analytical detection limit for activity of ^{137}Cs.

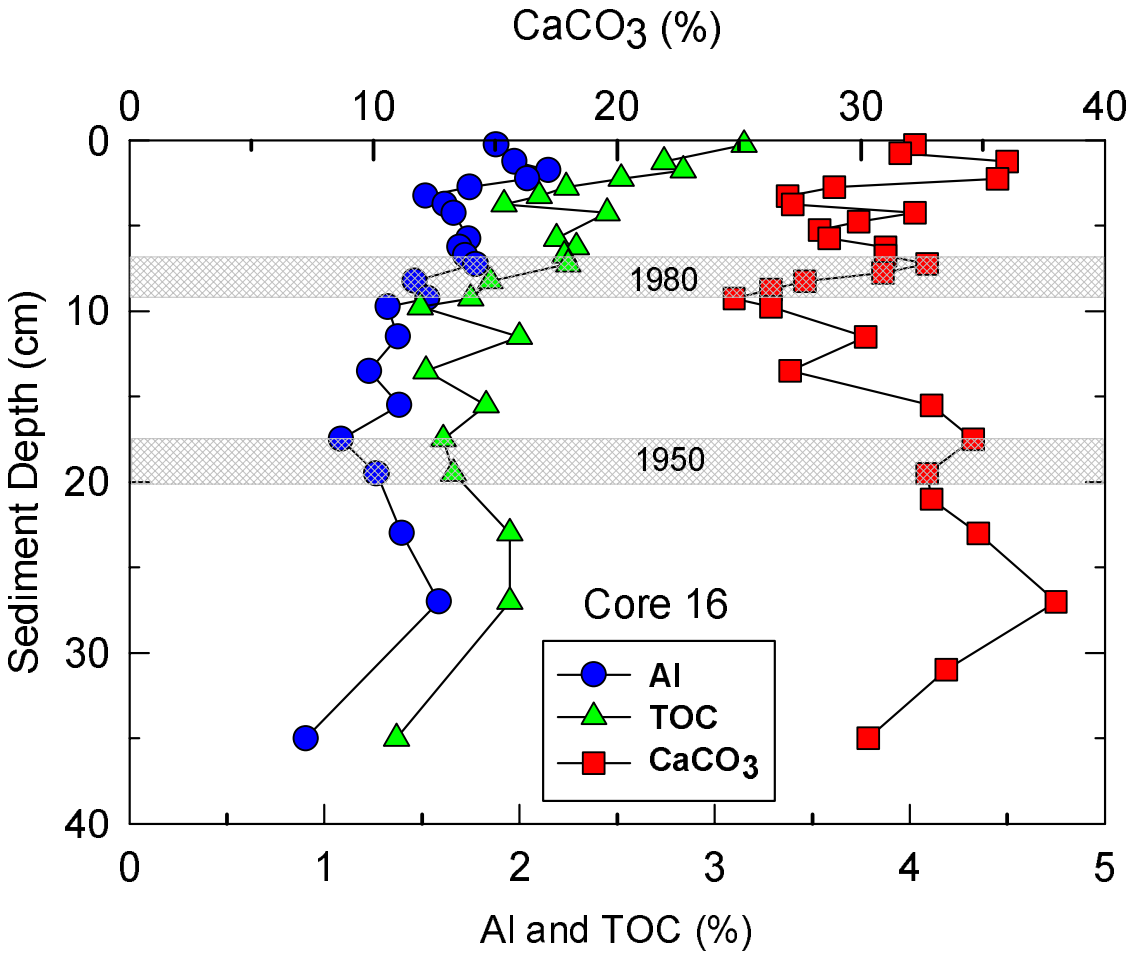

Figure 55. Vertical profiles for concentrations of aluminum (Al), total organic carbon (TOC), and calcium carbonate ($CaCO_3$) for sediments for core 16 from Estero Bay. Shaded areas shows depth intervals that corresponds to ~1950 and 1980.